NTNU

Norwegian University of
Science and Technology

Power Production from Low Temperature Heat Sources

Alexander Midtsjø

Master of Science in Energy and Environment

Submission date: June 2009

Supervisor: Arne Mathias Bredesen, EPT

Co-supervisor: Yves Ladam, SINTEF Energiforskning

Norwegian University of Science and Technology
Department of Energy and Process Engineering

Problem Description

Background and objective.
Sintef Energy Research As is involved in a KMB project 162617/i40 Resource Optimization and recovery in the MAterials industry.

We are involved in the Energy Recovery part of this project. A new technology for power production from low to medium temperature heat sources will be developed. Application to power production from exhaust of electrolysis cells in the aluminium industry will be investigated. This technology will be based on the use of CO2 as a working fluid. CO2 is non flammable non toxic and is environmental friendly. Preliminary calculations showed an important potential for performance improvement compared to existing technologies.

A prototype will be built in our laboratory early in 2009. The student will be involved in the assembling and instrumentation of this rig. He will also perform experiments with this prototype. Results will be analysed and compared to simulations (ProII) in order to establish optimization and off design control procedures.

The following questions should be considered in the project work:

1. Litterature survey
2. Install instrumentation on the prototype
3. Experimental investigation of prototype power production system. Establish optimization and control procedures
4. Analysis and discussion of results and findings, and preparation of a final report to be submitted for evaluation

Assignment given: 19. January 2009
Supervisor: Arne Mathias Bredesen, EPT

Preface

This report is the written work of my Master thesis at the Norwegian University of Science and Technology, Faculty of Engineering Science and Technology, Department of Energy and Process Engineering, spring 2009. The subject of the thesis was decided in cooperation with SINTEF Energy Research and is a part of the KMB project Resource Optimization and recovery in the MAterials industry (ROMA). The Master thesis is a continuation of a project work done in autumn 2008.

The work done in my Master thesis has been a combination of practical work in the laboratory, where I have done some instrumentation and assembling of a prototype rig, calculations and simulations, and establishing of optimization and control procedures for the prototype rig. I feel that my knowledge have been tested thoroughly by the different tasks given in the work with the thesis. Doing so much practical work in the laboratory has given me a better understanding of the physical behavior of thermodynamic systems in general and especially of the prototype rig. In addition I must say that one of the most important lessons learnt is that things do not always work out as planned, and that it's important to always have a plan B.

In my work with the thesis I've had a lot of helpful guidance and assistance. For this I would like to thank my research advisor Yves Ladam for the fine combination of giving helpful advices and challenging my knowledge. I would like to thank Reidar Tellebon and Gunnar Lohse for the invaluable help in the laboratory in matters of assembly and instrumentation of the prototype rig. In addition I would like to thank Håvard Rekstad, Michael Drescher, Armin Hafner and Professor Arne M. Bredesen.

Trondheim, June 2009

Alexander Midtsjø

Summary

As part of the energy recovery part of the ROMA (Resource Optimization and recovery in the Materials industry) project, a laboratory prototype power production system is being built and completed in 2009. The laboratory prototype is based on a new technology for power production from low to medium temperature heat sources (the off gas from electrolysis cells in the aluminum industry) where CO_2 is used as a working medium in a trans-critical Rankine cycle. The laboratory rig consists of the power cycle with a prototype expander as the core unit, an air loop to provide the heat, and an ethylene glycol loop to provide condensation of the working fluid in the power cycle.

As a preparation to the assembling and instrumentation of the prototype rig, a simulation and an uncertainty analysis were conducted for the prototype rig in the autumn of 2008. This report focuses on the continuation of that work by an experimental investigation of the individual loops and the components of the prototype rig. The emphasis of this investigation has been put on the air loop and the expander unit of the power cycle. This is basically because these are of great importance to the performance of the power production prototype rig.

The air loop was thoroughly tested, and from the investigations it was discovered that there was an unfavorable temperature distribution of the air going into the air-to-CO_2 heat exchanger. This is the heat exchanger where heat is provided to the power cycle. The source for this temperature maldistribution was identified, and solutions were investigated to improve on the problem without results. The reduced performance of the air loop was incorporated in a new simulation of the power cycle in order to quantify the consequences for the optimization of the power cycle. The simulation was carried out for warm air temperature of 80 °C. The new calculations showed a reduction in maximum net work output of 27 % compared to the original simulation. The optimal conditions for the power cycle were also changed as a consequence of the reduced air loop performance.

The investigation of the expander unit revealed that the expander isentropic efficiency was a strong function of the pressure difference across the expander, and a weak function of the expander inlet pressure. It also revealed that overall the isentropic efficiency was much less than the value of 80 % which was used in the original simulation. A new simulation of the power cycle was carried out where the expander isentropic efficiency was incorporated as a function of the pressure difference across the expander. This function was based on the data from the expander testing. The simulation showed a reduction in maximum net work output from 225 W to about 60 W, for warm air temperature of 80 °C. The new expander characteristics also affected the optimization of the power cycle.

The simulation results and the results from the prototype investigation will be important in the optimization and control procedures of the assembled prototype power production system.

Preface I
Summary II
List of symbols V
1. Background – Aluminum production in Norway 1
1.1 Historical background 1
1.2 The aluminum production process [2] 2
1.3 Energy flow in the aluminum process 4
2. Waste heat to power – State of the art 5
2.1 Technical processes for waste heat recovery 5
2.1.1 Water vapor Rankine cycle 6
2.1.2 Organic Rankine cycle 7
2.1.3 The Kalina cycle 9
2.1.4 Misc gas cycles 11
2.1.5 The ideal power cycle and its fundamental constraints 14
3 ROMA project – Waste heat to power production system prototype 17
3.1 Concept – The CO_2 trans-critical Rankine cycle 17
3.1.1 Thermodynamic description 17
3.1.2 The benefits of working trans-critically 18
3.1.3 Challenges related to the cycle 19
3.2 Prototype rig 20
3.2.1 Prototype design 20
3.2.1.1 Main process – CO_2 power cycle 20
3.2.1.2 Supporting circuits – Ethylene glycol and warm air circuits 21
3.2.1.3 Supplementary circuit – CO_2 Heat pump 21
3.2.2 Prototype control strategies 22
3.2.2.1 Boundary conditions 22
3.2.2.2 Main process – CO_2 power cycle 23
3.2.2.3 Supplementary circuit – CO_2 Heat pump 23
3.3 Prototype simulation and uncertainty analysis 24
3.3.1 Prototype simulation 24
3.3.2 Uncertainty analysis of prototype 26
3.4 Prototype preparation and testing 31
3.4.1 Prototype testing - Warm air loop 31
3.4.1.1 Preliminary testing 31
3.4.1.2 Installation of thermocouples 33
3.4.1.3 Air loop – Mass flow measurements 35
3.4.1.4 Air loop - Testing of temperature profile 39
3.4.1.5 Air loop – Investigation of heater unit 44
3.4.1.6 Air loop – Investigation of heat exchangers and air fan 48
3.4.1.7 Conclusion on air loop testing 53
3.4.1.8 Prototype simulation – New air loop conditions 55
3.4.2 Prototype testing - Expander 56
3.4.2.1 Expander – Test rig set up 57
3.4.2.2 Expander – Test rig control procedures 58
3.4.2.3 Expander – Test results 59
3.4.2.4 Consequences of expander performance 63

3.4.2.5 Prototype simulation – New expander conditions 65
4. Conclusions 69
References 72
List of Figures 75
Appendix A: Additional test expander test results 77
Appendix B: Results from uncertainty analysis 80

List of symbols

Latin letters

A_1	Top surface area of expander cylinder [m^2]
A_2	Expander leakage area [m^2]
B_i	Systematic uncertainty of parameter *i*
B_r	Systematic uncertainty of data reduction equation
C	Coefficient of discharge [-]
d	Diameter of orifice [m]
D	Upstream internal pipe diameter [m]
DP	Pressure difference across expander [Pa]
E	Current efficiency [-]
F	Faraday constant = 96485 C/mol
g	Standard gravity [m/s^2]
G	Amount of produced off gas from aluminum electrolysis cells [$m^3/(s\ m^2)$]
$h_{friction}$	Friction head [m]
h_{pump}	Pump head [m]
$h_{turbine}$	Turbine head [m]
Δh	Enthalpy difference [J/kg]
H	Fluid height difference [m]
i	Anodic current density [A/m^2]
I	Current [A]
l	Pressure tapping spacing [m]
L	Relative pressure tapping spacing [-]
$\dot{m}$	Mass flow [kg/s]
$\dot{m}_{Al}$	Production rate of aluminum [kg/s]
Δm_i	Uncertainty of mass flow *i*
M_{Al}	Atomic weight of aluminum [kg/kmol]
n_{th}	Thermal efficiency [-]
P	Absolute static fluid pressure [Pa]
P_0	Reference pressure [Pa]
P_1	Pressure upstream of orifice [Pa]
P_2	Pressure downstream of orifice [Pa]
P_a	Applied pressure [Pa]
P_i	Random uncertainty of parameter *i*
P_r	Random uncertainty of data reduction equation
ΔP	Pressure difference [Pa]
ΔP_i	Uncertainty of pressure *i*
q_m	Fluid mass flow rate [kg/s]
Q	Heat duty [W]
r	Data reduction equation (page 29)
r	Radius of expander cylinder [m] (page 66)
R	Universal gas constant [J/(mol K)] (page 5)
R	Distance from expander cylinder centre to wall [m] (page 66)
Re_D	Reynolds number referred to D [-]

S_l	Leakage area [m^2]
T	Absolute temperature [K]
T_1	Temperature of heat source (Carnot cycle) [K]
T_2	Temperature of heat sink (Carnot cycle) [K]
ΔT_i	Uncertainty of temperature *i*
U_i	Uncertainty of parameter *i*
U_r	Total uncertainty of data reduction equation
v	Air velocity [m/s]
ΔV_i	Uncertainty of air volume flow *i*
W_{net}	Net work [W]
X_i	Variable in data reduction equation
z	Altitude [m]

Greek letters

β	Diameter ratio [-]
γ	Specific weight [kg/m^3]
ε	Expansibility factor [-]
η_{Carnot}	Carnot efficiency [-]
η_{is}	Isentropic efficiency [-]
κ	Isentropic coefficient [-]
ρ	Fluid density [kg/m^3]

Abbreviations

COP	Coefficient Of Performance
ORC	Organic Rankine Cycle
PWM	Pulse-Width Modulation
ROMA	Resource Optimization in the MAterials industry

1. Background – Aluminum production in Norway

The background for the Energy Recovery part of the ROMA (Resource Optimization and recovery in the MAterials industry) project is the energy use of and waste heat from the production of aluminum, preferentially in Norway. For this reason the following section gives a short resume of the production process of aluminum and the source of waste heat from the production of aluminum.

1.1 Historical background

The aluminum electrolysis process was invented in 1886 by the French P.L.T. Heroult and the American C.M. Hall and is therefore called the Hall-Heroult process.

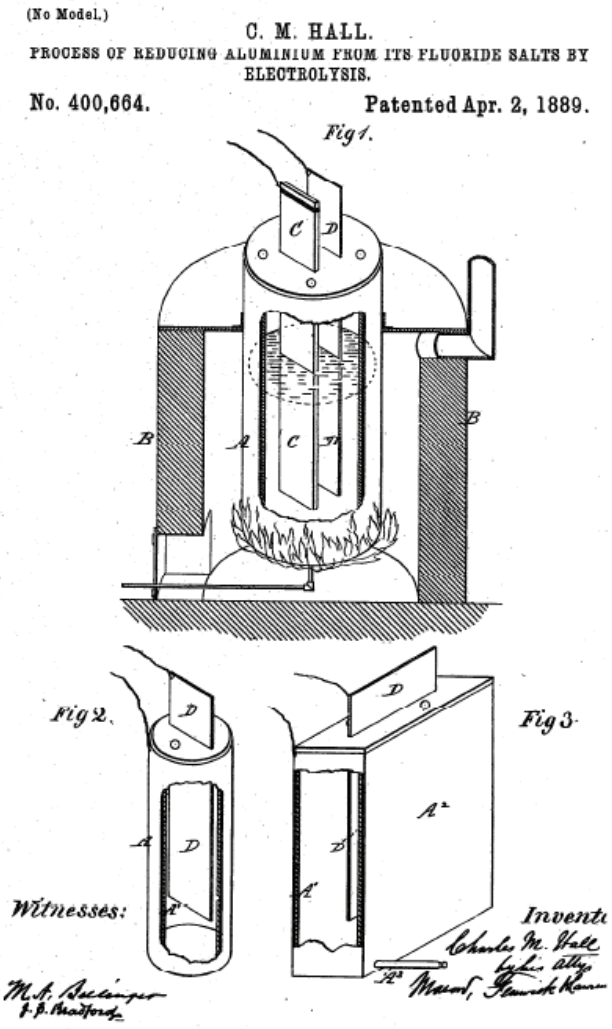
(No Model.)

C. M. HALL.

PROCESS OF REDUCING ALUMINIUM FROM ITS FLUORIDE SALTS BY ELECTROLYSIS.

No. 400,664. Patented Apr. 2, 1889.

Fig 1.

Fig 2.

Fig 3.

Witnesses:

Inventor

Figure 1: The patent on aluminum electrolysis developed by Charles Martin Hall in 1886. [1]

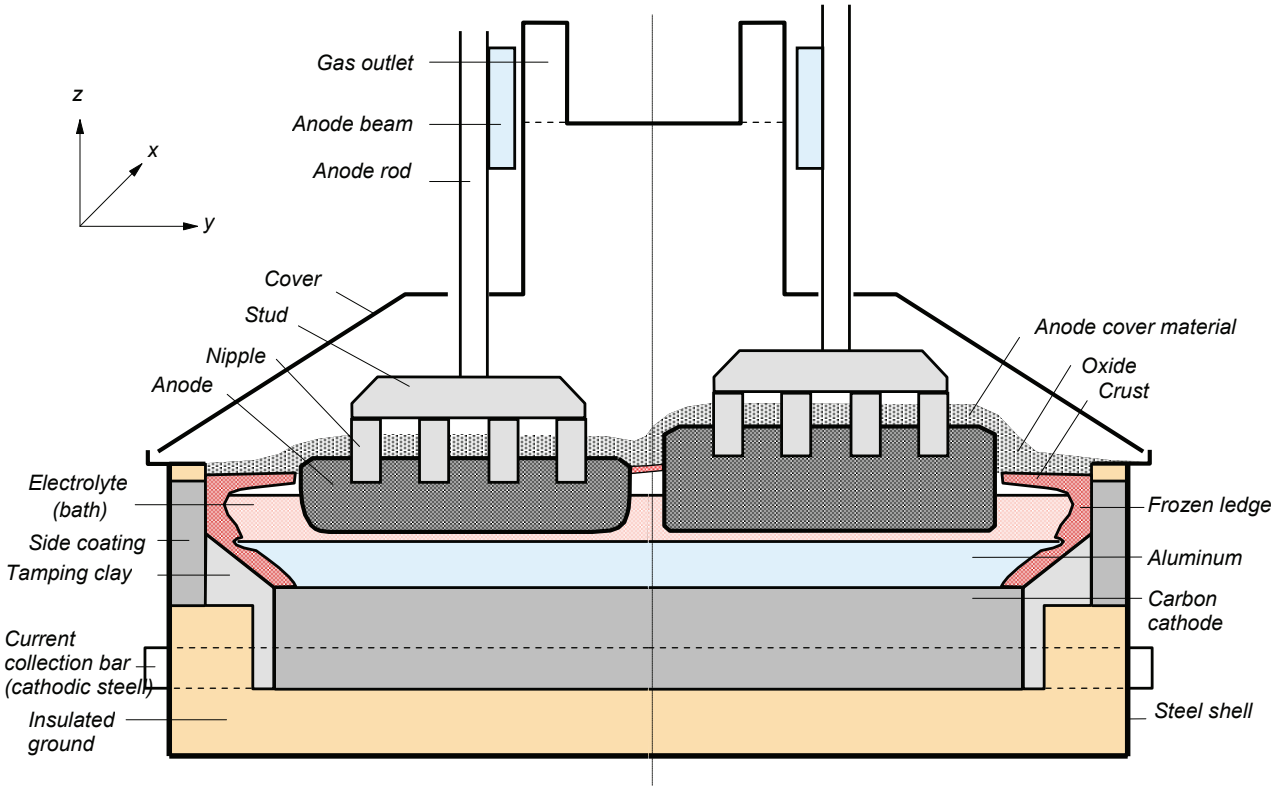

Figure 2: The cross-section of an aluminum electrolysis cell. [2]

1.2 The aluminum production process [2]

The main reaction in the aluminum process can be written as

Equation 1

$$\underset{1889}{Al_2O_3} + \underset{333}{\tfrac{3}{2}C} = \underset{1000}{2\,Al} + \underset{1222}{\tfrac{3}{2}CO_2}$$

The numbers below each chemical compound is the amount (in kg) per produced ton of aluminum. The theoretical (reversible) cell voltage for this reaction is 1,2 V, but due to the reaction being endothermic, the minimum possible cell voltage to run the reaction is 1,9 V. In reality, since one have to take into account over-voltages and ohmic losses, the number is closer to the range of 4 – 4,5 V.

The anode in the electrolytic reaction is made of carbon which is consumed in the reaction equation above. The carbon cathode at the bottom of the electrolysis cell is not consumed during the process. The electrolyte is a solution of molten cryolite, a chemical compound made out of aluminum, sodium, and calcium fluorides. The cryolite, which serves as the source for the ionic flow, has a temperature of about 960 °C in the electrolysis process.

The current flows in through the anode of the electrolysis cell, via the electrolyte and into the cathode carbon. From the cathode carbon the current goes into the conductor rail made of steel, where the biggest ohmic losses at the cathode are.

The side walls of the electrolysis cell consist of silicon carbide as the outer layer, and the inside of the cell is covered with solidified cryolite. Since both carbon and cryolite are good heat-conductors, a large heat loss occurs at the side walls of the cells.

The amount of aluminum produced in the process can be calculated from this equation:

Equation 2

$$\dot{m}_{Al} = \frac{I \cdot M_{Al} \cdot \varepsilon}{3F} \qquad \left[\mathrm{kg\,s^{-1}}\right]$$

In equation 2 I is the current, M_{Al} the atomic weight of aluminum, ε is the current efficiency and F is the Faraday constant. The current efficiency is the ratio between the current going into the production of aluminum, and the total current into the cell. The main source of reduction in current efficiency is the production of sodium gas at the cathode. The normal value of ε lies in the area of 0,9 – 0,96.

The electrochemical reaction at the cathode is:

Equation 3

$$AlF_3 + 3e + 3Na^+ \rightarrow Al + 3NaF$$

The electrochemical reaction at the anode is:

Equation 4

$$\frac{1}{2}Al_2O_3 + 3NaF + \frac{3}{4}C \rightarrow 3Na^+ + 3e + AlF_3 + \frac{3}{4}CO_2$$

From this it can be seen that the anode made out of carbon is continually used in the electrolysis process, and it has to be substituted when the size of the anode reaches a certain minimum. From these equations (as well as equation 1) it can also be seen that the product of the production process along with aluminum is CO_2 gas. The amount of gas produced [$m^3\ s^{-1}\ m^{-2}$] can be calculated from the following equation:

Equation 5

$$G = \frac{i}{4F} \cdot \frac{RT}{P}$$

Equation 5 is found by combining the ideal gas equation and equation 2. In this equation i is the anodic current density, F is the Faraday constant, R is the universal gas constant, T the absolute temperature and P is the pressure.

A typical value for the amount of gas produced is 0,00236 m^3/s per m^2 of anode surface. Typical dimensions of the anode can be; 1,6 meter long, 0,7 meter wide and 0,6 meter high. The gas produced leaves the electrolysis cell through the gas suction channels shown in figure 2. It is this off gas which is the waste heat considered to be used in a power producing cycle.

1.3 Energy flow in the aluminum process

The energy flow in a typical aluminum works can be summarized as in figure 3. Key points in this figure are the amount of electricity used in the production of aluminum, and the amount of energy which ends up as waste heat in the stack gases and flue gases.

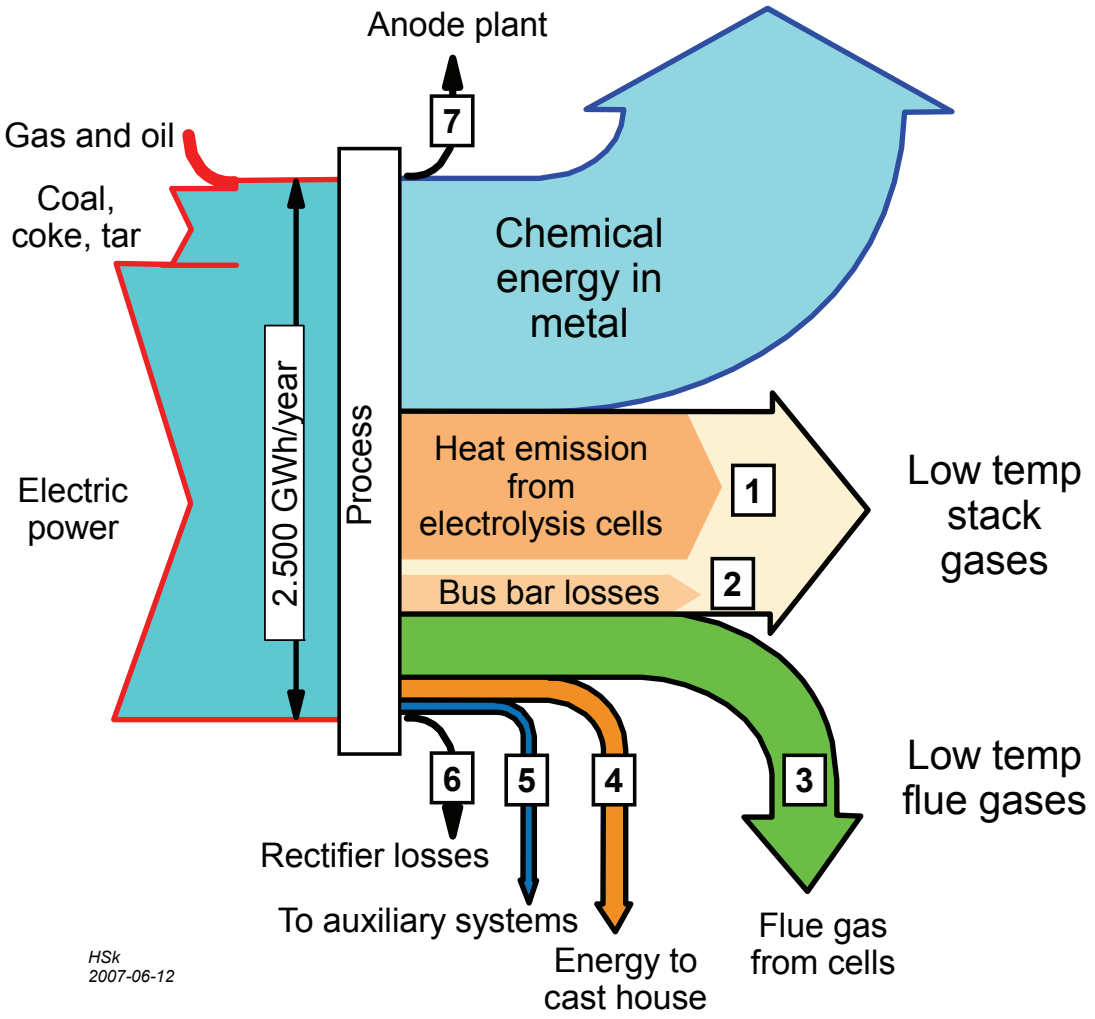

Figure 3: Energy flow in a typical Norwegian aluminum works which produces about 10 % of the total aluminum production in Norway. [3]

According to Minea [4], about 50% of the input energy is lost in the aluminum production process. Out of this amount about 2/3 is heat loss through the cell walls. The last 1/3 is flue gases at a temperature of 100-130 °C, with a good potential for energy

recovery. This is what the ROMA project is investigating further through the construction of a prototype power production system.

ENOVA [5] have done a study on the potential for utilization of waste heat in Norway. The waste heat is reported with 0 °C as the reference point. The total waste heat potential in the aluminum industry was found to be 2225 GWh/year. This amount is dispersed over a few temperature intervals as shown in figure 4.

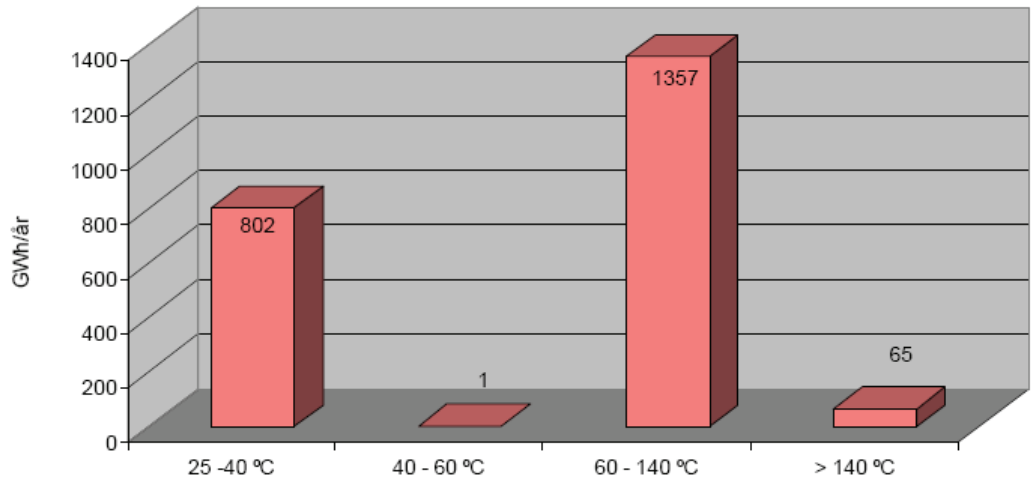

Figure 4: Waste heat in the Norwegian aluminum industry sorted by temperature intervals [5]

2. Waste heat to power – State of the art

2.1 Technical processes for waste heat recovery

There exists a set of technologies and scientific processes to produce electricity from waste heat. This section presents some of the more realizable and relevant technologies existing today.

2.1.1 Water vapor Rankine cycle

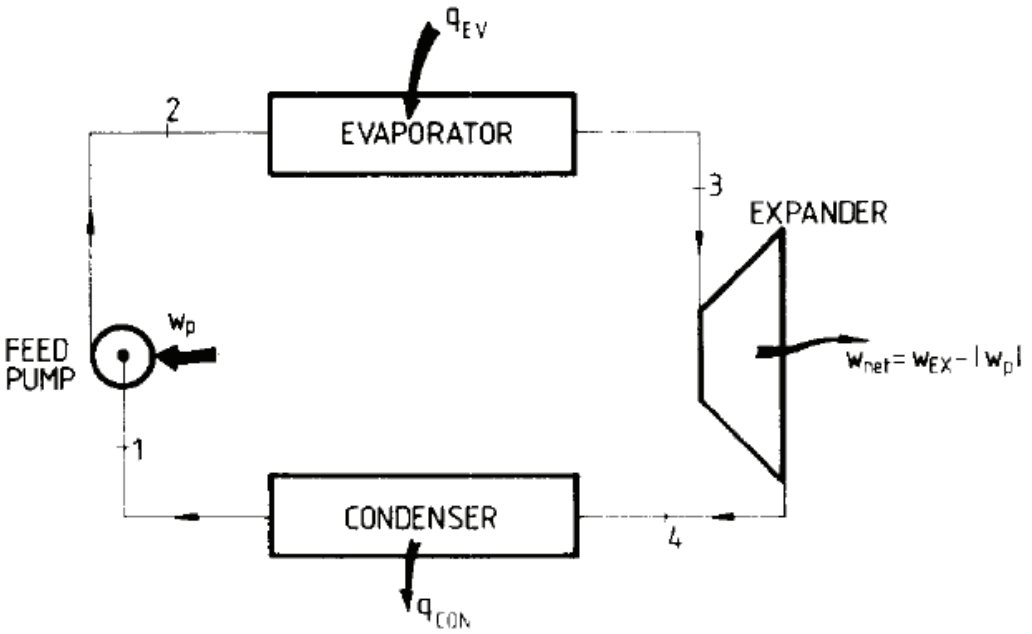

Figure 5: The Rankine cycle system. [6]

The steam Rankine cycle is a thermodynamic cycle where water is used as working medium. The cycle consists of four process steps. Water in liquid form is pumped from low to higher pressure in the first step. The pressurized liquid is then circulated through an evaporator where all of the liquid is evaporated by a heat source. The product coming out of the evaporator is high pressure water vapor. The next step is expansion of the vapor through a turbine/expander, where power is produced. From the expander the low pressure water vapor proceeds to a condenser, where it is condensed to liquid water which flows back into the pump.

The steam Rankine cycle is best suited for recovery of high grade waste heat. This is due to the condensing temperature at ambient pressure being 100 ° C and the need for superheat of the gas in order to avoid a wet expansion through the expander.

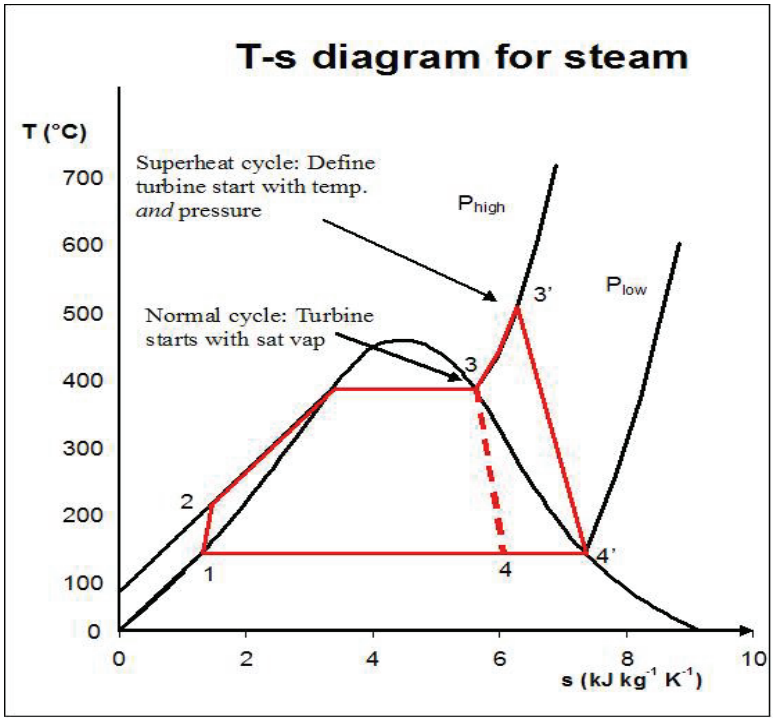

Figure 6: Entropy diagram for a steam Rankine cycle [7]

2.1.2 Organic Rankine cycle

The organic Rankine cycle (ORC) bares resemblance to the steam Rankine cycle as the working medium goes through the same four stages of the thermodynamic cycle. The main difference is the use of an organic medium, meaning a hydrocarbon, HFC etc. The introduction of an organic medium is to be able to better match the conditions of the waste heat source. This is due to the fact that most organic mediums have a lower boiling point than water when compared for the same pressure, i.e. a lower critical pressure. This also means that organic Rankine cycles operate with smaller heat capacities than the water vapor-cycle [8]. Hung [8] pinpoints that a larger latent heat of the working medium at low pressure means a lower thermal efficiency as more energy is being "dumped" in the condenser. A large specific heat of vaporization also implicates a poorer use of the waste heat as shown in figure 7.

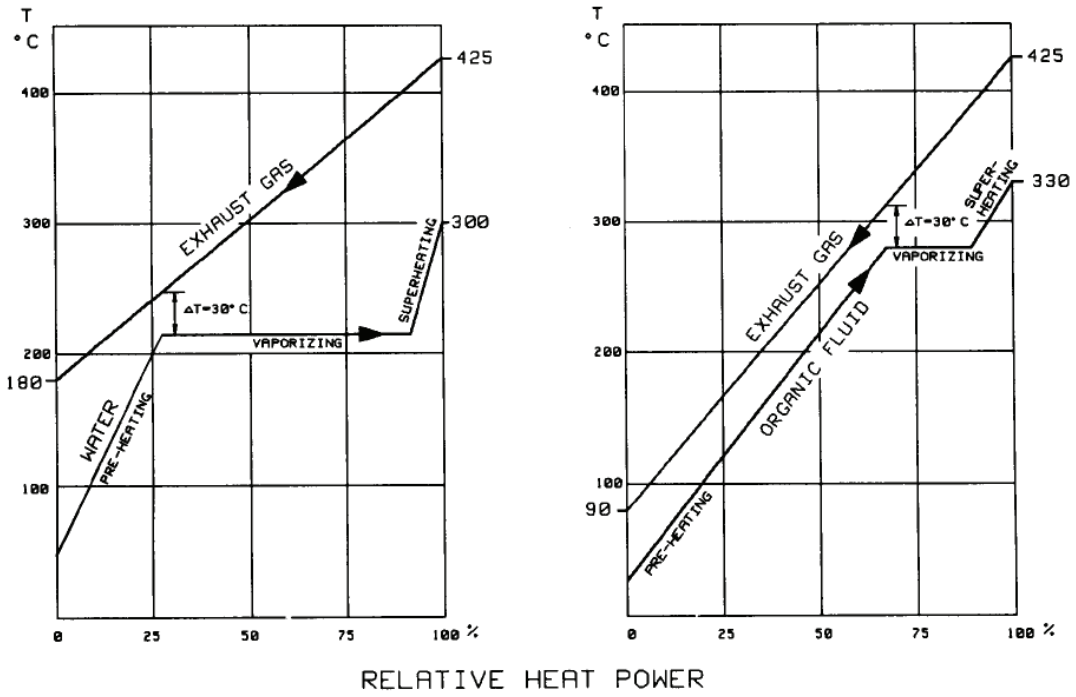

Figure 7: A comparison of the evaporation of water (left) and an organic fluid (right). Note that the organic fluid, due to the lower heat of vaporization, manages to cool the exhaust gas to a lower temperature than water manages. [9]

To avoid condensation through the expander outlet, the gas out of the evaporator has to be superheated. Due to the positive isentropic slope of the saturation curve for some organic fluids, the superheat of the gas going into the expander does not have to be as great as for water to avoid condensation [10].

There exists a large source of information based on theoretical and practical investigation of the organic Rankine cycle. Many reports are concerned with optimization of the organic Rankine cycle with respect to thermal and/or exergetic efficiency [8, 11]; others compare different working mediums with each other [6, 8, 12, 13].

One way to use the ORC is to have it working as a bottoming cycle for the water vapor Rankine cycle by utilizing the condensation heat from the water vapor Rankine cycle. This arrangement is shown in figure 8.

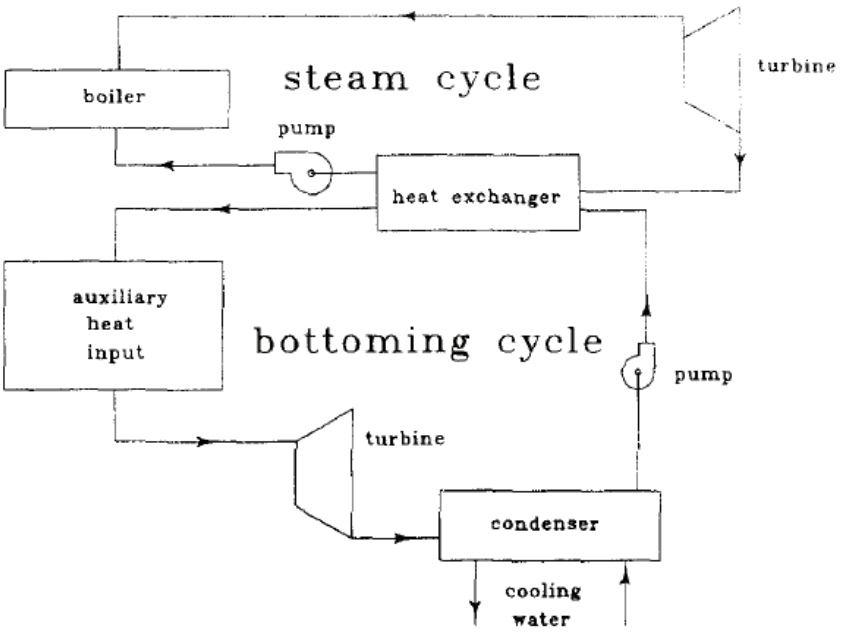

Figure 8: The organic Rankine cycle used as a bottoming cycle in the water vapor Rankine cycle. [14]

Another useful application of the organic Rankine cycle is in combination with geothermal reservoirs. For those reservoirs which produce hot water instead of steam, the ORC can be applied in binary cycle plants where the hot water serves as the heat source for the organic fluid in the evaporator. Barbier [15] writes that "…the binary power plant technology has emerged as the most cost-effective and reliable way to convert large amounts of low temperature geothermal resources into electricity...". Due to the fact that geothermal plants can be built economically in smaller scale than other comparable power plants; the most likely comparison are hydropower stations. There is especially a basis for this type of plants in developing countries where the electricity market still is small but increasing slowly [15].

Of the 9000 MW of total installed geothermal plants, around 1000 MW were from ORC or combined ORC/steam cycles in 2008 [16].

Larjola [9] points out that in many cases the turbine efficiency of ORC is almost twice as much as for the water vapor Rankine cycle when the unit output of the turbine is at moderate level, typically at 500 kW. Because the specific enthalpy drop for the organic fluid is smaller compared to the water vapor in the expansion process, the turbine design for the organic fluid is simpler and for smaller units the ORC can use a single-stage turbine whereas a water vapor cycle of the same output would need multi-stage turbine. It is also noted that the majority of waste heat sources has an available electric output below 1 MW. This gives the ORC an advantage when it comes to generate electricity from waste heat.

2.1.3 The Kalina cycle

The main theory on the Kalina cycle is taken from Watts [17] unless otherwise noted.

As shown in the previous section, a thermodynamic cycle where the boiling process of the working fluid better follows the temperature glide of the heat source helps to improve the utilization of the heat. For a pure substance boiling at a constant pressure (and a pressure below critical pressure), the temperature is constant as the substance goes from liquid to gaseous state; the substance/medium is said to be azeotropic.

The Kalina cycle addresses this problem by introducing a non-azeotropic medium. In the Kalina cycle this medium is a water/ammonia mixture, chosen for its fitting characteristics for operation in a power cycle, and because information and knowledge on the behavior of the mixture is substantial. What is critical when choosing a working fluid or mixture for this application is to know if it is suitable for operation in a turbine. The working fluid has to be stable at the turbine inlet conditions (pressure and temperature).

The Kalina cycle consists of four processes. The working fluid (mixture) is evaporated in a boiler; the gaseous product is then taken through a turbine for where power is produced; the working fluid flows through a condenser/absorber arrangement and finally the condensed mixture is pumped back to the boiler.

The chemical composition of the water/ammonia mixture in the Kalina cycle varies in the different parts of the cycle. In the boiler section of the cycle, the mixture is rich on ammonia (close to 70 % solution of ammonia in water; [18]). When heat is provided in the boiler, the water and ammonia boils off at different rates, which in turn changes the chemical composition of the fluid mixture and the boiling temperature rises.

In the condensation process, the arrangement is a bit more complex (a schematic diagram is shown in figure 9). A bit simplified the, condensation process happens in two steps. The first step is a condensation/absorption process where a weak water-ammonia solution is used as the absorbent and the strong water-ammonia solution coming from the turbine outlet is absorbed. After the weak and strong solution has been “separated” in a flash vessel, the strong solution is further condensed (at a higher pressure than in the absorber) in a separate condenser unit before being pumped to the boiler.

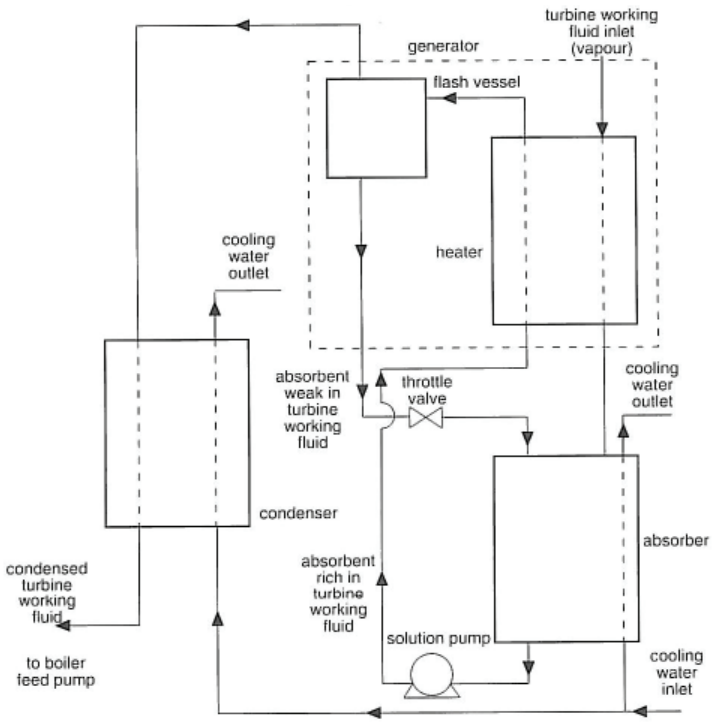

Figure 5.1 *Schematic diagram of the Kalina cycle's condensing arrangement*

Figure 9: Schematic diagram of the Kalina cycle's condensing arrangement [17]

The first commercial power plant to use the principle and technology of the Kalina cycle (the second grand scale implementation of Kalina cycle [19]) was built in Husavik, Iceland, and started producing power in 2000. It uses geothermal brine at a temperature of 121 °C and mass flow rate of 90 kg/s. Exergy Inc., the company behind the plant technology, reported a net power production of about 2000 kW in 2001 [20].

Some challenges related to this technology have already surfaced. One is related to the sealing gas used in the turbine to prevent contamination of the process fluid by the lubricant. Inert nitrogen is used as the sealing gas, and this means that the ammonia has to be recovered from a mixture of nitrogen, water and ammonia [4]. The Husavik plant has also had some problems with corrosion to the turbine, as the water-ammonia mixture can be highly corrosive [21].

The Kalina technology is still in an early stage and experience gathered from power plants, both commercial and scientific, will be useful in the future evaluation of this technology. For now there is too little (neutral) information available to make any conclusions. [22]

2.1.4 Misc gas cycles

2.1.4.1 Brayton cycle

Since the Brayton cycle is a gas cycle, this means that there are no phase changes in the cycle process stages. The Brayton cycle consists of four main stages. The first stage is

(ideally) an isentropic compression of the gas from low pressure to high pressure. Then the high pressure gas is heated under constant pressure. The gas is now at the highest energy level. The next stage is expanding the gas through a turbine (ideally an isentropic expansion), and by this generating power. The last step for a closed cycle is to cool the low pressure gas down to the initial temperature.

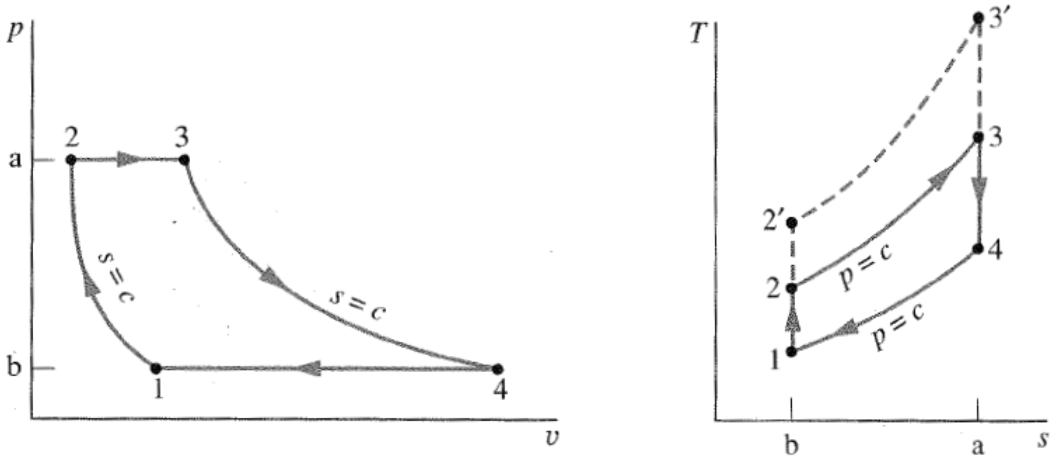

Figure 10: Schematic representation of the ideal Brayton cycle in a pressure-volume diagram (left) and a temperature-entropy diagram (right). [23]

For an open cycle (usually the air-standard Brayton cycle), the high temperature low pressure gas exiting from the turbine is released to the ambient. The air at the inlet of this open cycle is taken from the same surroundings.

Design work on turbo-machinery with the idea of a Brayton cycle with super-critical CO_2 as working media in mind, has been carried out [24], mainly due to promises of high efficiency and compact machinery. The machinery has been designed for the lower pressure level of 80 bar, an upper pressure level of around 200 bar and a temperature range between 30 °C and 550 °C. One of the main difficulties regarding compressor design is the major change in density with change of temperature near critical temperature and pressure (see figure 11).

The Brayton cycle is mostly relevant when the heat source is at high temperatures.

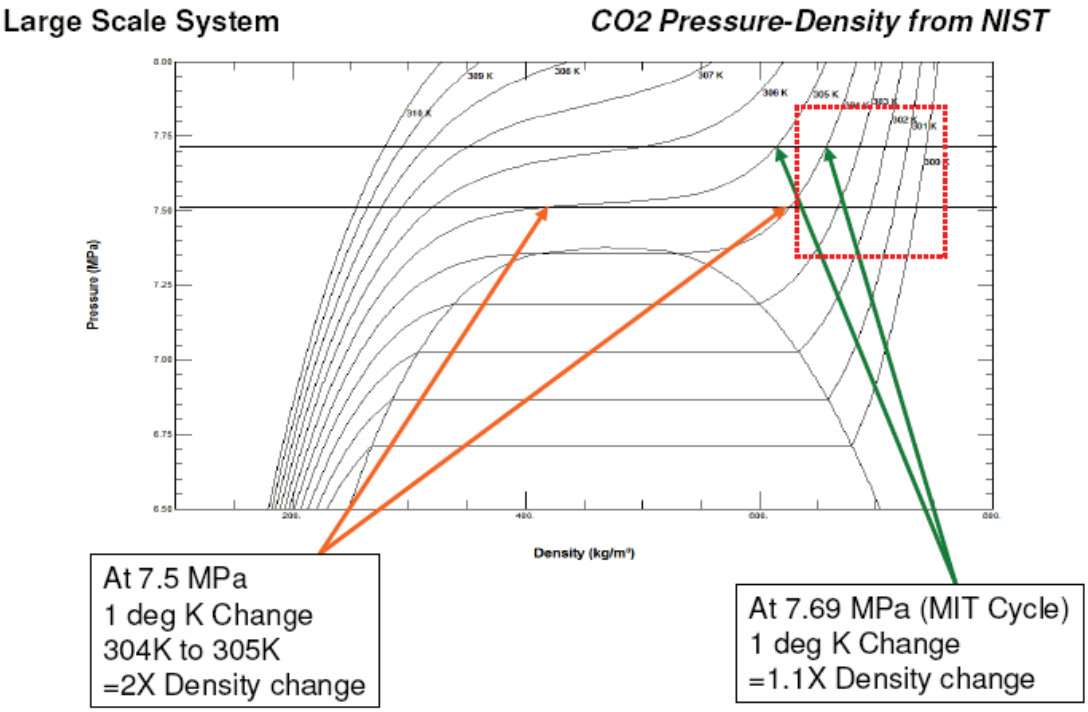

Figure 11: Pressure-density diagram showing the pressure dependency of density change due to incremental temperature variation. [24]

2.1.4.2 Stirling cycle

The first step of this gas cycle is an isotherm compression of the gas. This is opposed to the Brayton cycle where the gas is being compressed isentropic (resulting in a temperature rise). Then heat is added to the gas at constant volume. This means that the pressure increases even further, to the highest pressure of the cycle. From this state the gas is going through an isotherm expansion where power is being generated. The last step of this cycle is a heat release at constant volume and therefore at decreasing pressure. All four steps in the ideal Stirling cycle are reversible. The cycle as a whole is seen as fully reversible if the constant volume heat rejection is absorbed by the constant volume heating through a regenerator with 100 % effectiveness.

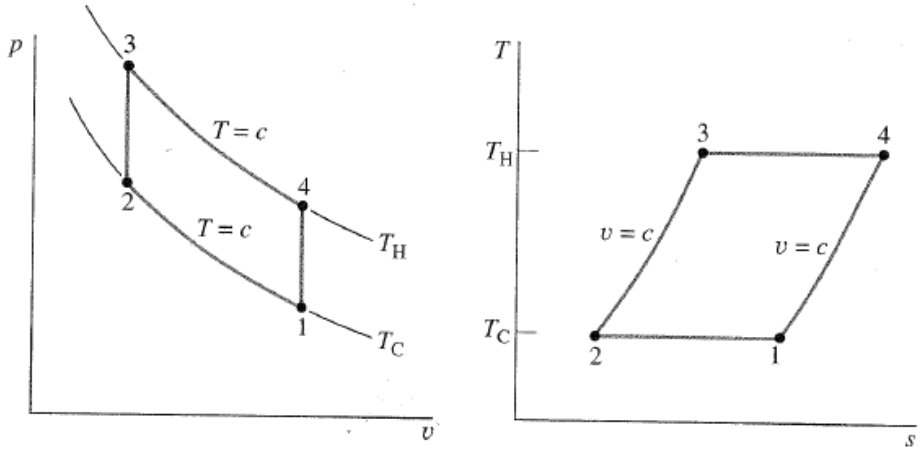

▲ **Figure 9.25** *p–v* and *T–s* diagrams of the Stirling cycle.

Figure 12: Pressure-volume diagram (left) and temperature-entropy diagram (right) of the Stirling cycle. [23]

Stirling engines are, as Brayton process, appropriate where high temperature heat is available; there have been reported difficulties with transferring heat to the engine. The Stirling technology for waste heat recovery has not made much commercial impact at the moment [25].

2.1.5 The ideal power cycle and its fundamental constraints

The theory of this section is found in [17] unless otherwise mentioned.

To be able to compare the usefulness of the different processes to each other, a reference process is needed. When considering a thermodynamic process where work is extracted from heat transferred from a high temperature reservoir to a low temperature reservoir, the Carnot cycle is a much used ideal.

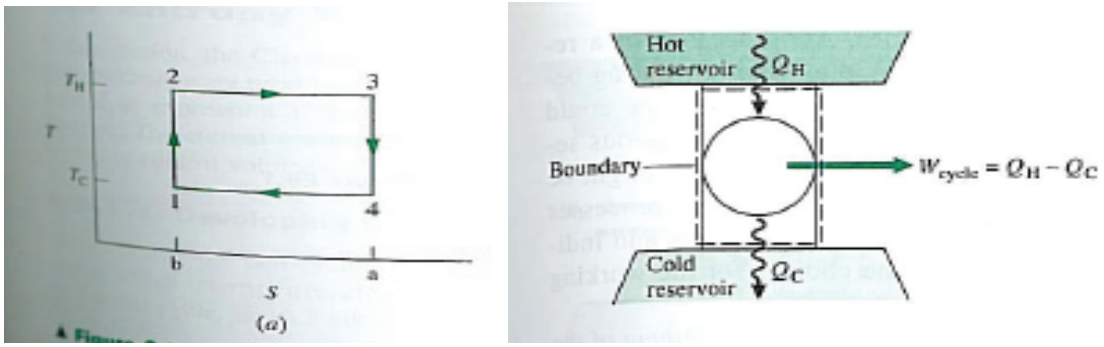

Figure 13: The Carnot cycle illustrated in a temperature-entropy diagram (left) and a schematically representation (right) [23]

In this ideal cycle heat is transferred to a work producing cycle at a constant high temperature and ejected to a cold reservoir at a constant lower temperature. Work is taken

out in a reversible process where the entropy is constant (isentropic process), and the working fluid is also pressurized in a reversible process, at constant entropy.

But since the heat source more often than not is available only in a limited amount (and this most notably corresponds to the limited waste heat off gas from aluminum production plants), the principal of extraction of heat from the high temperature heat source at a constant temperature is not fully comparable. Therefore the ideal trilateral cycle is being used as a more relevant ideality to compare with.

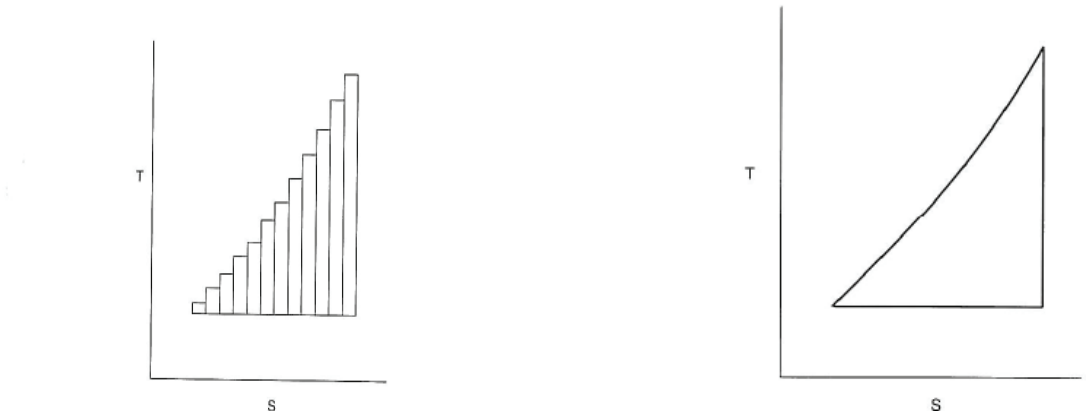

Figure 14: The ideal trilateral cycle; as a composition of infinitesimal Carnot cycles (left) and on integral form (right) [16]

The ideal trilateral cycle can be seen as a composition of infinitesimal Carnot cycles, where each cycle operates between successively reduced temperature limits.

Since both the Carnot cycle and the ideal trilateral cycle are idealized cases, in the real world one is bound to experience deviations from these. Both thermodynamic constraints and practical limitations move the practical cases away from their idealized counterparts.

Some of these limitations are:

- Temperature differentials needed to transfer heat from heat source to working medium and from working medium to heat sink.
- Poor temperature matching between the heat source and the working fluid.
- Friction and leakage effects in the turbo machinery, giving a lower work output than the reversible isentropic process.
- Auxiliary power requirements, i.e. power needed to circulate cooling fluid for the heat sink.
- Non-isentropic pressure machinery.

In order to give a value for real power cycles to compare against these idealized cycles, thermal efficiencies have been introduced. These are defined as net work output divided by the heat delivered to the cycle.

If the temperature of the heat source is defined as T_1 and the temperature of the heat sink is defined as T_2 the efficiency of the Carnot cycle (Carnot efficiency) is given as:

Equation 6

$$\eta_{Carnot} = \frac{T_1 - T_2}{T_1}$$

The efficiency of the ideal trilateral cycle is then:

Equation 7

$$\eta_{Trilateral} = 1 - \frac{T_2 \ln\left(\frac{T_1}{T_2}\right)}{T_1 - T_2}$$

A graphical representation of these two efficiencies for a heat sink temperature (T_{min}) equal to 300 K is given in figure 15:

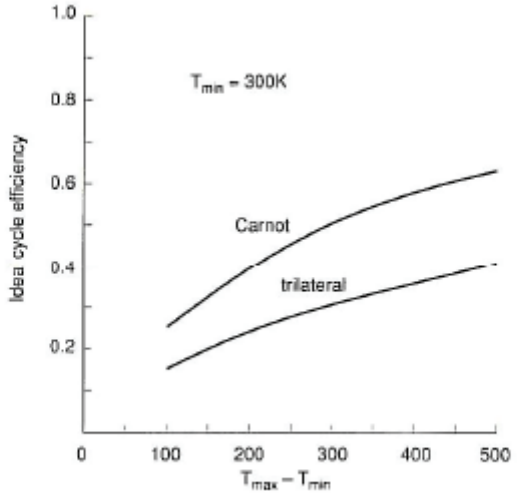

Figure 15: Graphical representation of the ideal Carnot and trilateral cycle efficiencies [20]

3 ROMA project – Waste heat to power production system prototype

3.1 Concept – The CO_2 trans-critical Rankine cycle

The power production prototype is based on the thermodynamic principle of a trans-critical Rankine cycle, with CO_2 as working medium. This section gives a description of this cycle and why it is the preferred thermodynamic cycle for this project.

3.1.1 Thermodynamic description

The Rankine cycle, as described earlier, is a thermodynamic cycle where a working fluid goes through four specific processes. Starting with the working fluid as a sub cooled liquid at low pressure, the fluid is pumped up to a pressure above critical pressure. At this pressure the liquid flows through an evaporator/gas heater where it is heated by an external heat source (in a heat exchanger arrangement). Out of the heat exchanger the working fluid is at a state of high pressure, high temperature gas. From this state the hot gas is expanded through a turbine/expander where work is extracted and the fluid leaves at a lower pressure than when entering. The low pressure gas then flows through a condenser where the fluid is condensed to liquid form before entering the pump, completing the thermodynamic cycle. The trans-critical Rankine cycle is shown in a pressure-enthalpy diagram below:

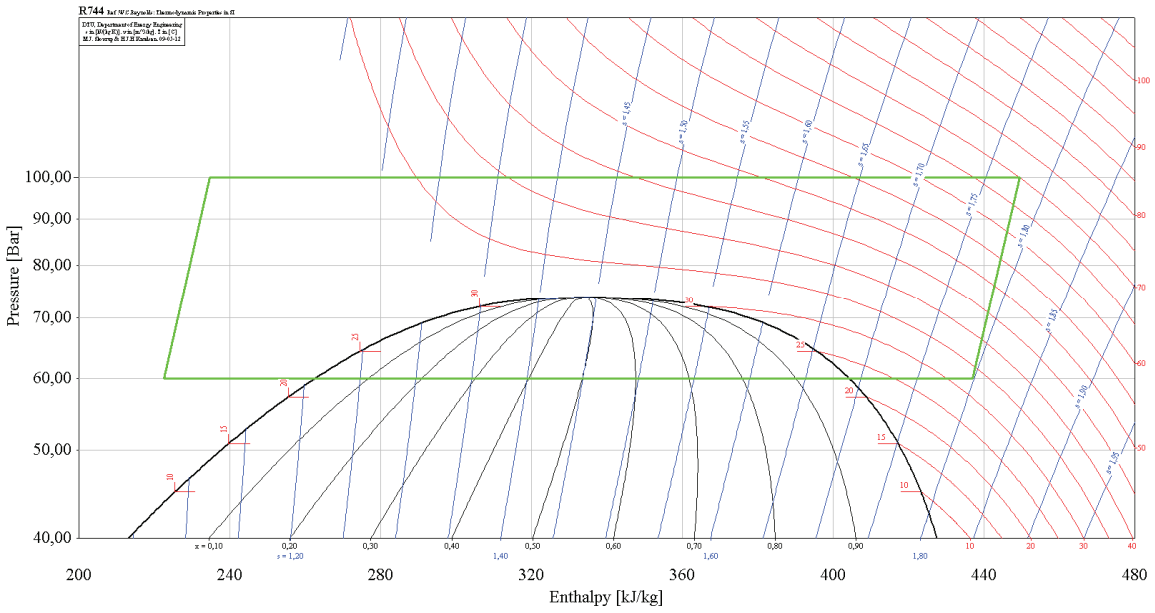

Figure 16: The trans-critical Rankine cycle (green lines) shown in the logarithmic pressure–enthalpy diagram for CO_2. Red lines indicate the constant temperature (isotherms), while the blue lines indicate the constant entropy (isentrops).

Some of the properties of CO_2 as a working fluid is that it has a low critical temperature (31,1 °C) and a relatively high pressure level (73,8 bar at critical temperature). Some advantages for CO_2 as a working medium [26]:

- High density gives high volumetric performance factor (lower flow rate) and smaller pipe diameter.
- The heat transfer coefficient is high for CO_2 in general, especially for boiling and condensation processes. This has a positive effect on the design of heat exchangers.

Some disadvantages with CO_2 as a working medium [26]:

- High pressure level increases the wear and tear on everything from pumps to pipes to heat exchangers. High pressure level also demand thicker pipes.
- CO_2 has the tendency to dissolve into the lubrication oil. This decreases the viscosity of the oil.
- At high pressures the CO_2 might diffuse into ring gasket material and form small gas pockets. By a small altering to a lower pressure, the trapped gas expands with the result that the gasket material might crack. This is called explosive decompression.

3.1.2 The benefits of working trans-critically

In chapters 2.1.2 and 2.1.5 it is pinpointed how important the temperature match between the heat source and the working medium in a thermodynamic cycle is to the utilization of the heat source. This is why the organic Rankine cycle is preferred to the water vapor Rankine cycle at low temperatures. Due to the organic fluids smaller specific heat of evaporation compared to water at low temperatures, the temperature match between the heat source and the working medium is better, as seen in figure 7.

Another way to obtain a close to trilateral cycle is to have a working medium which "evaporates" at a pressure above critical pressure. When a fluid is heated at a pressure above the critical pressure, the transformation from compressed liquid to compressed gas happens at gliding temperatures. The trans-critical process is shown compared to a conventional process in figure 17.

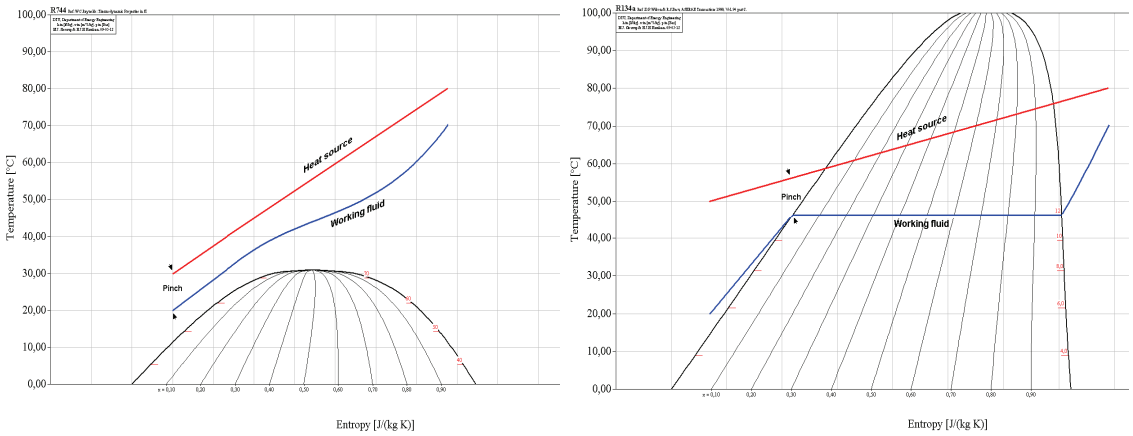

Figure 17: Temperature-entropy diagram for a trans-critical heating of working fluid (left) and a conventional process with heat transfer to a working fluid inside two-phase area

The figure shows that as heat flows from the heat source (red line) to the working fluid (blue) line, the heat source temperature declines. For the case where the working fluid is at a pressure above critical pressure (left) the temperature of the working fluid increases as heat is absorbed. For the conventional process (right) the working fluid temperature increases until the fluid is saturated liquid. From here on the heat evaporates the working fluid at a constant temperature (isothermally) until the fluid is at the state of saturated gas. Further heating of the working fluid increases the gas superheat.

When comparing the two processes shown in figure 17, what matters the most is how much heat it is possible to extract from the heat source. The amount of heat extracted is proportional to the temperature difference between the inlet temperature of the heat source going into the heat exchanger and the outlet temperature of the heat source. How much it is possible to cool the heat source is dependent on what is called the pinch. The pinch is the smallest temperature difference between the heat source and the working fluid in the heat exchanging process. If the pinch can be moved to either sides of the boiler inlet/outlet by adjusting the pressure of the working fluid, this will enhance the utilization of the heat source. For the conventional process the utilization of the heat source is limited by the isothermal boiling.

3.1.3 Challenges related to the cycle

Building a prototype for the CO_2 trans-critical cycle involves some challenges. Since this is a prototype in a KMB project (Knowledge-building project with user involvement), this indicates that this is an undeveloped area in waste heat recovery technology. The combination of high temperatures and high pressures is one challenge which demands special care in choosing of components for the prototype rig.

The main part in the power cycle is the expander. There is little experience and expertise available when it comes to making an expander which suits the conditions of the power cycle. As a result of this, part of the testing and evaluation of the laboratory prototype involves investigation of the expander.

3.2 Prototype rig

In the following section a presentation of the ROMA prototype rig, its objectives and how they are solved is given.

3.2.1 Prototype design

A brief description of the laboratory scale prototype, or test facility, is given in the following section. A more detailed review of the control strategy of the test facility is given later in the report.

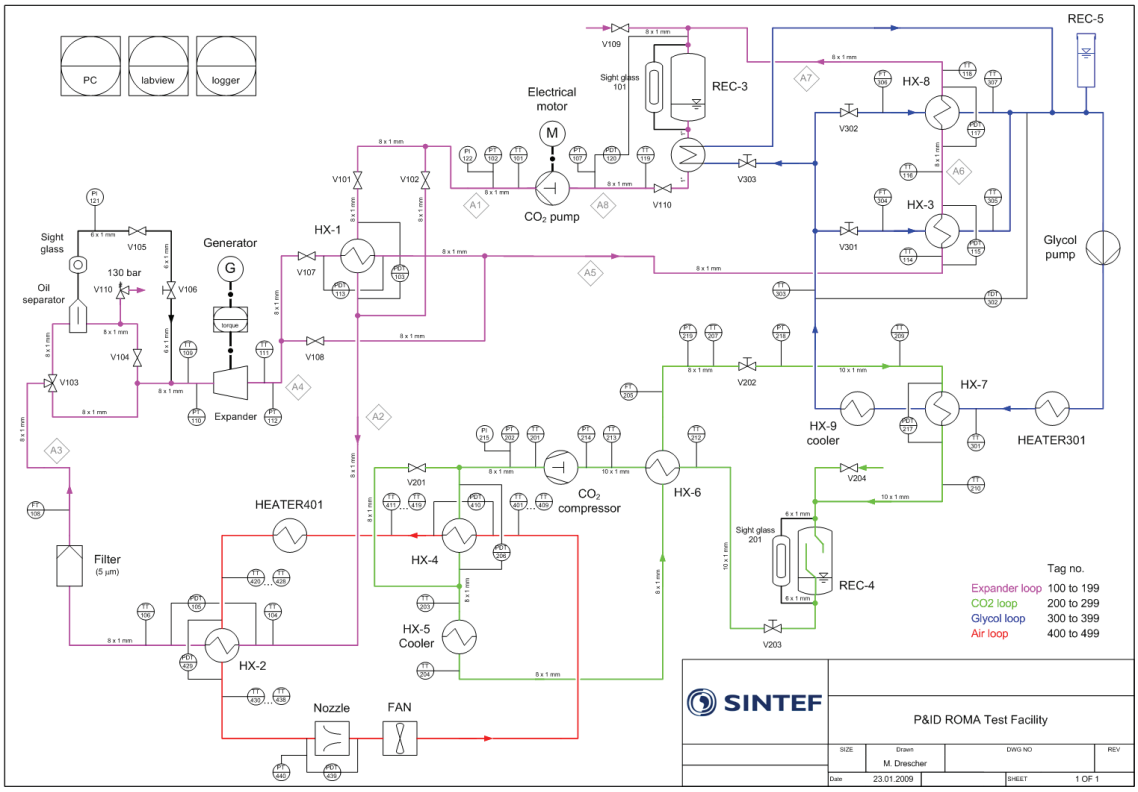

Figure 18: Drawing of test facility, showing the CO_2 power cycle as purple lines, the CO_2 heat pump as light green lines, warm air loop as red lines and ethylene glycol cycle as blue lines. The dark green lines show the control equipment.

3.2.1.1 Main process – CO_2 power cycle

At the center of design of the test facility is the CO_2 power cycle. This cycle is marked with purple lines in figure 18.

The CO_2 power cycle, or work recovery circuit, consists of several units put together, but at the core is the expander. The testing of the expander is one of the main focuses of the project, and the rest of the components are auxiliary units which provide the desired conditions for the testing of the expander. The power cycle exchanges heat with a heat source (HX-2) and a heat sink (HX-3 and HX-8) through several heat exchangers. To increase the performance of the power cycle a regenerator is also being installed (HX-1). A pump is installed after the condensation heat exchangers (HX-3 and HX-8) to control the mass flow in the circuit.

There is a receiver installed after the condensers. To ensure that there is only liquid at the pump inlet, there is a built-in static pressure height between the receiver and the pump. In addition a coaxial heat exchanger (to sub cool CO_2) is built on the pipes going down to the pump as an extra precaution.

3.2.1.2 Supporting circuits – Ethylene glycol and warm air circuits

The ethylene glycol circuit – cooling circuit
The main measure for the ethylene glycol circuit (blue lines in figure 18) is to function as a heat sink for the CO_2 power cycle. This is done by circulating ethylene glycol, with the aid of a pump, through the two heat exchangers HX-3 and HX-8. The mass flow distribution between these two heat exchangers is controlled with a set of valves. In HX-3 and HX-8 the ethylene glycol condenses the CO_2 so that the product CO_2 going from those heat exchangers to the pump is sub cooled liquid.

The removal of heat from the ethylene glycol is done either in the HX-7 heat exchanger if the heat pump is in operation (see figure 18), or it is cooled with cold water in the HX-9 heat exchanger. The heat pump is described more closely in chapter 3.2.1.3. As a supplementary solution, cold ethylene glycol can be used to sub cool the CO_2 in the power cycle after the receiver to ensure that only liquid gets into the CO_2 pump (when condensation temperature is lower than room temperature). This supplementary circuit can be opened with a valve.

The warm air loop
The warm air loop's (red lines in figure 18) primary function is to act as the heat source for the CO_2 power cycle. The heat exchanging with the power cycle is done through the HX-2 heat exchanger. When the heat pump is running, the air is warmed up in the HX-4 heat exchanger by the hot CO_2 gas running in the heat pump. If there is need for supplementary heating to obtain the desired temperature of the air, the electric heater provides the rest of the heat needed. In the case where the heat pump is not running the heater provides all of the heat needed. The circulation of the air is provided by an air fan installed right in front of HX-4.

3.2.1.3 Supplementary circuit – CO_2 Heat pump

As mentioned above, the power cycle collects heat from hot air on the high pressure side of the cycle, and releases heat to an ethylene glycol cycle. Between the air loop and the cooling cycle a CO_2 heat pump is planned to operate. The main reason for this is to recycle as much as possible of the condensation heat of the power cycle.

The main working components of a heat pump are the evaporator, the condenser, the compressor and an expansion device. In this circuit the HX-7 heat exchanger works as the evaporator, ethylene glycol provides the heat to the CO_2. The condensation takes part in the HX-4 heat exchanger where CO_2 is cooled by air from the warm air circuit, and in the HX-5 cooler where CO_2 is cooled even further (if needed) by cold water. The compressor unit used is a semi hermetic radial piston compressor with fixed

displacement. The expansion device is a prototype expansion valve. In addition there will be installed an internal heat exchanger (HX-6), to increase the performance of the heat pump and to dry the CO_2 gas entering the compressor. There is also a receiver in place between the evaporator and the internal heat exchanger working both to provide saturated gas to the internal heat exchanger and to account for changes in condition in the low pressure end of the heat pump.

3.2.2 Prototype control strategies

In order to have a well functioning test facility, it is necessary to work out control strategies for the different circuits of the test facility, leading up to a control strategy for the test facility as a whole.

The test facility consists, as previously mentioned, of four different circuits which interact with each other. The key objective is to optimize the power cycle in regards to work output. When the power cycle is the main concern, the warm air loop and the ethylene glycol cooling circuit act as boundary conditions to the power cycle, and they are controlled with this in mind.

The heat pump is to take advantage of the heat delivered to the heat sink by the power cycle, and providing heat to the warm air loop. In addition it can be used to increase the temperature difference between the heat source and the heat sink. The working conditions of the heat pump are results of the boundary conditions set for the power cycle.

3.2.2.1 Boundary conditions

Heat source - Warm air loop

The warm air loop defines the boundary condition on the high pressure side of the power cycle. This is done in form of heat made available in the heat exchanger between those two circuits (HX-2), by controlling the temperature as well as the mass flow of air into the heat exchanger.

The temperature of the air into the heat exchanger is controlled by the electric heater situated right in front of HX-2. The heater is regulated on the basis of a temperature sensor at the heater outlet. The temperature measured at this sensor is compared to a set point temperature chosen by the rig operator, and based on the difference between these two temperatures a regulator gives input signals to the heater. The heater then switches the heater elements on and off as a result of these signals, using pulse-width modulation (PWM) to control the amount of power sent to the load.

The volume flow is controlled by the air fan inserted in the loop in front of HX-4. The mass flow is a function of both volume flow (which is the parameter controlled by the fan) and the specific volume of air at the fan inlet. The specific volume of air is a function of temperature and pressure (in the temperature of interest the specific volume might vary between 0,9 and 1,3 m^3/kg depending on the humidity). This makes it a bit more complicated to control the mass flow as the fan has to account for the variations in

the temperature at the fan inlet when setting the rotational speed. The rotational speed of the fan has a range between 0 Hz and 50 Hz.

Heat sink – Ethylene glycol cooling circuit
The other boundary condition for the power cycle is the ethylene glycol circuit which operates as a heat sink. This circuit has one target which is to sub cool the CO_2 to 10 °C below saturation temperature. This is done in two heat exchangers (HX-3 and HX-8) which operate in parallel relative to the ethylene glycol circuit and in series relative to the power cycle. The amount of cooling is controlled through the mass flow of ethylene glycol circulated in the circuit. The circulation is provided by a single pump.

In addition to the pump, there is an option to regulate the distribution of ethylene glycol through the two heat exchangers with a set of valves. This is done in order to decide which heat exchanger should account for the major part of the cooling. The optimal regulation is when HX-3 does most of the condensation of CO_2 and HX-8 sub cools the CO_2 liquid. The reason for this set up is because condensation and sub cooling are two different heat exchanging processes, each with their own characteristics. The most important difference is the much higher heat transfer coefficient for the condensation process. This means that the heat specific heat exchanger area of HX-3 can be less than for HX-8, while for HX-8 the heat exchanger configuration is of a bigger importance. HX-8 is modeled as a fully cross-flow heat exchanger.

3.2.2.2 Main process – CO_2 power cycle

With the boundary conditions set, the power cycle can be regulated with the aim to produce maximum net work. This is done, as seen from the simulations, by regulating the mass flow of CO_2 and the high pressure. The mass flow is controlled with the pump while the high pressure is regulated by regulation of the load of the generator coupled to the expander unit (the torque).

The pump is actually a volume flow controller; the mass flow is a result of both the volume flow and the specific volume of CO_2 at the pump inlet. The CO_2 at the pump inlet is in liquid phase, thus the specific volume varies very little with varying pressure and temperature, and the mass flow of CO_2 can be controlled solely by controlling the volume flow through the pump.

The low pressure level is self regulating. A relatively high pressure in the condenser units means that the temperature difference between the working fluid (CO_2) and cooling (glycol) fluids will be large, and the condensing rate will exceed the rate of CO_2 going through the expander. This will result in a fall in pressure towards a stable level where the condensing rate is equal to the rate of CO_2 let through the expander.

3.2.2.3 Supplementary circuit – CO_2 Heat pump

The heat pump can be regarded as a supplementary circuit to the power cycle, as the power cycle can be operated without the heat pump running. In such a case there is need for external cooling of the ethylene glycol circuit, which is done with the use of cold

water in the HX-9 cooler. In the warm air loop, the electric heater would have to provide all of the heating.

The heat pump works between the ethylene glycol circuit and the warm air loop, and they therefore set the boundary conditions for the heat pump. The working medium in the heat pump is CO_2. The parameters controlled for the heat pump are the mass flow and the high pressure.

The mass flow is a function of the volume flow and the specific volume of CO_2 at the inlet of the compressor. The volume flow is regulated with the compressor, and therefore by considering the state of the CO_2 at the compressor inlet, the mass flow can be regulated through speed control of the compressor.

The high pressure is a combined result of the expansion valve opening at the inlet of the evaporator and the compressor speed. But the high pressure can also be increased or decreased by changing the amount of CO_2 filled into the system.

On the low pressure side the heat pump absorbs heat from the ethylene glycol. The available heat is decided by the ethylene glycol circuit as this is the product of mass flow and available enthalpy difference. [23]

Equation 8

$$Q = \dot{m} * \Delta h$$

3.3 Prototype simulation and uncertainty analysis

Ahead of this Master thesis, a project work was done which focused on simulation and uncertainty analysis of the prototype rig. The main results from that work are presented in the following section.

3.3.1 Prototype simulation

To have relevant experimental data for use in the uncertainty analysis and to have helpful data for the dimensioning of the facility, a simulation of the test facility was carried out. To help with this simulation, the process simulation tool PRO/II® was used. With the help of a graphical interface, a model of the complete facility was made. The model was simulated for three different warm air temperatures, 80 ° C, 120 ° C and 160 ° C. The results from these simulations were then used as raw data in an uncertainty analysis spreadsheet. In addition the results were used in calculations of pipe dimensions and charge. The construction of the prototype rig in PRO/II for simulation is shown in figure 19.

The power cycle was optimized with regards to maximizing net work of the cycle. The heat pump was optimized with regards to maximizing the coefficient of performance (COP).

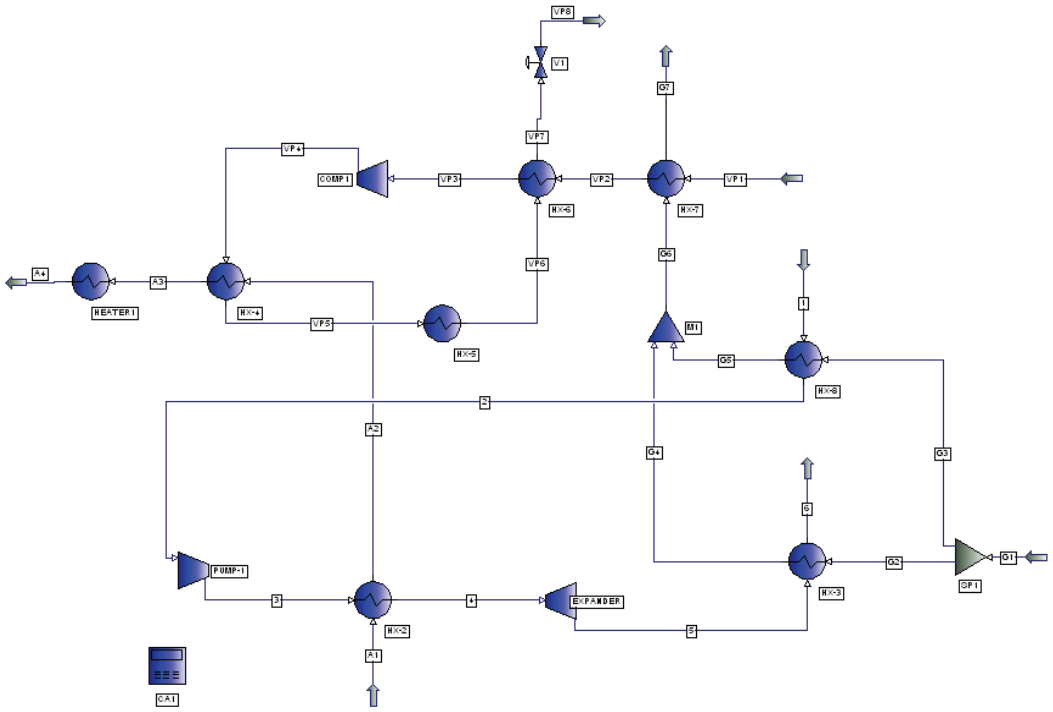

Figure 19: Graphical set up of test facility in the process simulating tool PRO/II.

In the simulation of the test facility some initial simplifications and assumptions were made. These were:

- The recuperator (HX-1) in the CO_2 power cycle was omitted from the simulation. This was done to simplify the simulation process. A recuperator would yield the extra requirement that the low pressure gas out of the expander had to be warmer than the high pressure liquid leaving the pump, or else the recuperator would work against its own benefit.
- CO_2 at the exit of HX-3 was set to be saturated liquid.
- CO_2 at the exit of HX-8 was set to be liquid at a temperature 10 °C below saturation temperature at exit pressure.
- Air mass flow was set to 0,136 kg/s.
- All pump isentropic efficiencies were given the value of 0,70, and turbine/expander isentropic efficiency was set equal 0,80.
- Condensation pressure in CO_2 power cycle was set to 60 bar. CO_2 condensates at a temperature of 21 °C at this pressure.
- Pressure of CO_2 at compressor entrance in heat pump circuit (evaporation pressure) was set to 35 bar, which means an evaporation temperature of 0 °C.
- The concentration of ethylene glycol in water was set to 23,5 % which corresponds to a freezing point of -10 °C.
- Ethylene glycol was set to have a cold temperature of 5 °C into HX-7 and a hot temperature of 15 °C out of HX-7.
- The heat exchangers between air and CO_2 in both the CO_2 power cycle (HX-2) and heat pump circuit (HX-4) were defined with a minimum internal temperature approach of 10 °C.

There were also some limitations due to specifications of the different components which were put into attention in the simulation:

- Maximum pressure of the expander in the CO_2 power cycle was set to 130 bar.
- Maximum pressure in the CO_2 heat pump was set to 130 bar.

The most important results from the simulation are given in table 1 below. For a more detailed review and discussion of the simulation and its results, see [27].

Table 1: Summary of simulation results for prototype rig

Key Measure		Hot air temperature		
		80 °C	120 °C	160 °C
CO2 Power Cycle				
Temperature into expander	[°C]	70,0	109,7	150,0
High pressure	[bar]	100	130	130
Mass flow	[kg/hr]	108,00	168,48	201,60
Net work	[kW]	0,225	0,687	1,230
Heat Pump				
Temperature into HX-4	[°C]	125,1	144,8	149,1
Evaporation temperature	[°C]	-0,1	-0,1	-0,1
High pressure	[bar]	104	125	130
Mass flow	[kg/hr]	122,47	221,76	323,64
COP	[-]	4,922	4,179	2,990
Ethylene Glycol				
Hot temperature	[°C]	15,0	15,0	15,0
Cold temperature	[°C]	5,0	5,0	5,0
Mass flow through HX-3	[kg/hr]	516,96	943,92	1418,76
Mass flow through HX-8	[kg/hr]	98,64	154,08	184,32
Air circuit				
Temperature into HX-2	[°C]	80,0	120,0	160,0
Temperature out of HX-2	[°C]	32,3	31,5	29,5
Duty HX-2	[kW]	6,500	12,100	17,900

3.3.2 Uncertainty analysis of prototype

When performing tests with the prototype rig there are certain key numbers which are interesting to present as a result and base for discussion and presentation. For this kind of power cycle such key numbers can be net work produced by the power cycle, heat exchanger duties and various efficiencies. These are not numbers which can be read directly out of some kind of meter, but instead they are calculations based on measurements of temperatures, pressures, rotational speeds and torques to mention a few.

As all measurements have some uncertainty to its value this has a consequence for the calculations of those key numbers; the uncertainties of the measurements transfers into uncertainties of the key numbers. The core of the uncertainty analysis is to quantify these uncertainties.

A lot of work can be saved by doing a proper uncertainty analysis in advance. By acquiring knowledge on the uncertainty of the results from conducting experiments, one might get away with less post-experimental fault localization. Uncertainty analysis can also be used to decide the required degree of accuracy of the measuring equipment.

In the early phase of the project an uncertainty analysis was performed as part of the preparation of the prototype rig. The simulation data produced, based on the three different cases, was used in the calculation of the uncertainty.

Some basic theory on uncertainty analysis [28, 29]:

Those key numbers mentioned in the introduction are in uncertainty analysis theory called data reduction equations. They can be written on the form

Equation 9

$$r = r(\mathrm{X}_1, \mathrm{X}_2, \ldots, \mathrm{X}_\mathrm{i})$$

where $X_1, X_2, \ldots, X_i$ are variables in the data reduction equation, for instance temperatures and pressures. The total uncertainty related to this data reduction equation is denominated by U_r, consists of the systematic and random uncertainties, and is calculated as

Equation 10

$$U_r^{\,2} = B_r^{\,2} + P_r^{\,2}$$

The systematic uncertainty of the result, B_r, is calculated as follows:

Equation 11

$$B_r = \left\{ \sum_{i=1}^{N} \left(\frac{\partial r}{\partial X_i} B_i \right)^2 \right\}^{1/2}$$

B_i is the systematic uncertainty of parameter i.

The random uncertainty of the result, P_r, is calculated in the same manner:

Equation 12

$$P_r = \left\{ \sum_{i=1}^{N} \left(\frac{\partial r}{\partial X_i} P_i \right)^2 \right\}^{1/2}$$

P_i is the random uncertainty of parameter i.

In the planning phase of the experiment, normally a generalized uncertainty analysis is performed. At this stage the measured variables are given an uncertainty, ignoring the categorizing into systematic and random uncertainties. The total uncertainty would then be described as:

Equation 13

$$U_r = \left\{ \sum_{i=1}^{N} \left(\frac{\partial r}{\partial X_i} U_i \right)^2 \right\}^{1/2}$$

The uncertainty analysis was done with all three sets of data (i.e. warm air temperature of 80 °C, 120 °C and 160 °C) to see if there were major differences in the uncertainty for different conditions. In addition to the data from the simulations, some values for the uncertainty of the different variables had to be decided. These are the U_i-s of equation 12.

- For temperatures ΔT_i was set to 0,5 K.
- For pressure measurements ΔP_i was set to 0,01 % of pressure at point *i.*
- For mass flows Δm_i was set to 0,1 % of mass flow.
- ΔV_i for air volume flow was set to 0,1 % of value of volume flow.

From the results of the uncertainty calculations three areas were identified where the uncertainty proved to be too large. One problem area was the calculation of the individual heat duties of the HX-3 and HX-8 heat exchangers on the CO_2 side (the condensers of the power cycle), whose values proved to have too large uncertainties. The solution to this problem was to calculate the total heat duty of HX-3 and HX-8 together, which reduced the uncertainty to acceptable values.

The second problem area proved to be calculation of heat duties for the heat exchangers involving ethylene glycol (HX-3, HX-7 and HX-8). The decisive parameters in these data reduction equations were the temperatures and their uncertainties. An analysis of the relative heat exchanger uncertainty as a function of the temperature uncertainties was conducted. The results are shown in figure 20 below. The relative uncertainty expresses the ratio of the uncertainty to the calculated value.

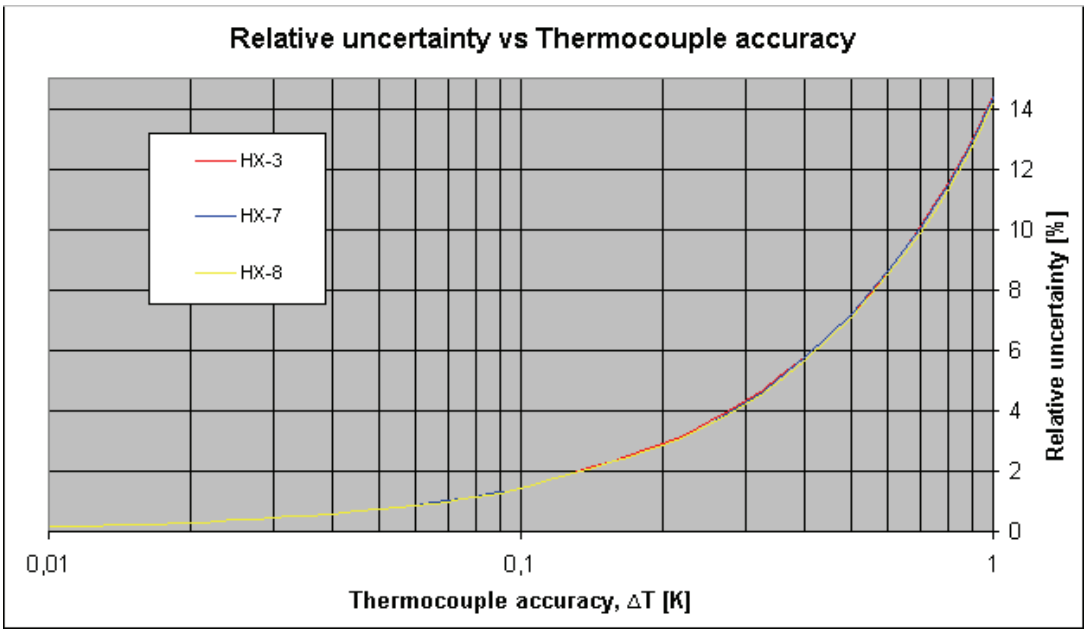

Figure 20: This chart shows the relative uncertainty of the heat duties of HX-3, HX-7 and HX-8, for the ethylene glycol side, as a result of variation of the temperature uncertainty.

The last problem was the uncertainties for the net work and thermal efficiency of the power cycle. As can be told from the table below, the uncertainties found for the net work and especially thermal efficiency are unacceptable high.

Table 2: Calculated values, uncertainties and relative uncertainties for net work, thermal efficiency and coefficient of performance for warm air temperature of 80 °C.

	W_net [W]	η_th	COP
Calculated value	224,75	0,034	3,469
Uncertainty	73,76	0,080	0,044
Relative uncertainty [%]	32,82	231,89	1,25

The resulting relative uncertainty from varying the temperature uncertainties is shown in figure 21. The temperatures are parameters in the data reduction equations of net work and thermal efficiency.

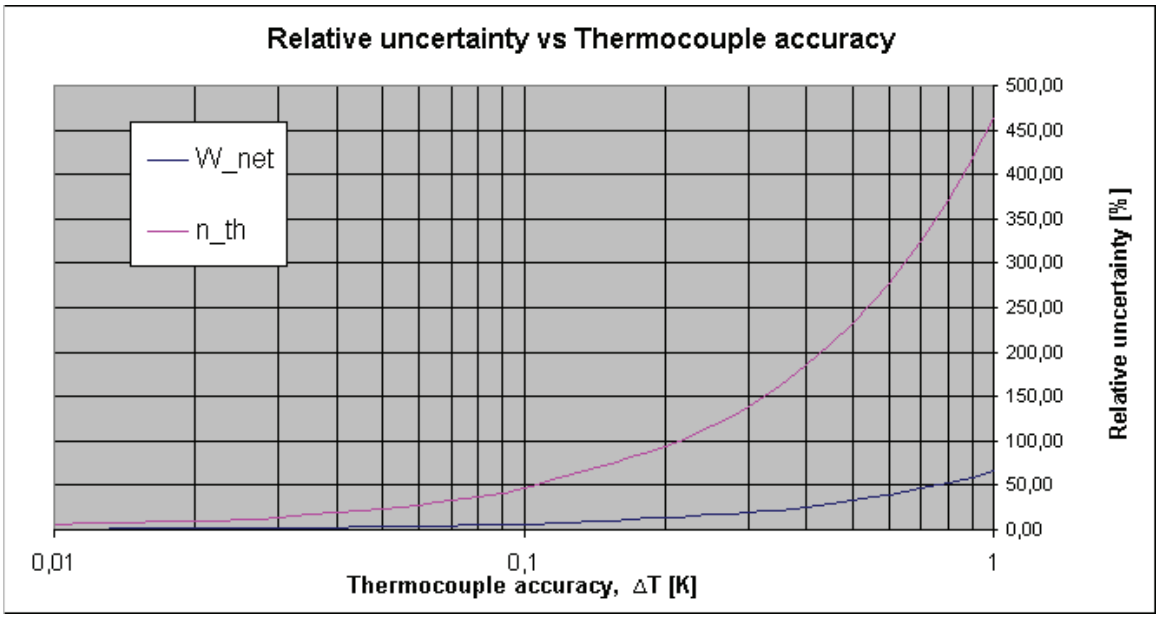

Figure 21: This chart shows the relative uncertainty of the net work and thermal efficiency as a result of variation of the temperature uncertainty on temperatures on both sides of the expander and the pump in the CO_2 power cycle.

It is believed that a way to evade this problem is to calculate the expander and pump work as a function of rotational speed and the torque. By incorporating this into the uncertainty calculation of net work and thermal efficiency, the relative uncertainty as a result of the uncertainty of the rotational speed and the torque is shown in figure 22. The temperature and pressure uncertainties are the same as for the initial calculations.

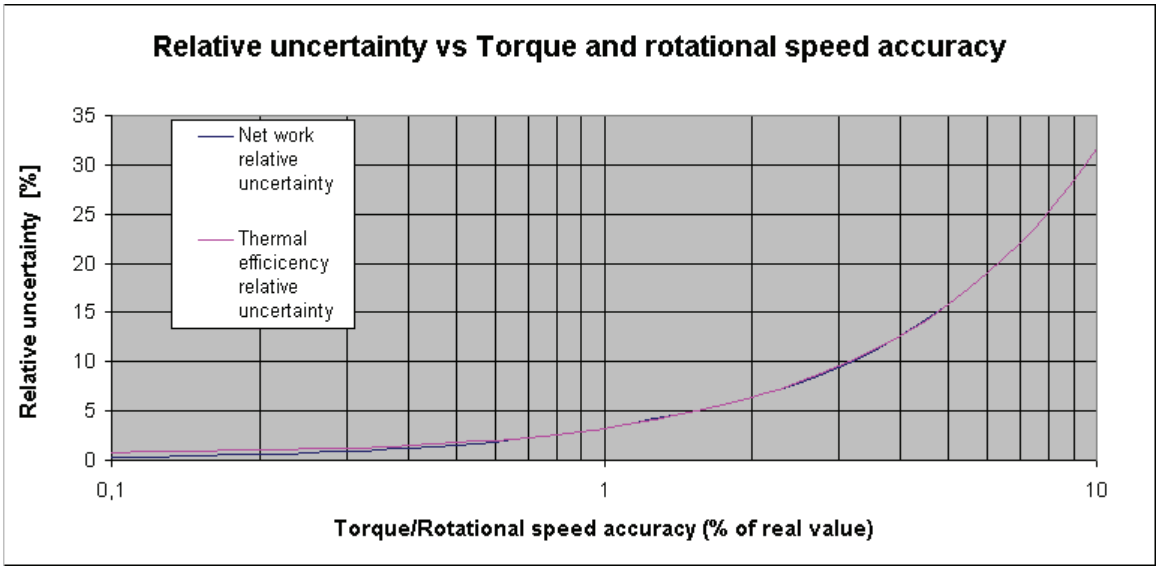

Figure 22: The calculations of relative uncertainty of net work and thermal efficiency as a fuction of the torque and rotational speed accuracy (assuming these are uniform) are shown in this chart.

As can be seen from figure 22 both the net work and thermal efficiency relative uncertainty are drastically reduced compared to the values in table 2. The accuracy of the

torque and the rotational speed can be assumed to be around 1-2 % of the measured value. From figure 22 it can be seen that this reduces the relative uncertainties of the net work and thermal efficiency to about 6-7 %. Comparing the two ways to calculate the net work and thermal efficiency, it is logical to assume the solution to use the rotational speed and torque as parameters in the calculation is the most accurate.

3.4 Prototype preparation and testing

During the time period in which the ROMA prototype rig was being built and put together, the individual cycles (air loop, ethylene glycol circuit and power cycle) and their components were prepared and tested. As a consequence of the completion of the ROMA prototype rig being delayed, this Master thesis changed its focus from experimental investigation of the complete prototype power production system to experimental investigation of its individual components. This chapter presents which specific components that were investigated, how they were investigated and results and discussions from these investigations. In addition, consequences of the investigation findings are taken under consideration.

3.4.1 Prototype testing - Warm air loop

The air loop is an important part of the prototype power production system as this loop is to simulate the heat source of the power producing cycle, i.e. the off gas from the aluminum production cells. In the process of assembling and installing this air loop some measurement instrumentation was also installed; this was done in order to record temperatures, pressures and mass flow. After installation, these instruments were checked for their functionality. In addition the assembled air loop, complete with heat exchangers (and heater) as well as pipes and fittings, were checked for irregularities which would lead to a non-optimal running of the prototype power production system.

3.4.1.1 Preliminary testing

Before the air loop was assembled, different sections of the loop were tested for leakage points. The idea was to identify these possible spots and evaluate if these would have a considerable influence on the mass flow and the velocity profile of the air loop.

The test procedure was as following. The air loop section which was to be tested was completely closed. A wooden plate with two small holes was mounted to the flanges of the heat exchanger. Connected to one of the holes was a small tube which was filled with water, also called a simple manometer. This was being used to measure the pressure difference between the atmospheric pressure and the pressure inside the sealed air loop section.

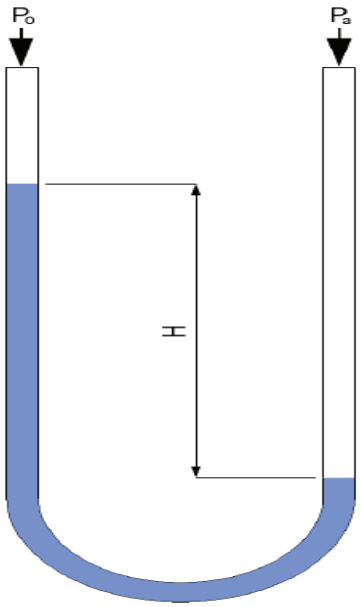

Figure 23: Simple manometer used to measure a pressure difference [30]

The other hole was then used to fill air with a compressor unit. By reading the height of the water column and thereby calculating the pressure difference between the inside and outside of the sealed section, the velocity of air could be calculated from the simple equation:

Equation 14

$$\Delta P = \frac{1}{2}\rho v^2$$

Equation 14 is derived from the steady flow energy equation [31]:

Equation 15

$$\left(\frac{p}{\gamma}+\frac{V^2}{2g}+z\right)_{in} = \left(\frac{p}{\gamma}+\frac{V^2}{2g}+z\right)_{out} + h_{friction} - h_{pump} + h_{turbine}$$

Rearranging the symbols in equation 14 gives:

Equation 16

$$v = \sqrt{\frac{2\Delta P}{\rho}}$$

The air velocity can be expressed as a function of the air density, mass flow rate and "leakage area":

Equation 17

$$v = \frac{\dot{m}}{\rho S_l}$$

Inserting the expression for air velocity in equation 17 into equation 14 and rearranging gives the following expression for the leakage area:

Equation 18

$$S_l = \sqrt{\frac{\dot{m}^2}{2\rho\Delta P}}$$

The leakage testing involved two sections of the air loop, one section consisting of the electrical heater and one section consisting of an air-to- CO_2 heat exchanger (HX-2) coupled to two 90 degrees bends with a tube in between.

The results from the testing of the heater showed a neglect able leakage area of 12,57 mm^2 . A summary of measurements and calculations are shown below in table 3.

Table 3: Summary of the results from leakage tests on heater section.

Air nozzle, cross section area:	12,60	[mm2]
Air density (20 C):	1,1886	[m3/kg]
Pressure difference from manometer:	300	[Pa]
Air velocity:	22,47	[m/s]
Mass flow air in/out:	1,21	[kg/hr]
Total leakage area:	12,57	[mm2]

From the tests it was concluded that the heater section did not show any substantial leakage which had to be investigated any further. For the section consisting of the air-to-CO_2 heat exchanger several leakage points were found by visual inspection. The most severe examples were found at the flanges of the heat exchanger as well as in the connection between the fitting and the upper 90 degrees bend. Needless to say, all the identified openings had to be sealed with joint-filler when the air loop was put together.

3.4.1.2 Installation of thermocouples

In the first stage of the installation, thermocouples were installed in front of and after the heat exchanger between the air loop and the power loop (HX-2). At the other heat exchanger (HX-4), installation of thermocouples was omitted at that time due to shortness of thermocouple material.

The thermocouples used were made out of material which could stand temperatures well above 100 ° C, which was necessary seen as the temperatures of the air coming out of the heater was planned to operate at those temperatures.

It was decided to use a set up of four thermo elements in front of HX-2 and eight thermo elements after the same heat exchanger. These elements were coupled to a metal grid as shown in figure 24 below.

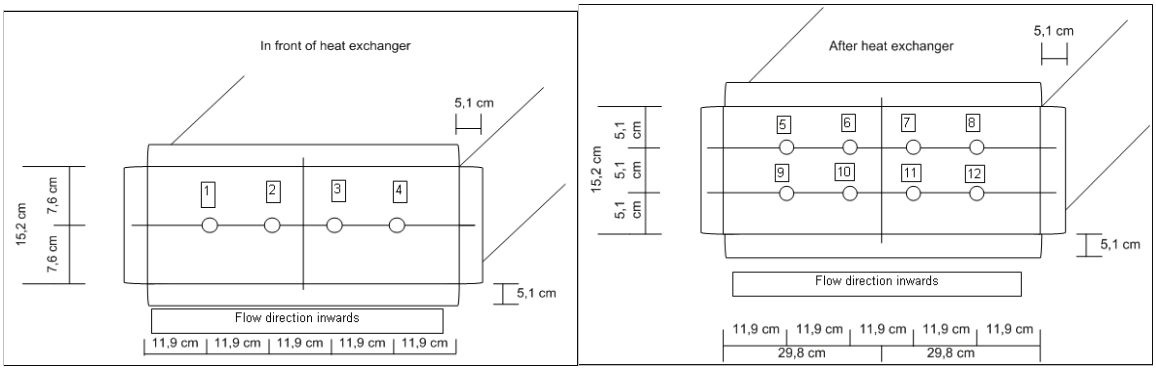

Figure 24: Sketches of the set up of thermocouples in front of and after HX-2.

The grids were made from metal pins with a diameter of 2 mm, which were spot welded at the connections. The thermocouple wires (which had been spot welded at the interconnections of the two thermocouple metals) were then fixated to the grid with heat-shrinkable tubing. As an extra measure to protect the thermocouples from the radiation heat from the heater elements, a small radiation shield was mounted on each of the four thermo elements in front of HX-2. These shields were made from thin aluminum foil. This was done because the radiation from the heater elements could induce an error to the measured temperature at the thermo elements. A more detailed view of the set up is shown in the picture below.

Figure 25: Picture of thermocouple installation at heat exchanger inlet, complete with radiation heat shielding.

The metal grids with the attached thermocouple wires were inserted into the channels of the heat exchanger, through small holes drilled into the channel walls. A larger hole was made as an entry for the thermocouple wires. These wires were eventually connected to a data logger.

3.4.1.3 Air loop – Mass flow measurements

When all temperature instrumentation was installed in the air loop, the next logic step was to run tests. The testing objectives were to verify that the thermocouples functioned well; then to test the air fan and operation of the heater. The temperature distribution out of the heater and the mass flow provided by the air fan were of the most important features investigated as these two are key measures in the regulation of the warm air as a heat source in the final prototype rig.

Initial tests were done at two different air fan speeds, at 50 Hz (which was the maximum rotational speed) and 25 Hz. The heater had a regulator connected to a single thermocouple element at the heater outlet, and with the signals received from this thermocouple the regulator triggered a voltage input to the heater elements based on a set point temperature given by the user.

The tests were done with the air loop both open and closed, meaning that in the first case the fan sucked the air from atmospheric conditions while latter case helped decrease the strain on the fan as it could “work against” a lower than atmospheric pressure.

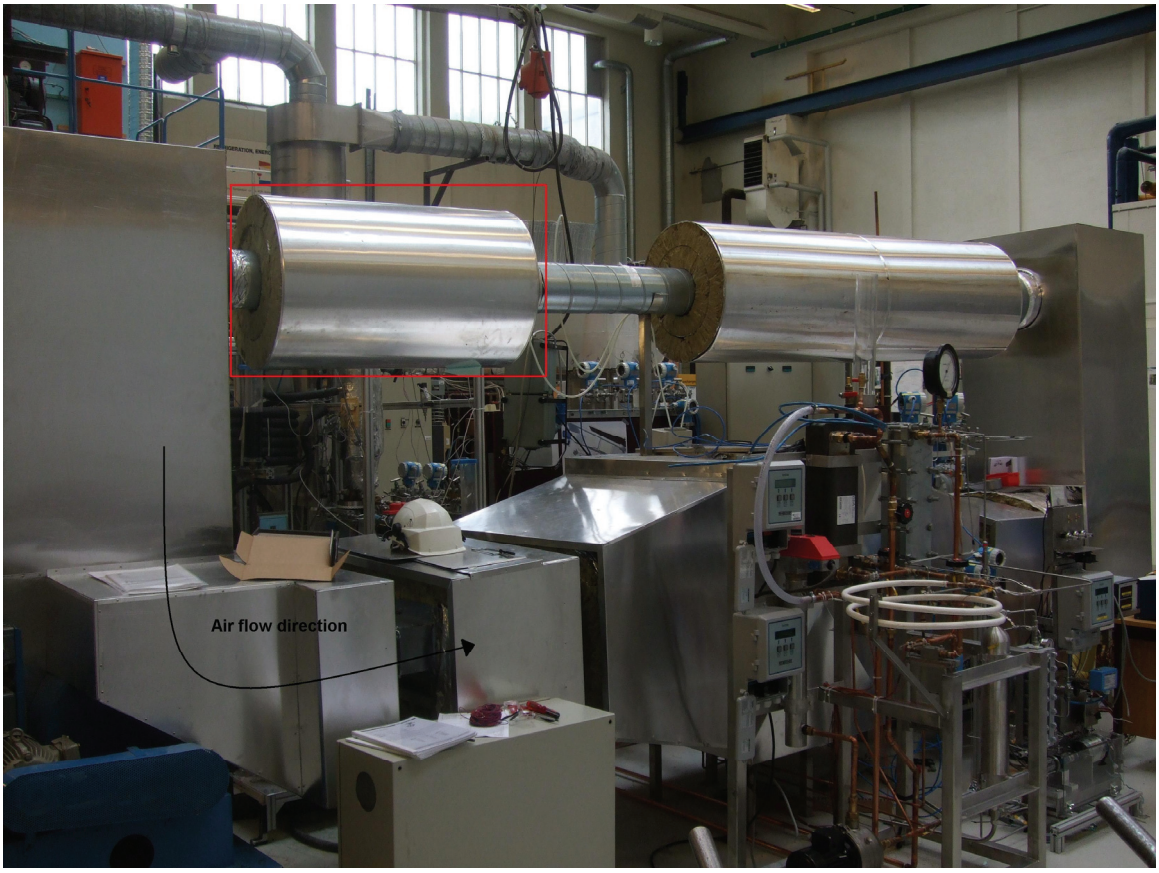

Figure 26: This picture shows the ROMA prototype rig, without the heat pump. The air loop is the large loop in the background. The red square highlights the section of the air loop which was removed when the air loop was run as an open loop.

To measure the mass flow of air in the air loop, an orifice plate is installed in the return pipe leading the air from HX-2 back to the air fan. On each side of this orifice plate are pressure tappings for measurement of the differential pressure across the plate. This differential pressure is, along with the dimensions of the orifice plate, used to calculate the mass flow of air. The following section describes the theory behind these calculations.

Measurement of fluid flow by use of orifice plates

The theory in the following section is taken from [32] and [33] unless otherwise stated.

Orifice plate set up

The design and set up of the orifice plate (see figure 27) and pressure tappings are subject to an ISO standard and are therefore carefully conducted. Guidance is given on subjects as thickness of orifice plate, distance from orifice plate for pressure tappings both

upstream and downstream as well as other design parameters in [33]. This report will not go further into these standards but rather refer to the mentioned reference.

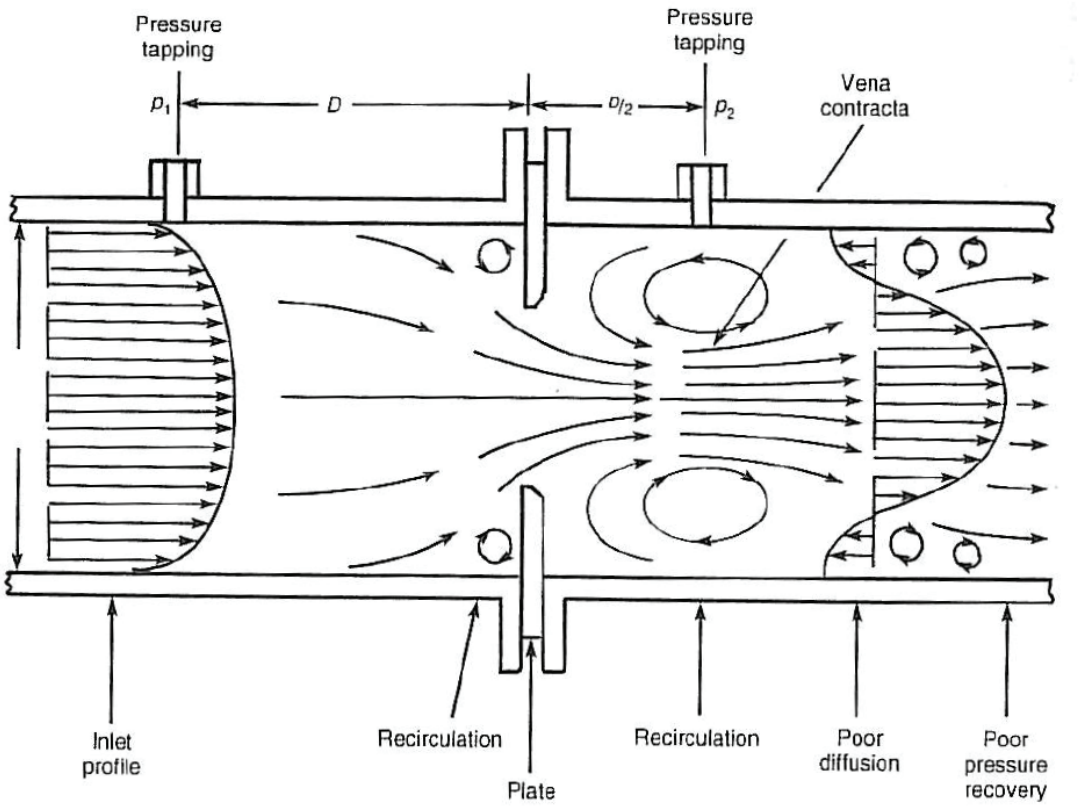

Figure 27: Geometry and flow patterns in the orifice plate set up. [34]

Theory

The target of this deduction is to show how the measured pressure differential across the orifice plate and the dimensions of the set up of the measurement system is used to calculate the mass flow. This section of theory will only concern equations and conditions which were needed to compute the mass flow in this test.

The installation of an orifice plate in a pipeline where a fluid is flowing causes a static pressure difference between the upstream and downstream sides of the orifice plate. This pressure difference can be used to calculate the mass flow rate, q_m:

Equation 19

$$q_m = \frac{C}{\sqrt{1-\beta^4}} \varepsilon \frac{\pi}{4} d^2 \sqrt{2\Delta p \rho_1}$$

From this equation it can be seen that several parameters need to be calculated.

The discharge coefficient, *C*, relates to the dimensions of the orifice set up as well as the Reynolds number for the fluid flow, Re_D. It is given by the Reader-Harris/Gallagher (1998) equation:

Equation 20

$$C = 0{,}5961 + 0{,}0261\beta^2 - 0{,}216\beta^8 + 0{,}000521\left(\frac{10^6\beta}{\mathrm{Re}_D}\right) + (0{,}0188 + 0{,}0063A)\beta^{3{,}5}\left(\frac{10^6}{\mathrm{Re}_D}\right)^{0{,}3}$$
$$+ (0{,}043 + 0{,}080e^{-10L_1} - 0{,}123e^{-7L_1})(1 - 0{,}11A)\frac{\beta^4}{1-\beta^4} - 0{,}031(M_2' - 0{,}8M_2'^{1{,}1})\beta^{1{,}3}$$

The parameters used in equation 20 are:

$\beta = d / D$ the diameter ratio.

$\mathrm{Re}_D = \frac{\rho V D}{\mu}$ Reynolds number

$L_1 = l_1 / D$ the quotient of the distance of the upstream tapping from the upstream face of the orifice and the pipe diameter

$L_2' = l_2' / D$ the quotient of the distance of the downstream tapping from the downstream face of the orifice and the pipe diameter

$$M_2' = \frac{2L_2'}{1-\beta}$$

$$A = \left(\frac{1900\beta}{\mathrm{Re}_D}\right)^{0{,}8}$$

As the principle used in this orifice installation is the D and D/2 tappings, the L_1 and L_2' are given the values of 1 and 0,5 respectively.

The expansibility factor, ε, which can also be found in the equation for calculation of the mass flow rate (equation 19), is calculated as follows:

Equation 21

$$\varepsilon = 1 - (0{,}351 + 0{,}256\beta^4 + 0{,}93\beta^8)\left[1 - \left(\frac{p_2}{p_1}\right)^{1/\kappa}\right]$$

Calculation of the mass flow rate is an iterative process since the discharge coefficient, C, is a function of the Reynolds number, Re_D, which in turn is a function of the mass flow rate through the pipeline.

Results from mass flow measurements

Several tests were run to calculate the mass flow rate in the air loop. Both air fan rotational speed and heater temperature set point were varied, and tests were performed with both open and closed air loop.

Table 4: Results from calculations of mass flow rate based on differential pressure measurements over orifice arrangement in air loop.

Parameter	Dimensions	Value					
Air loop conditions:							
Air fan speed, frequency	*Hz*	25	25	50	50	25	50
Temperature air into orifice	*°C*	30,0	51,0	30,0	57,0	34,0	34,0
Open or closed air loop	-	Open	Open	Open	Open	Closed	Closed
Measured values:							
Pressure upstream of orifice, P1	*Pa*	101421,2	101458,0	101790,0	101824,0	101288,0	101232,0
Pressure downstream of orifice, P2	*Pa*	101325,0	101325,0	101325,0	101325,0	101026,0	100305,0
Differential pressure, ΔP	*Pa*	96,2	133,0	465,0	520,0	262,0	927,0
Calculations:							
Reynolds number, Re_D	-	20840	22653	45548	43556	34087	63803
Mass flow	*kg/s*	0,061	0,070	0,133	0,136	0,100	0,187
Mean velocity orifice outlet	*m/s*	8,10	9,77	17,69	19,40	13,24	24,79

Table 4 shows the calculation results based on the differential pressures measured at various conditions in the air loop. It can be seen that, at maximum air fan speed, the mass flow rate is increased by about 40 % (from 0,133 kg/s to 0,187 kg/s) when the air loop is closed compared to tests with an open air loop. When compared to the target mass flow rate of 0,136 kg/s the tests show that when run in a closed air loop the air fan can provide a large enough air flow rate.

3.4.1.4 Air loop - Testing of temperature profile

As mentioned earlier the tests were performed at two different air fan rotational speeds; 25 Hz and 50 Hz. Several tests were conducted to look at both the response from changing the air fan speed at a constant heater temperature set point, and changing the heater temperature set point at constant air fan speed. The graphs in figure 28 show the temperature response from changing the air fan speed from 50 Hz to 25 Hz when the heater temperature set point was at 80 ° C. The thermo element used to regulate the heater against the set point temperature was installed higher in the air channel than the thermo elements used for temperature logging. The air at this element was warmer than the air in the vertical middle of the channel, and because of this the measured temperatures were never as high as the temperature set point.

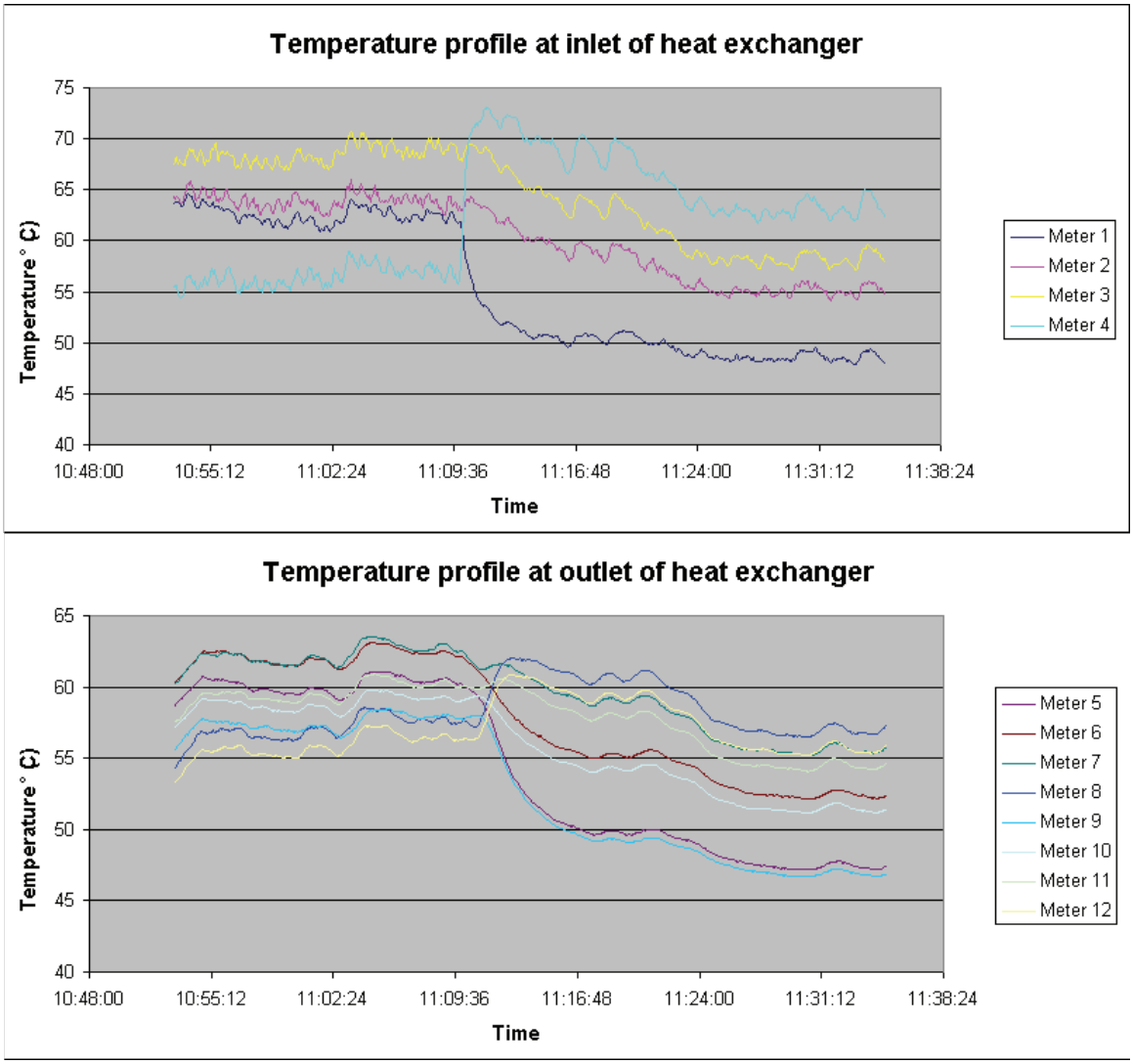

Figure 28: Testing of open air loop; temperature distribution in front of (above) and after (below) heat exchanger. The figures show the temperature response for the air loop when air fan speed changes from 50 Hz to 25 Hz, the heater temperature set point is constant at 80 °C.

From these two figures it can be seen that there is a wider temperature distribution across the cross-section of the heat exchanger for the lower air fan rotational speed. This is most evidently seen for the four thermocouples in front of the heat exchanger. At high air velocities the air seems better mixed as the difference between the highest and the lowest temperature is around 12-13 ° C and the highest temperature is measured by the two thermocouples in the middle. When the air fan speed is halved (to 25 Hz) the temperature profile changes its characteristics and the difference between the highest and the lowest temperature increases to about 16-17 °C. The temperature profile changes so that the lowest temperature is at the left side of the channel (in the direction of flow), and the temperature increases gradually towards the right side of the channel where the highest temperature is measured.

As a confirmation of what is observed in figure 28, figure 29 shows the temperature distribution when the order of occurrence is reversed, i.e. the air fan speed goes from 25 Hz to 50 Hz at a constant heater temperature set point of 80 °C.

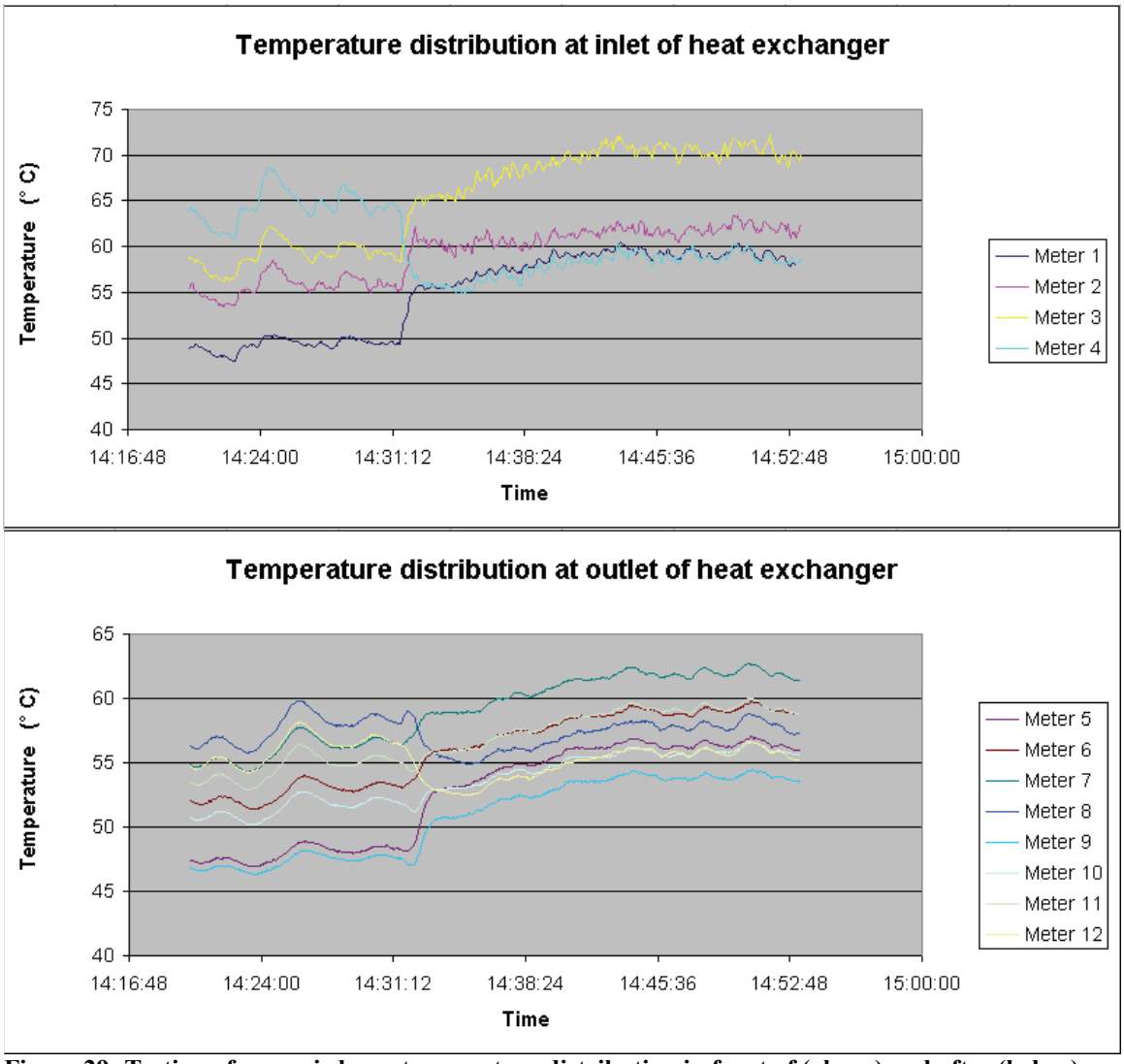

Figure 29: Testing of open air loop; temperature distribution in front of (above) and after (below) heat exchanger. The figures show the temperature response for the air loop when air fan speed changes from 25 Hz to 50 Hz, the heater temperature set point is constant at 80 °C.

Figure 29 shows exactly the same response when the air fan speed is changed, in this case from low to high frequency. The temperature distribution narrows a little when stabilized at the higher air speed.

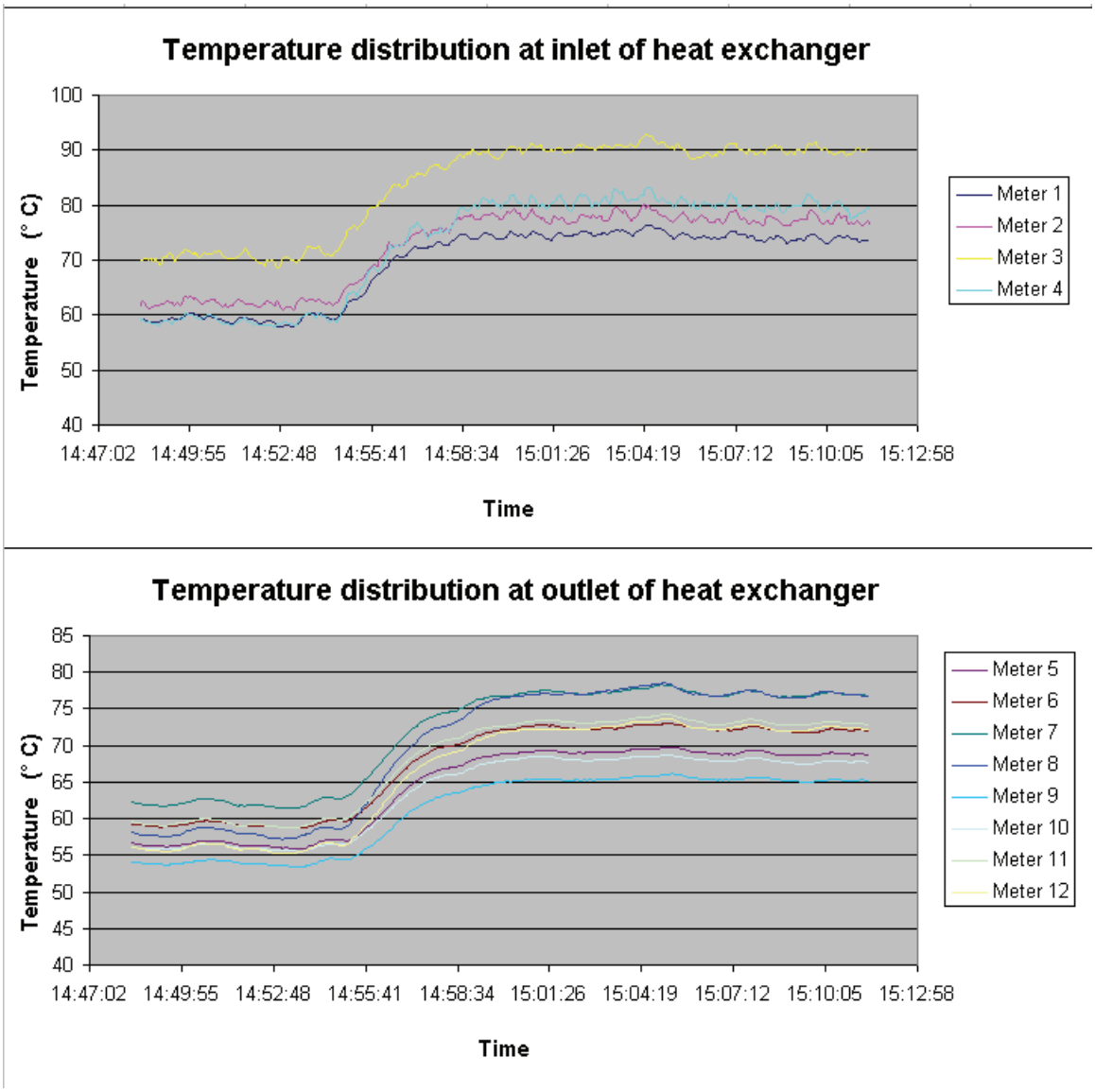

Figure 30: Testing of open air loop; temperature distribution in front of (above) and after (below) heat exchanger. The figures show the temperature response for the air loop when the heater temperature set point is changed from 80 °C to 100 °C. The air fan frequency is constant at 50 Hz.

In figure 30 the temperature response for a change in heater temperature set point from 80 °C to 100 °C is shown, with air fan frequency at a constant value of 50 Hz. The increase in heater temperature set point seems to result in a wider temperature distribution.

The next series of testing was done with a closed air loop where the upper section was installed to return the air back to the air fan inlet (see figure 26).

Measured temperatures from a test where the air fan is operated at 50 Hz, the heater temperature set point is changed from 50 °C to 80 °C, and the air loop closed is shown in figure 31. When compared to the temperature distribution for the same conditions in the

open air loop (figure 28), it is obvious that the air mixing is better for the closed loop compared to the open loop.

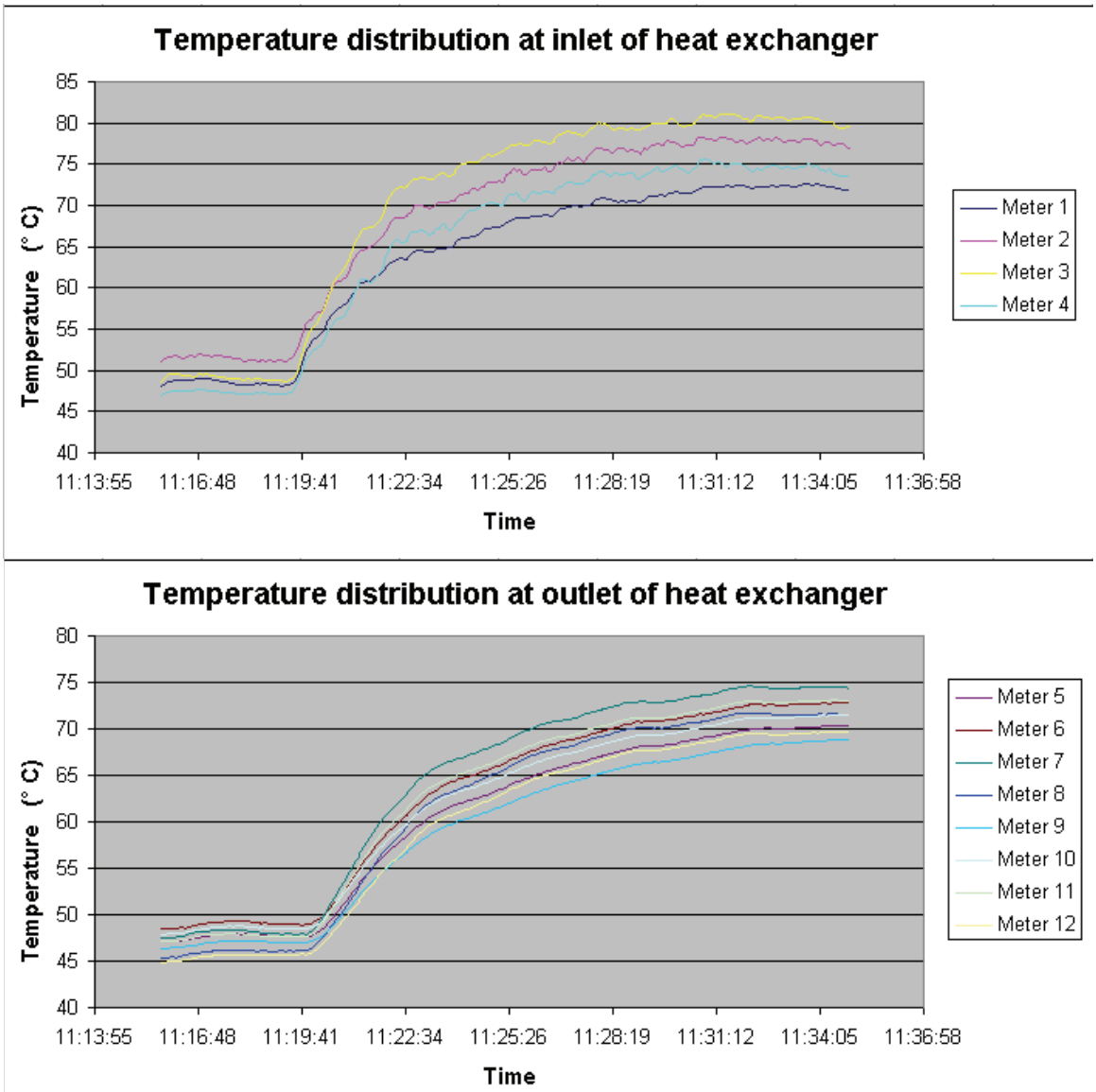

Figure 31: Testing of closed air loop; temperature distribution in front of (above) and after (below) heat exchanger. The figures show the temperature response for the air loop when the heater temperature set point is changed from 50 °C to 80 °C. The air fan frequency is constant at 50 Hz.

Overall it could be concluded that there exists some sort of imbalance in the air loop system which leads to an uneven temperature distribution of the air into the HX-2 heat exchanger. As a result further investigations had to be done in order to localize the source(s) of this imbalance.

3.4.1.5 Air loop – Investigation of heater unit

Since the testing of the air loop indicated an imbalance which led to an uneven temperature distribution in the air flow after the heater, it was decided to open up the air loop after the heater unit to do measurements of the air velocities out of the heater.

The measurements were conducted with a hand held vane probe anemometer of the type MiniAir5 made by Schiltknecht Messtechnik AG. When the probe was held perpendicular to the air stream the air velocity at that point was shown on an analog display, in meter per second. In order to get an image of the velocity profile, eight measuring points were taken at specific coordinates at the heater outlet. The measuring points are shown in figure 32.

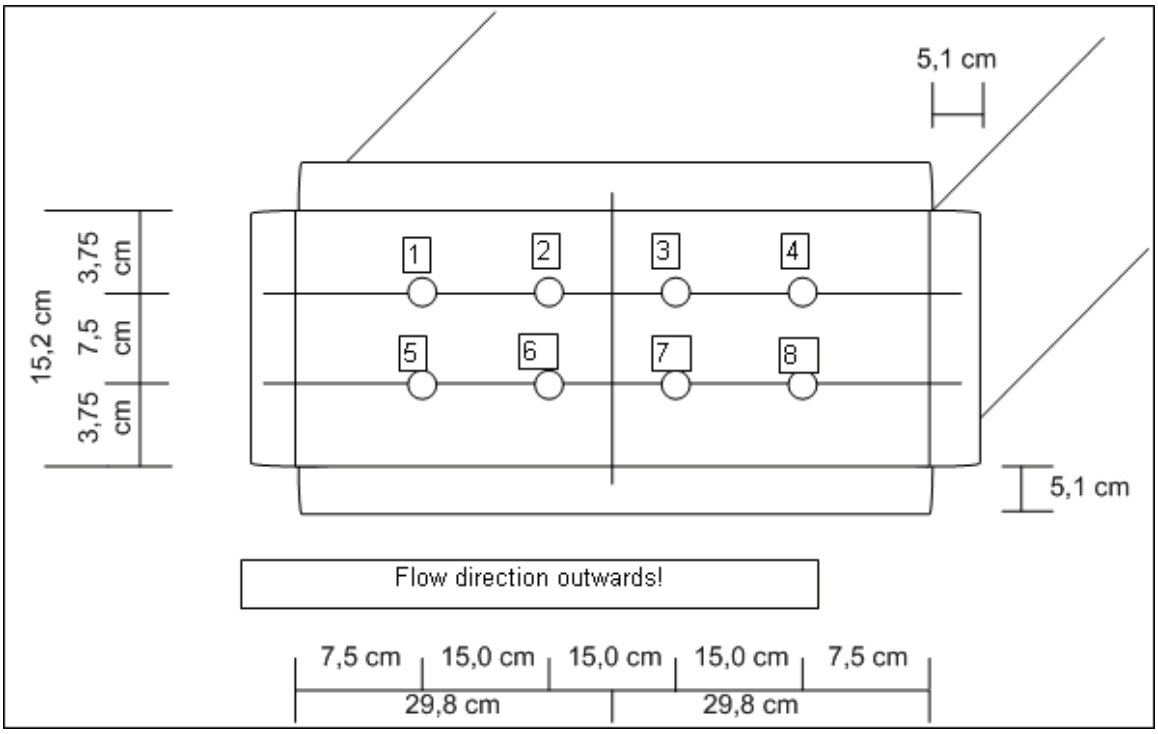

Figure 32: Measuring points for the air velocity at the outlet of both the electric heater and the individual heat exchangers.

Air velocity measurements at heater outlet

For the first round of tests, air velocity measurements were taken at the outlet of the heater unit. The measurements were taken at air fan rotational speeds of 25 Hz and 50 Hz, and the electric heater was turned off.

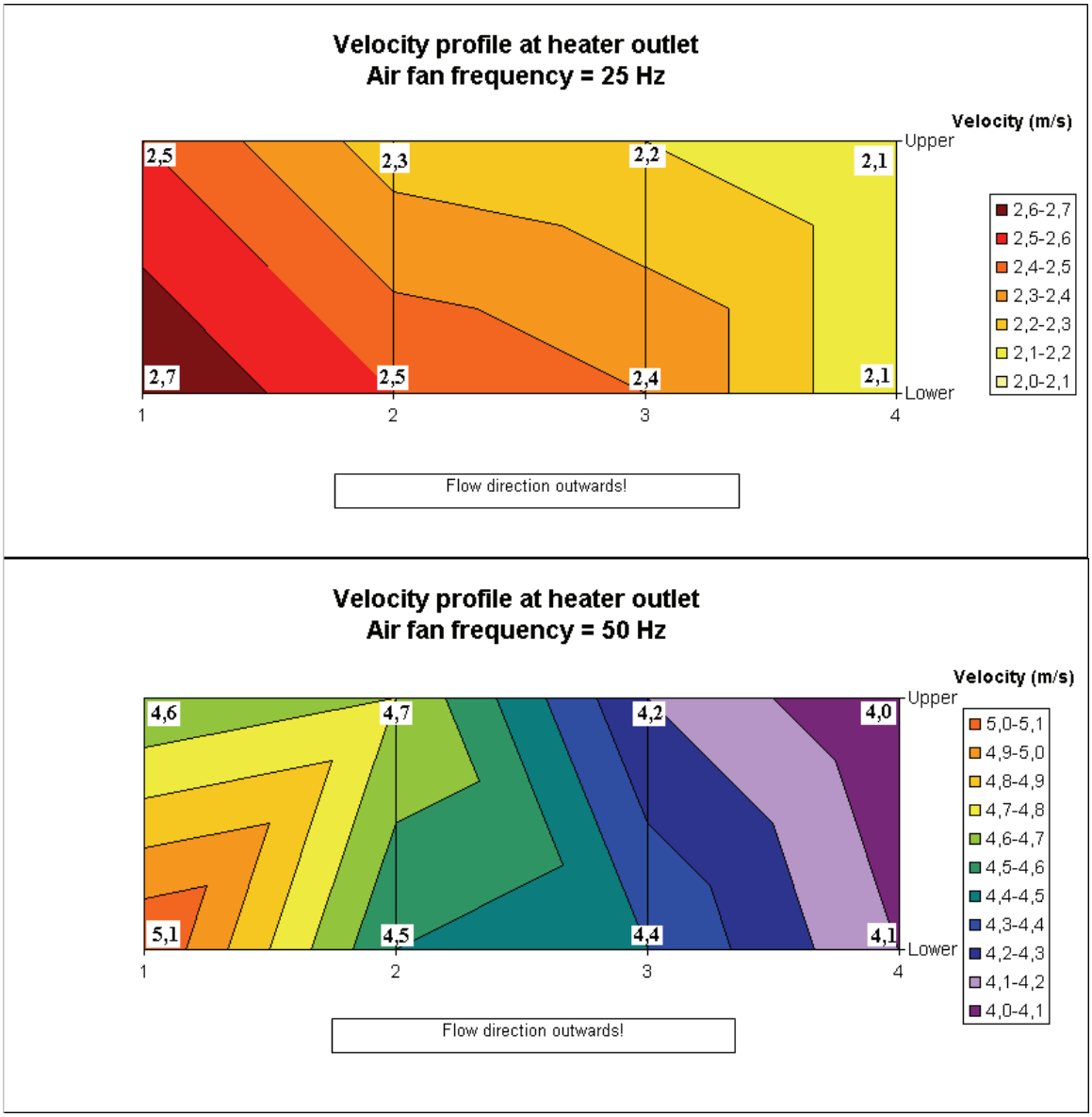

Figure 33: Constructed velocity profiles based on measured values at eight measuring points at heater outlet. The upper figure shows the profile with an air fan speed of 25 Hz, while the lower figure shows the profile with an air fan speed of 50 Hz.

Figure 33 shows **constructed** velocity profiles based on measurements done at the eight points shown in figure 32. These profiles are predominantly to give a more visual presentation of the measurements, and they do not take into account local variations of the air velocities across the cross section of the channel. The values measured at the measuring points can be found at the circumference of the profiles, at the intersection between the numbered lines (1, 2, 3 and 4) and the lines marked “Upper” and “Lower”.

In order to direct the air flow in such a manner that its direction of flow was parallel to the outlet of the electric heater, a honeycomb was placed right after the heater outlet. The honeycomb worked as a flow straightener, and velocity measurements were taken at the other side of the honeycomb. The measurements where taken at the exact same

coordinates relative to the heater outlet dimensions as the measurements taken directly at the heater outlet.

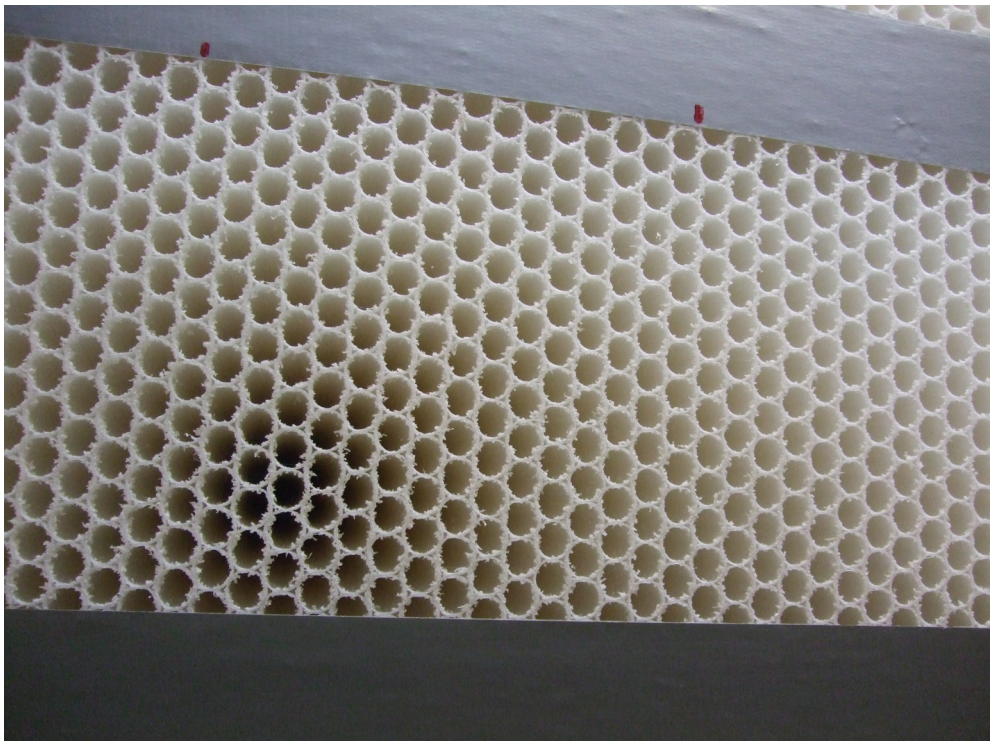

Figure 34: Measurements were done at the outlet of a honeycomb placed after the heater outlet. The dimensions of the heater outlet were marked with ducked tape in order to do measurements at the same coordinates relative to the heater outlet dimensions.

The velocity profiles based on the results from measurements at the honeycomb are shown in figure 35.

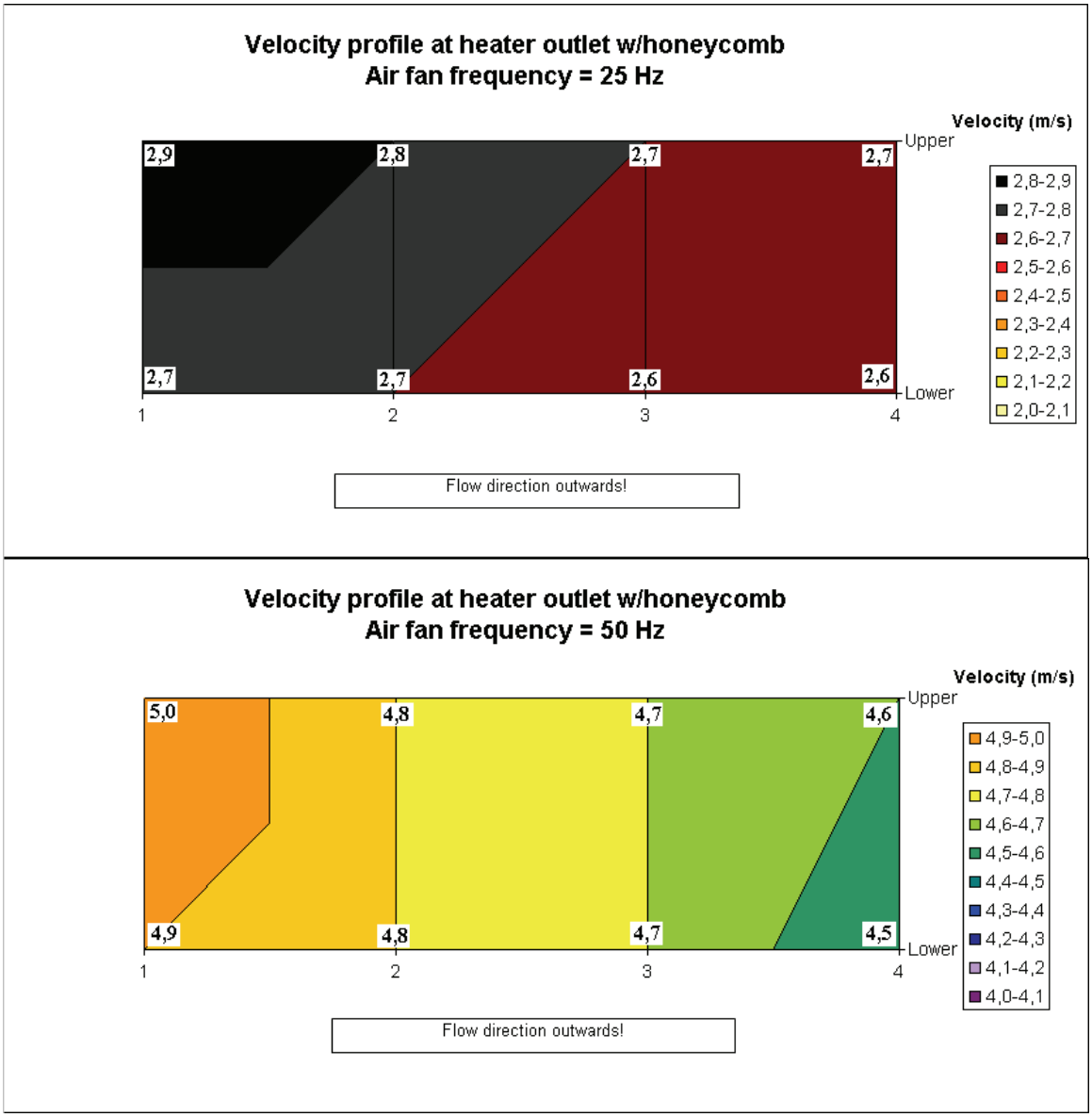

Figure 35: Constructed velocity profiles based on measured values at eight measuring points at honeycomb placed after the heater outlet. The upper figure shows the profile at an air fan speed of 25 Hz, while the lower figure shows the profile for an air fan speed of 50 Hz.

As can be seen from all the velocity profiles, it is clear that the air velocity at the right side of the heater outlet (in the flow direction) is higher than at the left side, meaning that more air flows through at that side. This is seen from measurements done both with and without the honeycomb.

Investigation of heater with thermal camera

To get further information in order to evaluate the reasons for the uneven temperature distribution out of the heater, a thermal camera was used to investigate the heating elements of the heater.

Pictures were taken with the air fan running at 50 Hz and the heater temperature set point at 30 °C and 60 °C. Pictures from two different air loop running conditions are shown in figure 36.

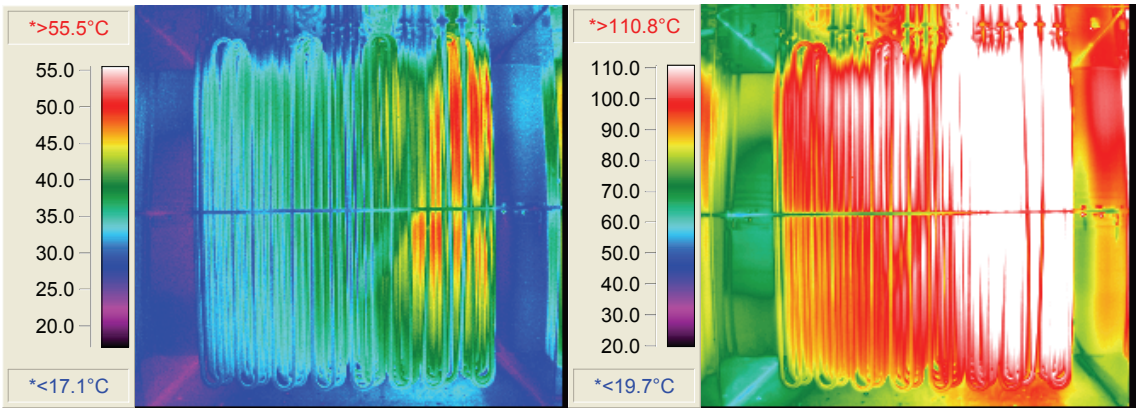

Figure 36: Photos of the heating elements of the electric heater with a thermal camera. The pictures are taken from the outlet of the heater.

The pictures are taken towards the direction of the air flow (the air flows towards the camera perspective). It can easily be seen that the surface temperature of the heater elements to the right are higher than those to the left, i.e. the heater elements to the left **in the flow direction** have the higher surface temperature.

3.4.1.6 Air loop – Investigation of heat exchangers and air fan

Investigation of HX-4 – Air velocity measurements

Since the investigation of the air flow out of the heater showed that more air flowed out of the right side of the channel, the next logical step was to investigate the unit sitting in front of the heater. This is the heat exchanger working between the air loop and the heat pump, HX-4.

The heater was therefore dispatched from the air loop, making it possible to do measurements at the outlet of HX-4. The dimensions of the heat exchanger outlet were the same as the dimensions for the heater, and the measuring points at the outlet were therefore taken at the same coordinates as for the heater outlet.

The honeycomb was also used to measure the air velocities at the outlet of HX-4, with the results from this test given in figure 37.

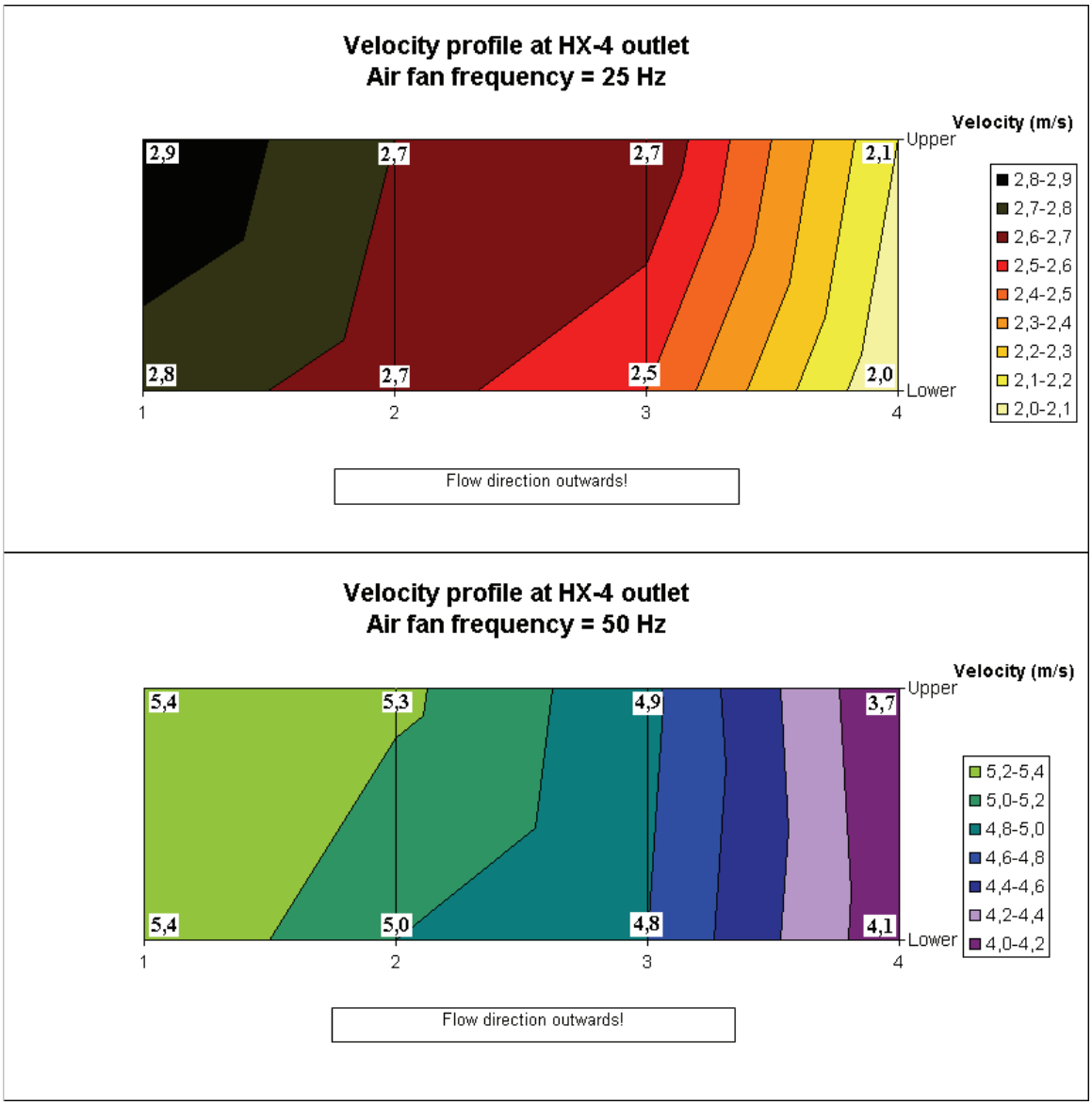

Figure 37: Constructed velocity profiles based on measured values at eight measuring points at honeycomb placed after HX-4 outlet. The upper figure shows the profile at an air fan speed of 25 Hz, while the lower figure shows the profile for an air fan speed of 50 Hz.

The profiles in figure 37 show an even larger gradient in the air velocities, going from the left side of the channel to the right, than at the heater outlet. This was a point worth noting as this indicated that the heater was not responsible for the velocity profile measured at its outlet.

In the air loop, the air fan is situated right at the inlet of HX-4 with only a short connection between the two units. Taking this into considerations it was decided to also investigate the air fan outlet to see if this could explain the air velocity gradient found further downstream of the air loop.

Investigation of air fan

A visual inspection of the channel leading the air from the air fan into HX-4 gave some more insight. The asymmetric placement of the vane wheel of the air fan relative to the channel opening would logically lead to an asymmetric velocity profile out of the air fan to heat exchanger channel (see figure 38).

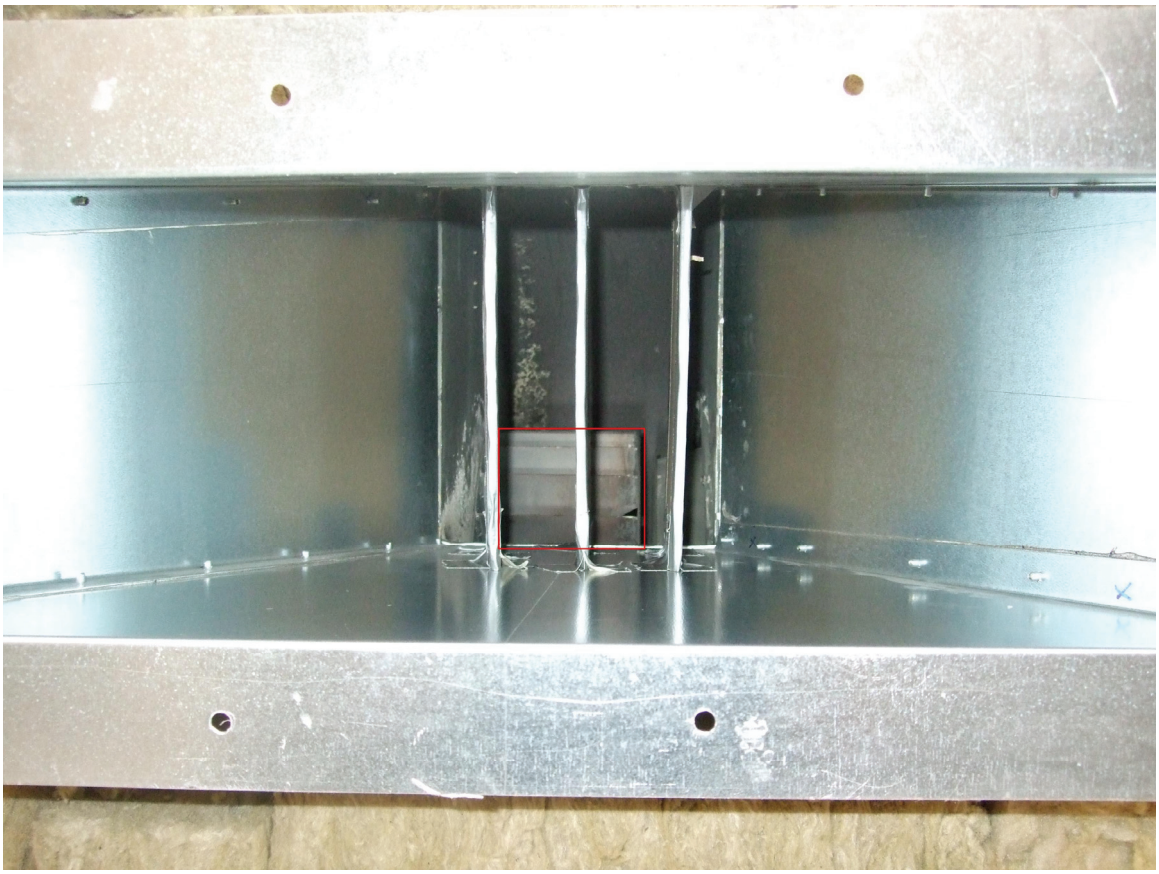

Figure 38: Picture taken of the air fan outlet. As seen in the picture, the air fan vane wheel (marked with read square) is asymmetrically placed relative to the channel opening. The fins seen in front of the vane wheel were a temporary installation in an attempt to redirect the air coming out of the air fan.

The honeycomb was placed in front of the air fan outlet and measurements were taken of the air velocity at the honeycomb, still at the same coordinates relative to the channel opening as for the other measurements. The results are given in figure 39.

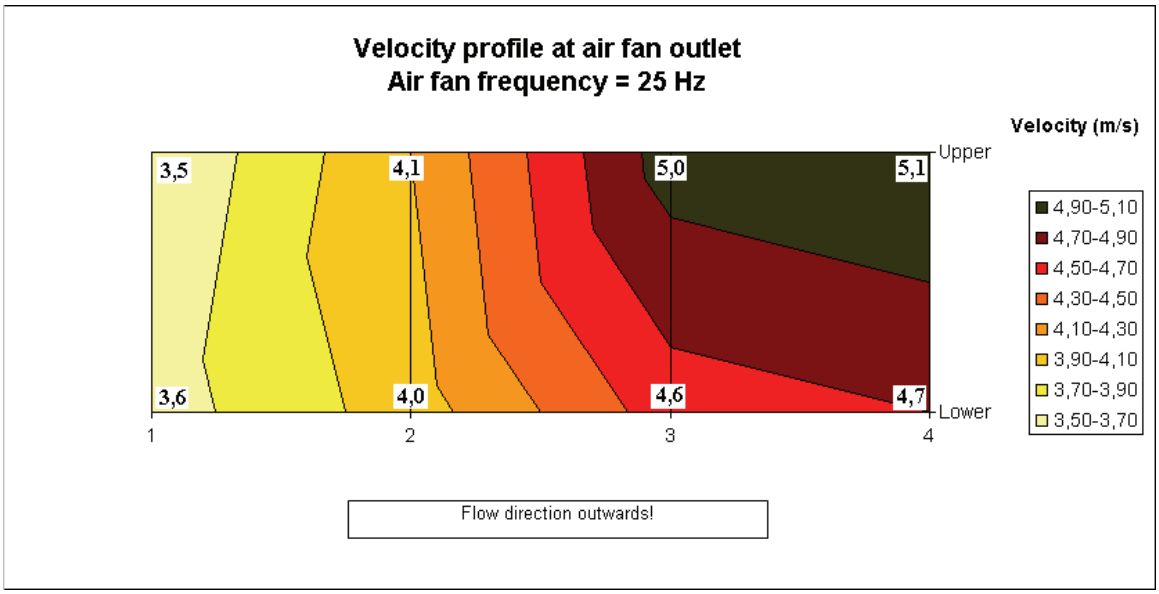

Figure 39: Constructed velocity profile based on measured values at eight measuring points at honeycomb placed after air fan outlet.

The velocity profile shown in the figure above tells that the air fan was providing more air on the right side of then channel than on the left. This was not in accordance with the results from velocity measurements done at the heater and HX-4 outlets. On the contrary this gave reason to believe that the HX-4 heat exchanger might be the deciding factor when it came to the air velocity profile at the outlet of the heater.

Further investigations of the heat exchangers

To confirm these suspicions there were performed new tests on the HX-4 heat exchanger. The heat exchanger was connected to the outlet of the air fan again, but this time it was connected the opposite way of how it normally is connected. In addition some fins made from cardboard were installed into the air fan channel (in front of HX-4) in order to align the air stream into HX-4 (see figure 38). The velocity profiles at the HX-4 outlet with HX-4 installed in normal and opposite direction are shown in figure 40.

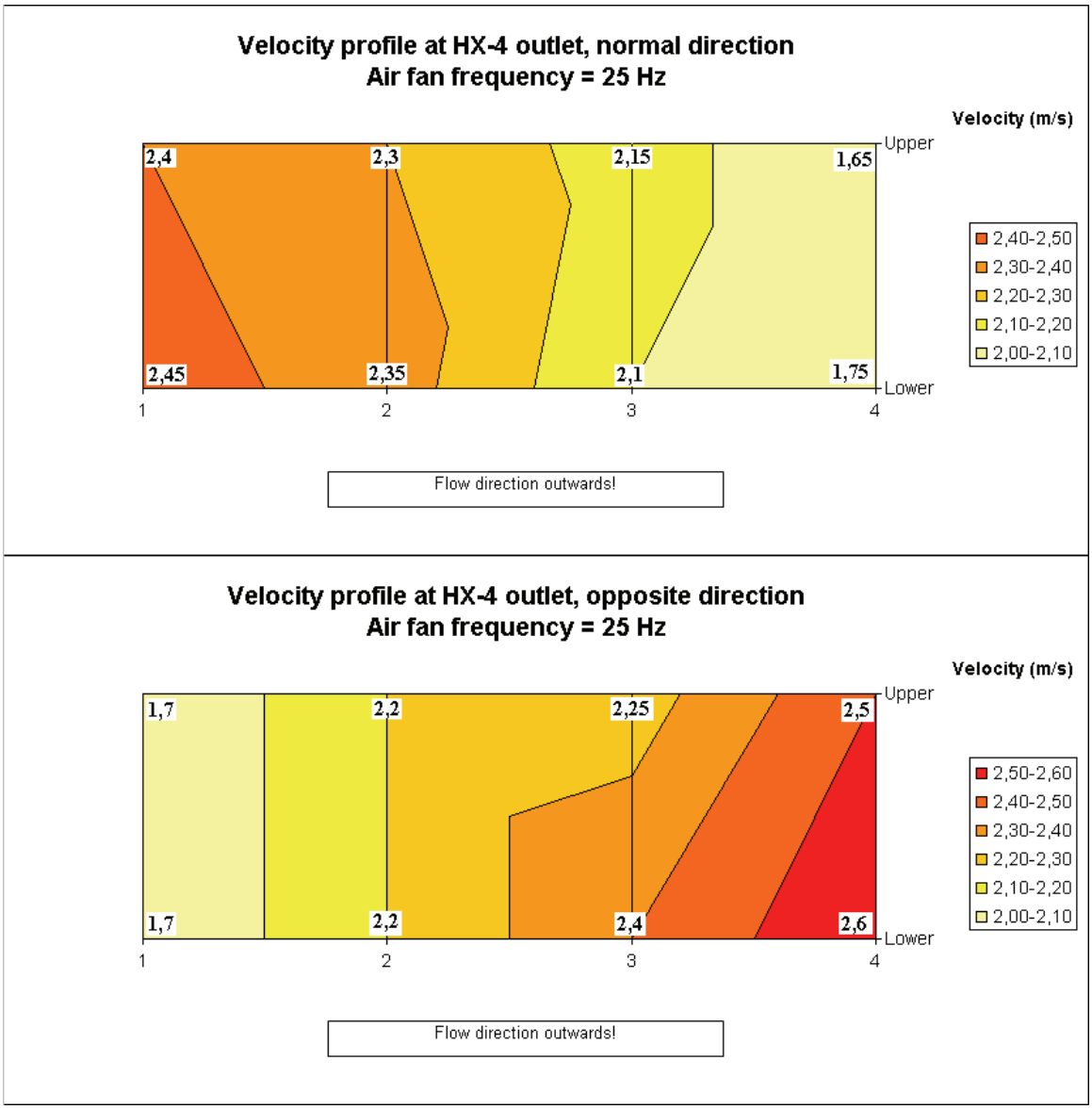

Figure 40: Constructed velocity profiles based on measured values at eight measuring points at honeycomb placed after HX-4 outlet, air fan speed set at 25 Hz. The upper figure shows the profile when HX-4 is in normal direction, while the lower figure shows the profile when HX-4 is turned in the opposite direction.

As this obviously confirmed that HX-4 was the main reason for the, the same test was performed for the HX-2 heat exchanger, with HX-2 installed right after the air fan outlet, because this is of the same type as HX-4. The HX-2 heat exchanger is where the warm air exchanges heat with CO_2 from the power loop. Results from those tests are shown in figure 41. The fins were removed from the air fan outlet channel for these tests.

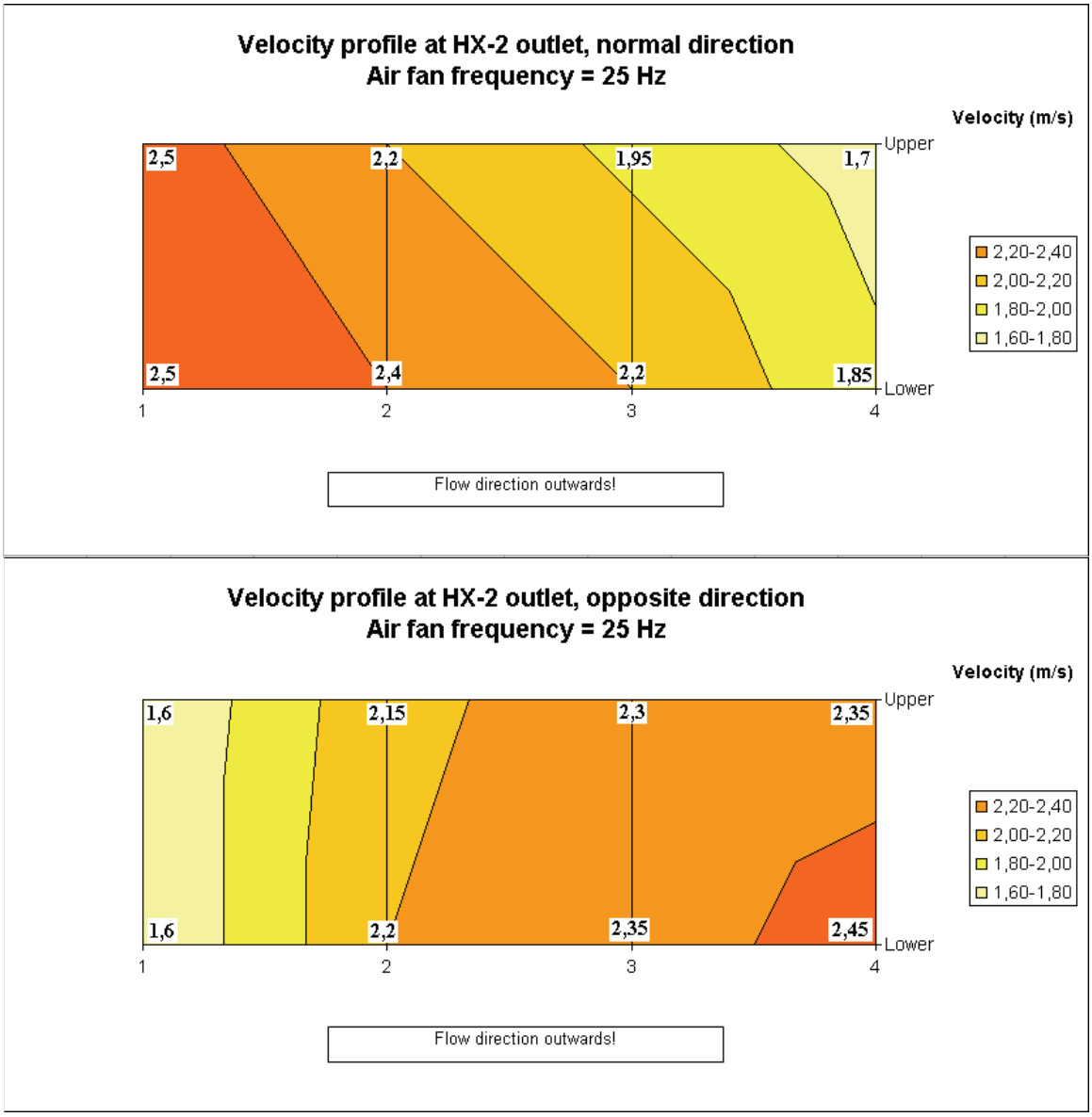

Figure 41: Constructed velocity profiles based on measured values at eight measuring points at honeycomb placed after HX-2 outlet, air fan speed set at 25 Hz. The upper figure shows the profile when HX-2 is in normal direction, while the lower figure shows the profile when HX-2 is turned in the opposite direction.

The tests of HX-2 gave the same indications as for HX-4. The air velocity profile is not very different from that found for HX-4, which could indicate a structural fault with the heat exchanger type.

3.4.1.7 Conclusion on air loop testing

To sum things up after the extensive testing; testing of the air loop showed a problem with the temperature profile of the air out of the heater. The tests show that the temperature distribution uniformity is made worse by two main factors; low air flow rate (low air fan speed) and high heater temperature set point.

A closer inspection of the air loop components and a new set of tests uncovered possible causes for the temperature profile out of the heater:

- Air velocity profile out of the air fan was distorted in such a manner that the velocity was highest at the left side and lowest at the right side, in the flow direction.
- Out of HX-4, the heat exchanger between the air loop and the heat pump, the velocity profile was opposite of what it was out of the air fan; the velocity was highest at the right side and lowest at the left side, in the flow direction. This was confirmed when the heat exchanger was tested for air flow in the opposite direction; the resulting velocity profile was reversed.
- The heat exchanger between the air loop and the power cycle, HX-2, showed similar characteristics to what was found for HX-4.
- When inspecting the heating elements of the heater with a thermal camera, results showed that the surface temperature of the elements on the left side of the channel was higher than on the right side of the channel (in the flow direction). This is in agreement with the air flow into the heater, as less air is flowing on the left side of the channel than on the right, implicating a better cooling effect on the heater elements on the right side than on the left.

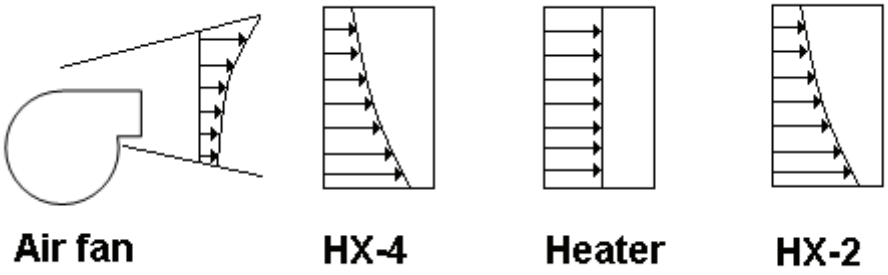

Figure 42: Air flow characteristics for the individual air loop components; air flow velocity profile as seen from above the flow channel.

Figure 42 shows a summary of how the air flow velocity profile is affected by the different components in the air loop. The heat exchangers HX-4 and HX-2 were visually inspected, but it was hard to find an obvious source for the asymmetric air flow this way. Both HX-4 and HX-2 are tube and fin heat exchangers where the pipes containing CO_2 crosses the air flow horizontally. The fins are like perforated plates where the pipes go through these perforations/holes. These fins/plates are stacked across the width of the heat exchanger with about 5 mm between each plate. One possible explanation for the air flow out of these heat exchangers is that these plates could have been displaced in such a matter that the space between the plates is smaller in some sections of the heat exchanger than others. A picture of a heat exchanger of the same kind as HX-2 and HX-4 is shown in figure 43.

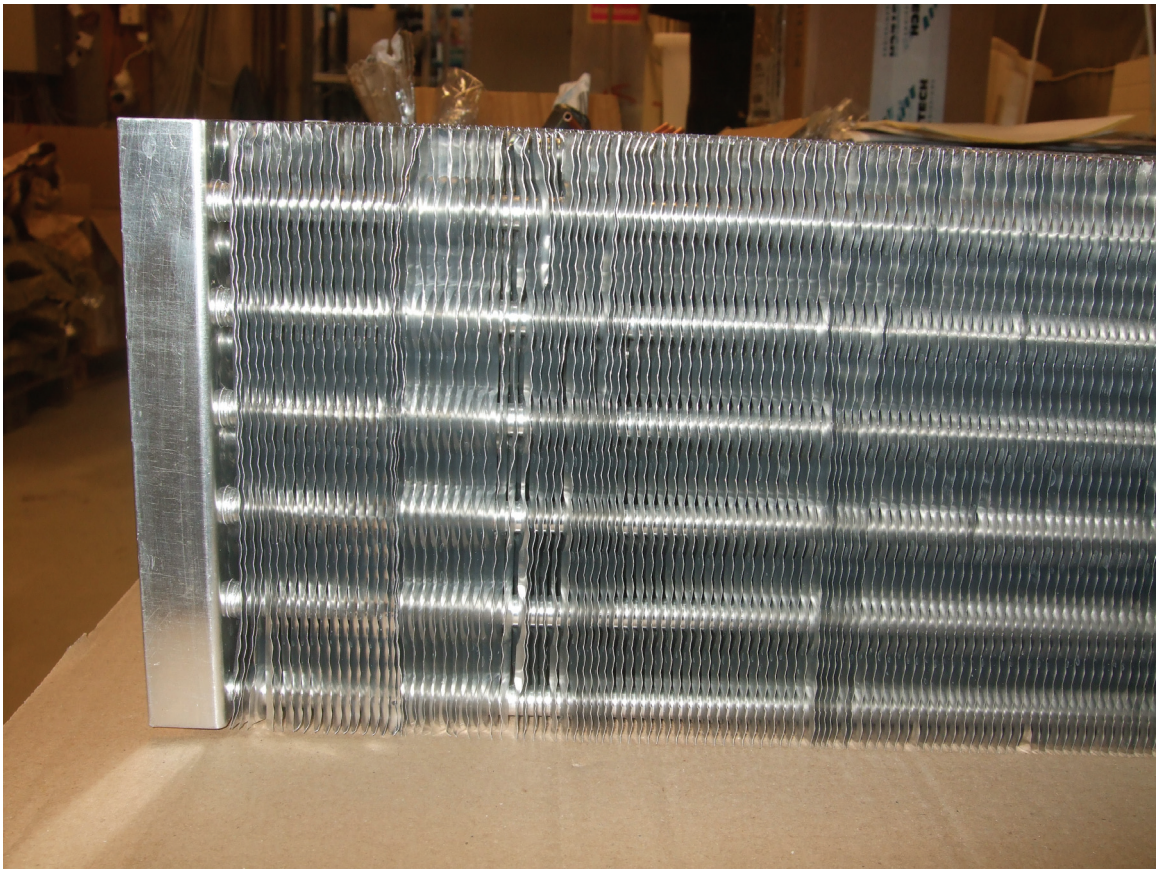

Figure 43: Picture showing the front of a heat exchanger of the same type as HX-2 and HX-4. The pipes running horizontal are where the CO_2 is flowing while the air is flowing "into" the picture.

All these factors listed above leads to an uneven temperature distribution at the cross-sectional area into HX-2. As a consequence of this, the heat transfer from the air loop to the power cycle might not be as efficient as preliminary design and simulations accounted for. This will again influence the thermal efficiency of the power cycle. The optimization of the power cycle will also be influenced by this.

On a positive note, testing and calculation of the mass flow rate in the air loop showed that the capacity of the air fan was sufficient.

3.4.1.8 Prototype simulation – New air loop conditions

As a consequence of what was found in the investigations of the air loop, new boundary conditions for the simulation of the power cycle have surfaced. The main concern is the performance of the HX-2 heat exchanger as this is a key unit in the power cycle. Because of this a new simulation of the power cycle was conducted. In this simulation of the power cycle all the conditions which were relevant were the same as for the simulation in section 3.3.1, except for the conditions related to HX-2. To incorporate the findings of the investigation of the air loop, the internal temperature approach of HX-2 was set to 20 °C instead of 10 °C. The simulation was performed for a warm air inlet temperature of 80 °C. The results from the simulation are shown below.

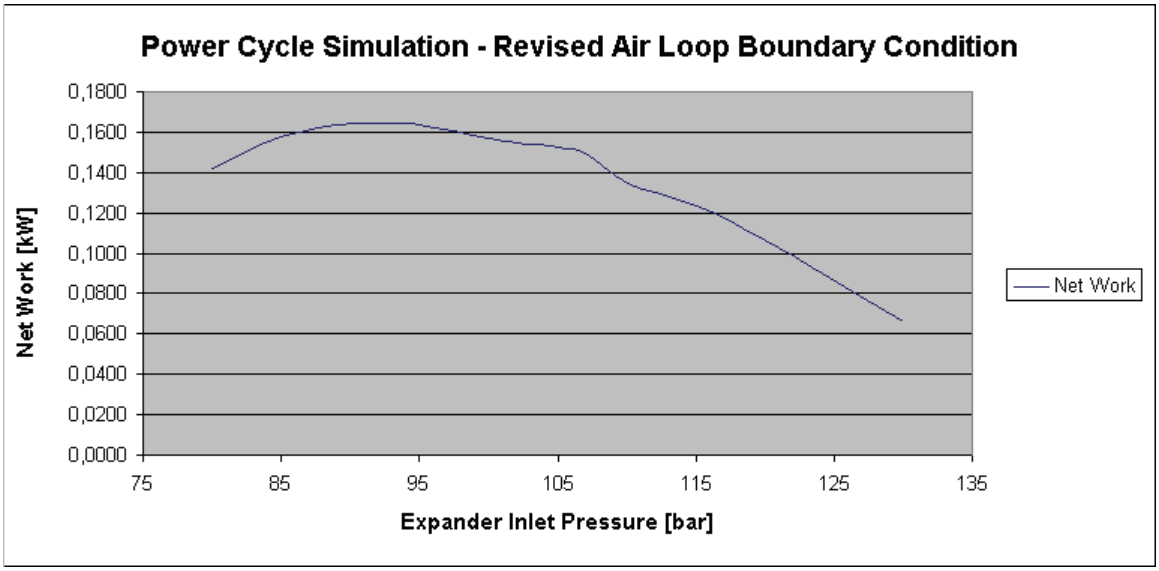

Figure 44: Optimization of net work for power cycle with new air loop boundary conditions. The minimum internal temperature approach setting was changed to 20 °C from the settings used in the original simulation.

The simulation showed a maximum net work of 164,7 W, which compared to the value in the original simulation is about 60 W less or a decrease of 27 %. The change in boundary conditions also affected the optimal expander inlet pressure which originally was 100 bar, but with the new set of conditions is found to be 92 bar. The mass flow of CO_2 in the power cycle has decreased from 108 kg/hr to 86,4 kg/hr.

The simulation shows that the performance of the air loop has a great influence on the performance of the power cycle. To improve on these results there are several possibilities.

The air loop was tested with fins installed at the air fan outlet in order to direct more air to the left of the channel. This was done to try to counteract the influence the two heat exchangers had on the air flow velocity profile. Unfortunately this did not show any substantial improvement overall to the velocity profile out of HX-4.

Another option, which has not been tested, is to turn HX-4 the other way. This could also be seen as a way to counteract the overall air flow velocity profile, but the only effect it would have on the velocity profile into the heater is that it would be inverted. It is doubtful if the air velocity profile through HX-2 would be substantially changed, especially considering the experience from the testing with fins at the air fan outlet.

3.4.2 Prototype testing - Expander

Before the expander was installed in the ROMA prototype rig, it was tested in a set up previously used for mobile air conditioning simulation. In the ROMA prototype rig, optimization of the power cycle has two aspects. One aspect is to get as much energy from the heat source to the working medium (CO_2) as possible, which increases the potential energy into the expander unit. This is very much related to the expander inlet

pressure (the pressure in the gas heater) as shown in section 3.1.2. The other aspect is to extract as much as possible of this potential energy in the expander. This amount is "decided" by the expander properties and most of all the expander isentropic efficiency. The expander isentropic efficiency describes how much of the theoretical expansion work it is possible to extract with the expander.

Since both the expander inlet conditions and the isentropic efficiency are important in the optimization of the power cycle, this forms a basis for the expander testing. The expander was tested with the aim to examine how the expander isentropic efficiency was related to the expander inlet conditions and the pressure difference across the expander. In the following section the set up and execution of the expander testing is presented along with the test results.

3.4.2.1 Expander – Test rig set up

In this circuit the expander was installed in a simple set up which included a CO_2 compressor, the expander unit itself, a gas cooler, a receiver and of course pipes and fittings.

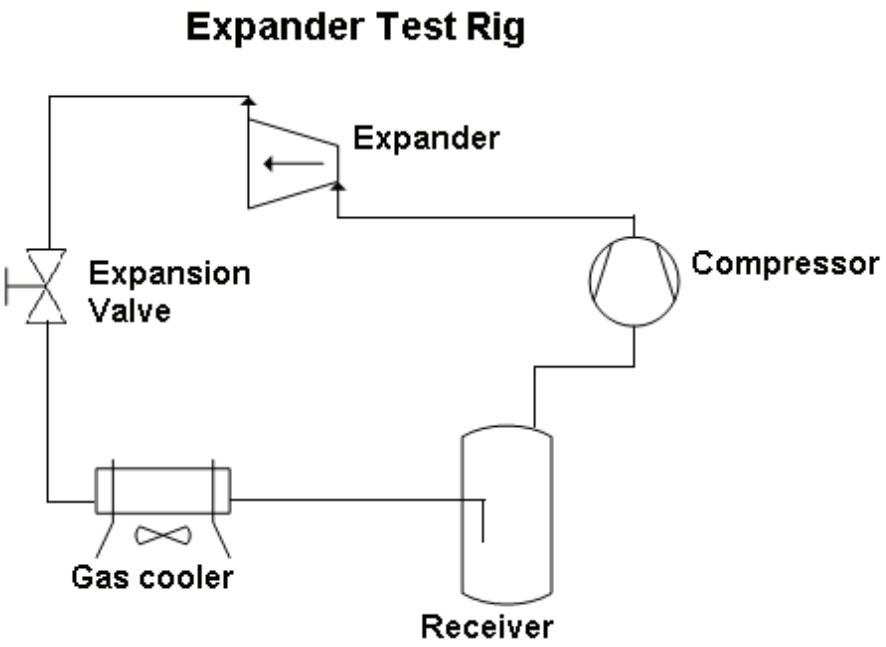

Figure 45: System drawing of the expander test rig set up.

The target for this system was to provide stable test conditions at the expander inlet and outlet, and making it as easy as possible to control these conditions. Temperature and pressure measuring devices were installed to monitor the rig and to be able to have enough data to do an accurate analysis of the tests.

The rig consisted of a CO_2 compressor which worked as the driving force of the system. The high pressure gas from the compressor was depressurized through the expander unit and the subsequent expansion valve. The low pressure gas flowed through a gas cooler

and eventually to a receiver before the gas was sucked off the top of the receiver by the compressor. This is the main difference in operation between the expander test rig and the ROMA rig. In the ROMA rig the mass flow is controlled by a CO_2 pump. The inlet fluid is an incompressible liquid, so the density changes very little with changes in pressure/temperature. The mass flow is therefore controlled solely by the rotational speed of the pump.

This is opposed to the expander test rig where the density at the inlet of the compressor was very dependent on the temperature and pressure of the fluid. This meant that the mass flow in the expander test rig was decided both by the rotational speed of the compressor and the fluid inlet conditions.

The initial tests of the expander were conducted without the use of the expansion valve. Those tests showed that there was a limitation to the pressure drop taken over the expander. Since it was of interest to examine the performance of the expander for various inlet pressures over a larger interval than the expander allowed, a prototype expansion valve was included in the test rig as seen in figure 45.

The expander was connected to a generator. The rotational speed of the expander could be controlled by adding or releasing the torque on the expander shaft.

3.4.2.2 Expander – Test rig control procedures

The primary control objective when testing the expander was to control the inlet conditions of the expander, and then mainly the inlet pressure. The control parameters used for this measure was the rotational speed of the compressor, and the expander torque and the expansion valve opening. The pressure after the expansion valve, strictly meaning the pressure in the gas cooler, responded to the outside temperature of the gas cooler (which was attempted at being kept at a constant level).

Test series of the expander were run where the inlet pressure of the expander was constant and with a variable pressure drop over the expander. To be able to keep the expander inlet pressure constant it was necessary to use the expansion valve placed after the expander. If the pressure drop across the expander was decreased, the expansion valve opening had to be decreased to compensate and keep the inlet pressure of the expander at the same level.

The system mass flow could be regulated by either increasing the rotational speed of the compressor or increasing the CO_2 filling in the system. By increasing the CO_2 filling the inlet pressure of the compressor would increase. When the pressure increased so would the density of the gas, and more mass per volume would be drawn into the compressor inlet thus increasing the mass flow.

By increasing the rotational speed of the compressor, the volumetric flow rate would increase (assuming stable inlet conditions for the compressor), and thus the mass flow rate increased as a consequence.

3.4.2.3 Expander – Test results

In the ROMA rig the lower (condensation) pressure is somewhat constant, i.e. to optimize the power cycle what matters the most is the pressure through the gas heater. The pressure out of the gas heater is the same as the expander inlet pressure. The expander inlet pressure is the sum of the condensation pressure and the pressure difference across the expander. From this it can be seen that to optimize the power cycle it is crucial to know how the expander unit behaves, especially from variations in expander inlet pressure and pressure difference across the expander. The primary objective with the expander testing was to examine how the isentropic expander efficiency corresponded to changes in the pressure difference across the expander.

The expander testing was conducted with the aim to examine some important characteristics for the expander. Three test series were taken, with constant expander inlet pressure at 84 bar, 90 bar and 100 bar. For each test series the total pressure drop was divided between the expander and the expansion valve. Having a large torque on the expander, and the expansion valve at maximum opening meant that most of the total pressure drop was taken in the expander. Decreasing the torque and adjusting the expansion valve would decrease the pressure drop across the expander and increase it across the expansion valve. This way the expander isentropic efficiency could be tested for various pressure drops across the expander while maintaining a constant expander inlet pressure. The mass flow of CO_2 was kept at a close to constant rate, and the compressor ran at 15 Hz.

Each test in the test series contains 15 sample points taken at 60 second intervals.

Expander inlet pressure 84 bar

The first test series was run with a constant expander inlet pressure of 84 bar. The results from this series are given in figure 46 below.

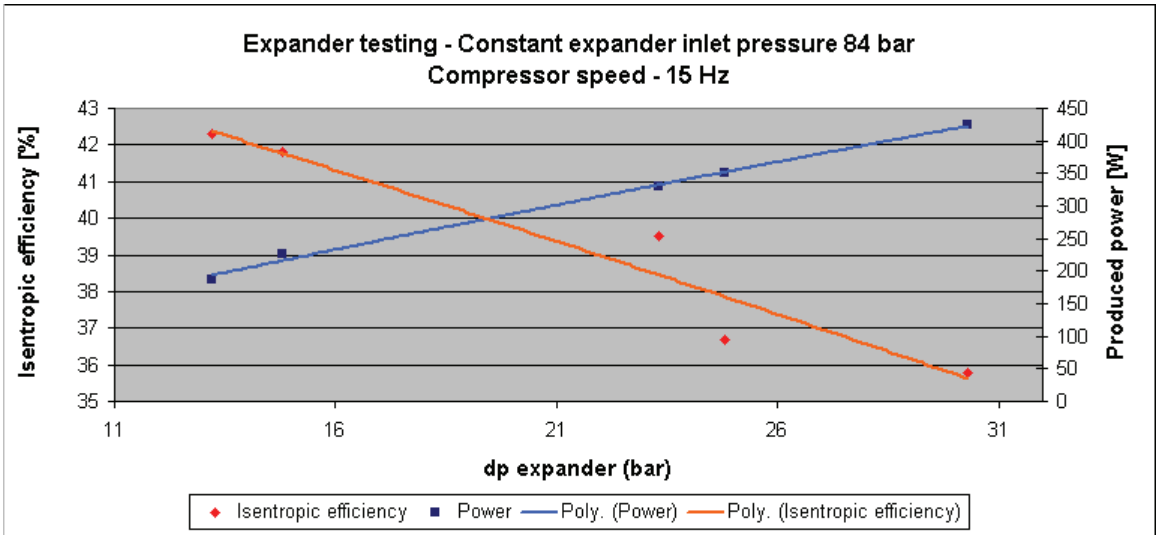

Torque, expander	**Nm**	0,897	0,697	0,646	0,329	0,306
Rpm, expander	**min^{-1}**	4513	4791	4891	6559	5795
Power	**W**	424	350	331	226	186
Massflow $_{CO2}$	**kg/min**	3,516	3,578	3,370	3,587	3,133
Temperature, expander in	**C**	74,0	73,8	74,1	74,5	80,8
Pressure, expander in	**bar**	84,0	84,0	84,1	84,1	84,1
Temperature, expander out	**C**	43,9	49,3	51,3	59,6	66,9
Pressure, expander out	**bar**	53,7	59,2	60,8	69,3	70,9
dp Expander	**bar**	30,3	24,8	23,3	14,8	13,2
Expander efficiency	**%**	35,8	36,7	39,5	41,8	42,3
dp Valve	**bar**	2,0	6,5	7,6	15,9	22,0

Figure 46: Chart and table for the testing of the expander at constant inlet pressure of 84 bar. Trendlines are added in the chart to display the tendencies for power production and isentropic efficiency in relation to pressure difference.

The chart in figure 46 shows the values for isentropic efficiency on the left axis and the produced power on the right axis. As can be seen from the graphs the tests did not reveal any definitive maximum for neither the isentropic efficiency nor the produced power at the pressure difference interval. While the isentropic efficiency displays a strong decrease when the pressure difference across the expander increases, the produced power from the generator almost doubles from 15 bar to 30 bar.

It should also be pointed out that the last test in the series was run with a little lower mass flow than the other tests. This was done in order to maintain a constant expander inlet pressure while decreasing the pressure difference across the expander. Since the adjustment of the torque on the expander had reached its minimum, some CO_2 had to be taken out of the system to get the expander inlet pressure down to 84 bar.

Expander inlet pressure 90 bar

The next test series was carried out at constant expander inlet pressure of 90 bar. This time the series contained more tests, i.e. the changes in pressure difference were taken at smaller intervals.

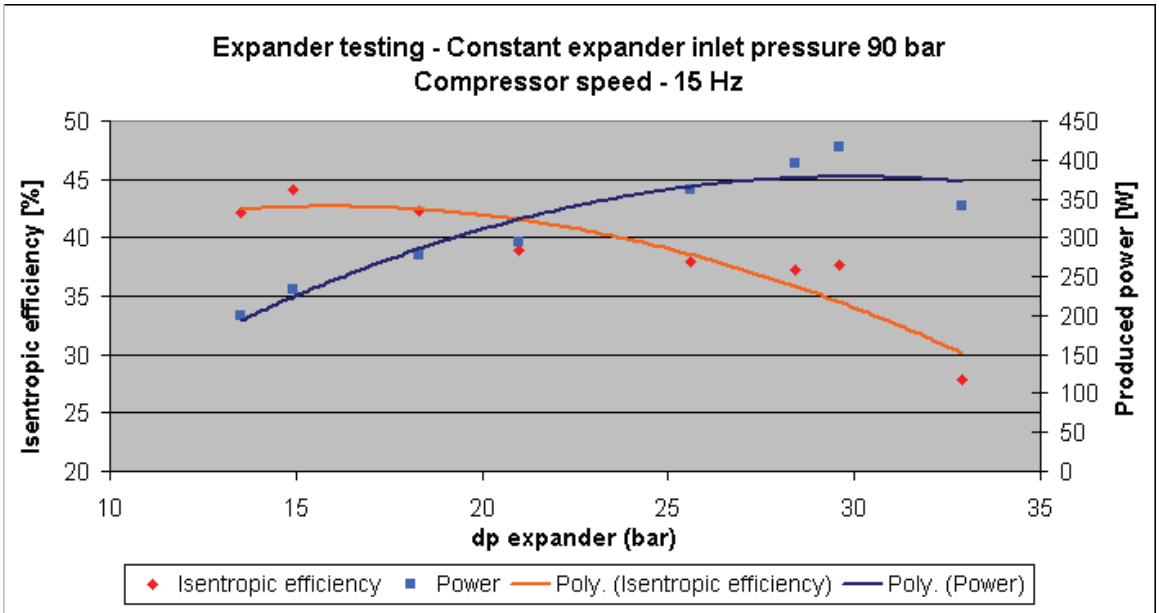

Torque, expander	**Nm**	0,995	0,889	0,823	0,726	0,564	0,455	0,341	0,288
Rpm, expander	**min^{-1}**	3275	4471	4587	4756	5004	5806	6521	6610
Power	**W**	341	416	395	362	295	277	233	199
Massflow $_{CO2}$	**kg/min**	3,557	3,625	3,664	3,683	3,679	3,659	3,681	3,681
Temperature, expander in	**C**	79,2	79,0	78,9	79,0	79,3	79,9	79,5	79,8
Pressure, expander in	**bar**	90,2	90,0	90,1	90,0	90,1	90,0	90,0	90,0
Temperature, expander out	**C**	50,0	51,7	53,0	55,7	60,3	63,3	65,7	67,4
Pressure, expander out	**bar**	57,3	60,4	61,7	64,4	69,1	71,7	75,1	76,5
dp Expander	**bar**	32,9	29,6	28,4	25,6	21,0	18,3	14,9	13,5
Expander efficiency	**%**	27,8	37,6	37,2	38,0	38,9	42,3	44,1	42,1
dp Valve	**bar**	4,9	6,9	7,7	9,9	14,3	16,9	20,2	21,5

Figure 47: Chart and table for the testing of the expander at constant inlet pressure of 90 bar. Trendlines are added in the chart to display the tendencies for power production and isentropic efficiency in relation to pressure difference.

In contrast to the test series for expander inlet pressure at 84 bar, this time a maximum value was seemingly found for both the isentropic efficiency and the produced power. More tests also meant more plots in the chart, which consequently makes it easier to see any tendencies or trends. This is displayed by the trendlines added in the chart as well.

Expander inlet pressure 100 bar

The final test series for constant expander inlet pressure was taken at a pressure level of 100 bar. The results from these tests are shown in figure 48.

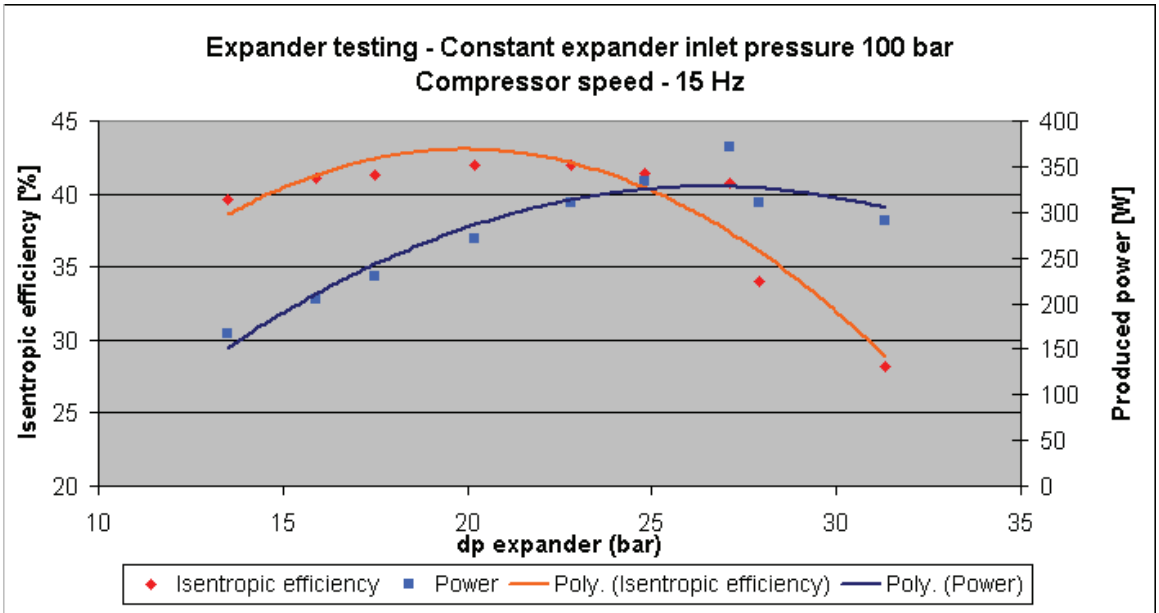

Torque, expander	**Nm**	0,946	0,834	0,807	0,733	0,660	0,565	0,464	0,392	0,282
Rpm, expander	**min^{-1}**	2926	3554	4404	4335	4479	4574	4740	4992	5639
Power	**W**	290	310	372	333	310	271	230	205	167
Massflow $_{CO2}$	**kg/min**	3,582	3,593	3,598	3,594	3,602	3,608	3,615	3,612	3,599
Temperature, expander in	**C**	84,9	85,8	90,0	86,4	86,8	87,0	87,4	87,5	88,1
Pressure, expander in	**bar**	100,2	100,0	100,1	100,1	100,0	100,1	100,0	100,2	100,1
Temperature, expander out	**C**	59,3	62,7	67,1	65,4	67,5	70,0	72,5	74,1	76,5
Pressure, expander out	**bar**	68,9	72,1	73,0	75,3	77,2	79,9	82,5	84,3	86,6
dp Expander	**bar**	31,3	27,9	27,1	24,8	22,8	20,2	17,5	15,9	13,5
Expander efficiency	**%**	28,2	34,0	40,7	41,4	42,0	42,0	41,3	41,1	39,6
dp Valve	**bar**	16,4	18,6	17,3	21,5	22,9	25,4	27,8	29,5	31,8

Figure 48: Chart and table for the testing of the expander at constant inlet pressure of 100 bar. Trendlines are added in the chart to display the tendencies for power production and isentropic efficiency in relation to pressure difference.

Compared to the test series for expander inlet pressure of 84 bar and 90 bar, the test series for expander inlet pressure of 100 bar shows a much more evident peak in the expander efficiency.

Summary of expander testing

Figure 49 displays the three test series for constant expander inlet pressure together in one chart. This chart clearly shows the displacement of the maximum isentropic efficiency towards higher pressure difference across the expander when the expander inlet pressure increases.

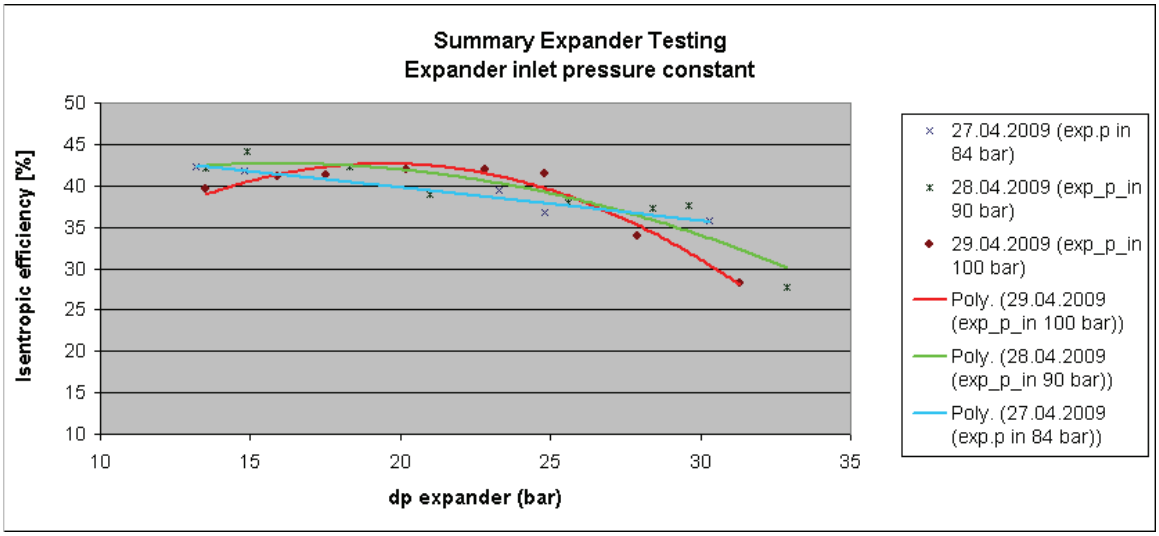

Figure 49: The test series for constant expander inlet pressure with trendlines displayed.

Some important conclusions can be drawn from the expander testing:

- The maximum isentropic efficiency seems to be found at increasing pressure difference across the expander as the expander inlet pressure increases (the vertex of the curves for isentropic efficiency moves to the right in the chart for increasing expander inlet pressure).
- The maximum isentropic efficiency found from all test series is 44,1 %, at an expander inlet pressure of 90 bar. There is not enough data to make conclusions on whether this maximum value is an irregularity or if it implies that the maximum isentropic efficiency increases or decreases as the expander inlet pressure decreases.
- There is a tendency that the isentropic efficiency has a more significant decrease as the pressure difference across the expander moves away from the optimal point when the expander inlet pressure increases. This has a considerable effect on the optimization of the power cycle as it will be even more critical to have stable inlet conditions for the expander.

3.4.2.4 Consequences of expander performance

There are two important expander characteristics which have been investigated in these tests. The first one is the isentropic efficiency and how it varies with the pressure difference across the expander. The other characteristic is the limitation on the pressure difference across the expander, giving an upper limit for the expander inlet pressure had the expander been the only expansion device in the circuit.

In relation to the ROMA rig where the expander is planned to be used, there is an optimal expander inlet pressure related to the temperature of the heat source which maximizes the net power produced in the power cycle. These optimal values were found in the simulation described in section 3.3.1. For example if the heat source is air at 80 °C the

optimal expander inlet pressure is simulated to 100 bar. In the same simulation the condensation pressure is set to 60 bar, which means an expansion pressure difference of 40 bar. Relating this pressure difference to the test results presented above, it is pretty clear that such a pressure difference, if obtainable, gives a poor isentropic efficiency.

Even though the use of an expansion valve after the expander is necessary for the initial test runs of the ROMA rig to obtain high enough pressures, this is most of all done for practical reasons. In reality one could place two or more of these expanders in series in order to obtain the highest possible isentropic efficiency in total. It is also probable that the small size of the expander results in a lower isentropic efficiency than it would have been for a larger unit. This is mainly due to leakage effects which are more substantial for a small unit than for a larger unit. This is illustrated in the figure and explanation below.

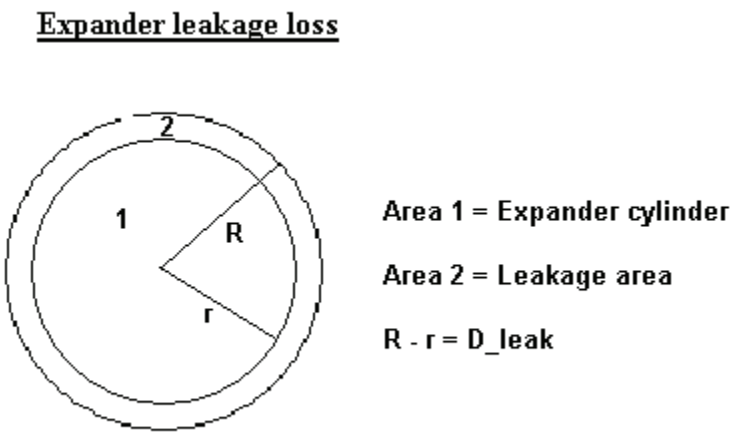

Figure 50: A simple drawing to explain the relation between expander leakage loss and expander size.

For this illustration the expander is simplified to a cylinder which separates two pressure levels by area 1 (see fig 50) and which moves by the work done by the pressure on area 1. Due to the movement of the cylinder, there needs to be a clearance distance between the cylinder and the cylinder wall. This clearance corresponds to a leakage area, area 2, in the horizontal plane, where gas freely can move from the high pressure side to the low pressure side of the expander (cylinder). This leakage loss is then quantifiable as a loss in potential expander work, and results in a decrease of the isentropic efficiency.

The area of the expander cylinder top surface is described by

Equation 22

$$A_1 = \Pi r^2$$

The leakage area, which is the area between the cylinder and the cylinder wall is described by

Equation 23

$$A_1 = \Pi R^2 - \Pi r^2$$

The ratio between the leakage area and the cylinder top surface area, A_2/A_1, can be arranged as

Equation 24

$$\frac{A_2}{A_1} = \left(\frac{1}{1 - \frac{D\_leak}{R}} \right)^2 - 1$$

In equation 24 D_leak is the clearance between the cylinder and the cylinder wall. An increase in the expander dimensions corresponds to an increase in R, while D_leak is unchanged. From the equation it can then be seen that an increase in the expander dimensions decreases the ratio between the leakage area and the cylinder top surface area, meaning that the relative effect of gas leakage decreases as the size of the expander increases.

This is a simplification of the real case for leakage effects in a turbine/expander, only meant to illustrate the principle that the relative leakage losses decreases as the expander unit increases. The expander used in the ROMA project is a black box, i.e. the principles and construction of the expander is unknown. The geometry used to explain the leakage effects are therefore not directly relatable to the expander in use, but the principles are still applicable.

3.4.2.5 Prototype simulation – New expander conditions

The original simulation of the prototype rig was done with a constant isentropic efficiency for the expander unit of 80 %. Since the test of the expander unit has shown how the isentropic efficiency relies on the pressure difference across the expander (with a considerably lower value than used in the simulation), as well as the inlet pressure of the expander, this simulation has some weaknesses when comparing it to reality.

To have simulation results which are closer to reality, the results from the expander testing were incorporated in a new simulation of the power cycle. The isentropic efficiency was changed from a constant value to a function of the pressure difference across the expander. This is still a simplification of reality. An equation for the isentropic efficiency was established by incorporating a trend line equation based on the measured isentropic efficiencies from the test series of constant expander inlet pressure.

Two cases were investigated in the new simulations. One case was to find the optimum high pressure of the power cycle when only the expander is utilized. The other case was to find the optimum high pressure of the power cycle when an expansion valve is utilized in the power cycle together with the expander. Both cases were conducted with air at an inlet temperature of 80 °C.

The test results for expander isentropic efficiencies at constant expander inlet pressure were used to create an equation for the isentropic efficiency as a function of pressure difference across the expander. The resulting equation was:

Equation 25

$$\eta_{is} = -0{,}0557DP^2 + 1{,}9605DP + 25{,}007$$

How this equation fits with the experimental data is shown in figure 51.

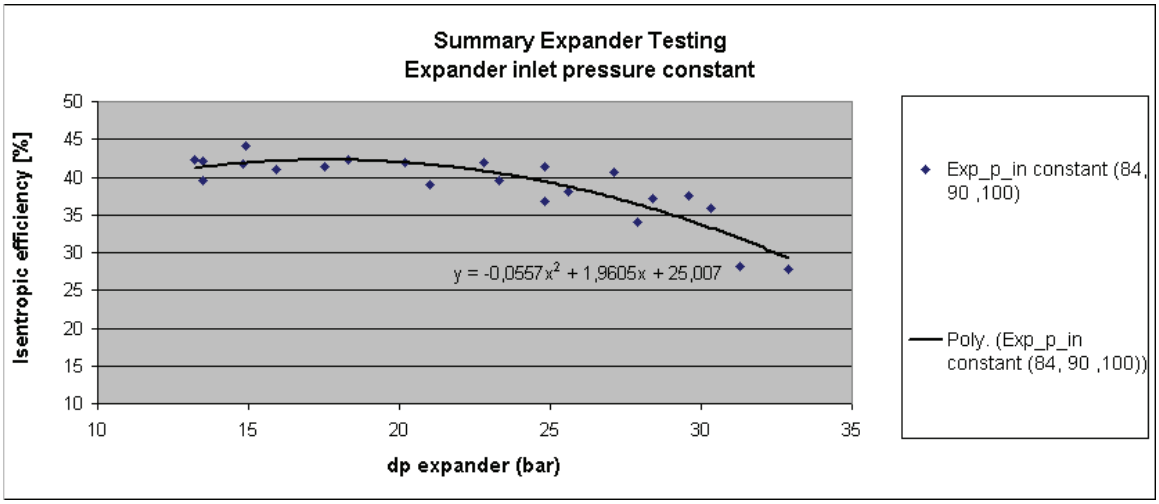

Figure 51: The test results for expander isentropic efficiencies (for all three inlet pressures) were used to decide a trendline equation for use in a new simulation of the power cycle.

Equation 25 was then used in the simulations to calculate the isentropic efficiency for varying pressure difference across the expander.

For the simulation case where the power cycle was simulated without the expansion valve installed, the resulting net work curve is displayed in figure 52.

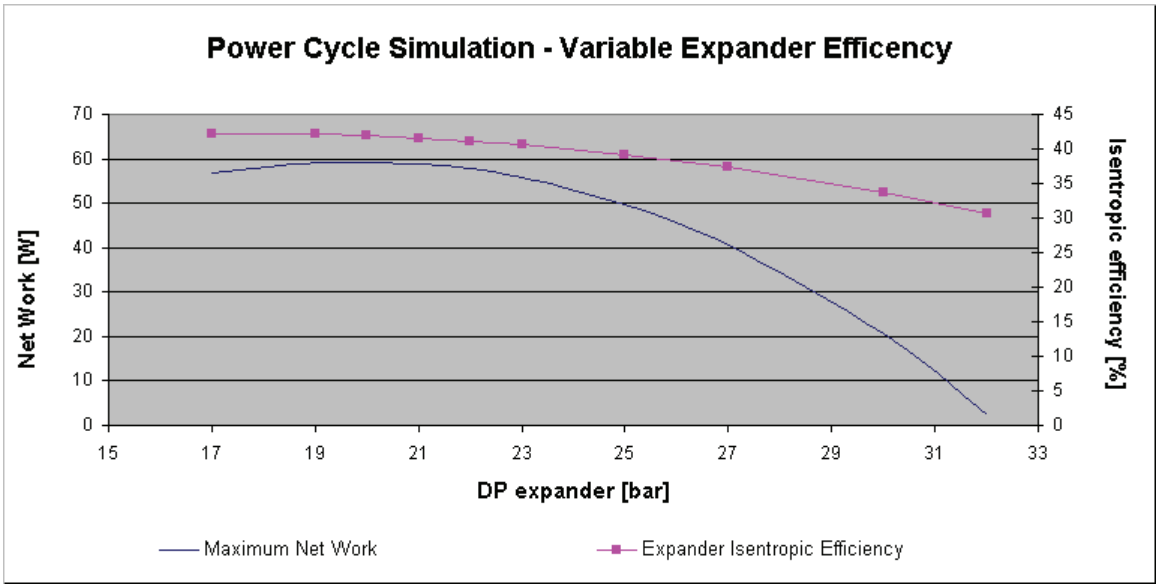

Figure 52: Simulation results for the power cycle with the expander efficiency as a function of the pressure difference across the expander.

The maximum net work was found at a pressure difference of 20 bar, which equates to an expander inlet pressure of 80 bar. This is 20 bar less than the optimal expander inlet pressure found in the original simulation. The maximum net work was found to be 59,3 W, which is quite less than the 225 W in the original simulation. There are mainly two reasons for this drastic reduction in net work. The first, and quite obvious, is the lower expander efficiency, which from the initial simulation is reduced almost to half the value. The other reason is from the opposite effects on the heat source utilization and the isentropic efficiency when increasing the pressure difference across the expander. The more heat is extracted from the heat source, the more heat is available at the expander inlet for conversion to electrical energy. As found from the initial simulation, the heat source utilization increases up to an expander inlet pressure of 100 bar. But while increasing pressure difference across the expander increases the heat source utilization, it also decreases the expander isentropic efficiency. So while more potential heat energy is available by increasing the pressure difference across the expander, a less amount of this energy is converted to mechanical work/electrical energy in the expander due to the continuous decrease in the expander isentropic efficiency.

The results from the simulation where the expansion valve is included in the power cycle as well are shown in figure 53.

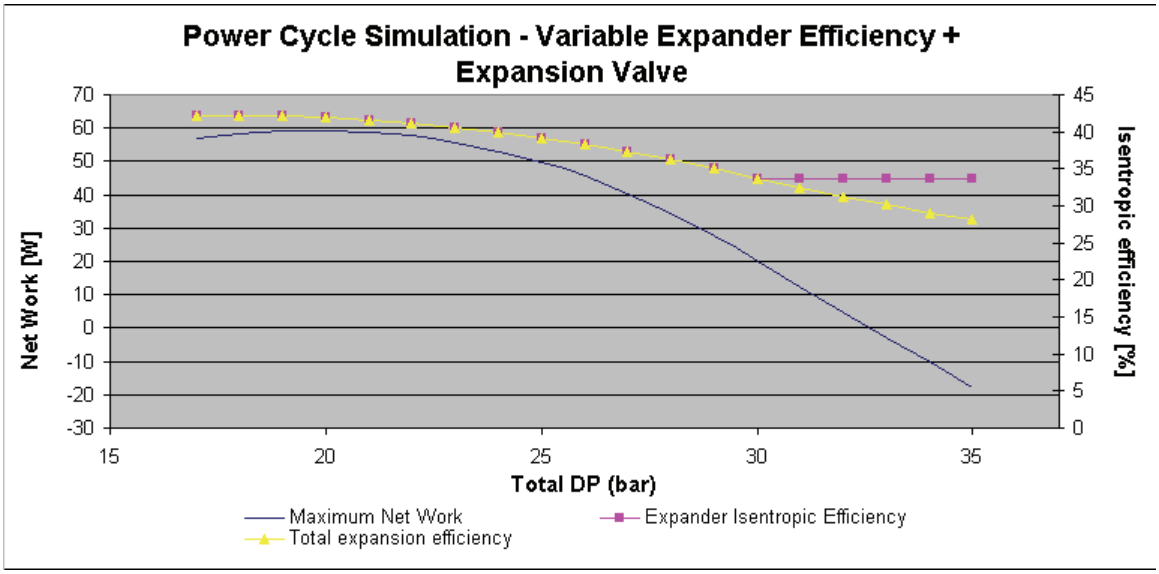

Figure 53: Simulation results for the power cycle with the expander efficiency as a function of the pressure difference across the expander, and an expansion valve installed in the cycle right after the expander. Also shown is the total isentropic expansion efficiency which deviates from the expander efficiency at total pressure differences above 30 bar as this is where the additional pressure drop is taken through the expansion valve.

The simulation of the power cycle with the expander and valve combination at a hot air temperature of 80 °C shows that incorporation of the valve does not increase the maximum net work. The simulation shows though that for a total pressure difference of more than 30 bar, the inclusion of the valve improves the net work compared to the net work output for the power cycle without the expansion valve. At total pressure differences above 30 bar the optimal set up is to maintain a pressure difference across the expander of 30 bar, while the rest of the expansion is taken through the expansion valve. This is the reason the curve for expander isentropic efficiency is flat from a total pressure difference of 30 bar and onward. A curve for the total isentropic expansion efficiency is included in the figure as well. This total efficiency is calculated as expander work divided by the maximum theoretical work done by an expansion work for the total pressure drop. This is the reason it is lower than the expander isentropic efficiency from a total pressure difference of 30 bar, when the expansion valve goes into use.

For total pressure difference up to 30 bar, the curves for both maximum net work and expander isentropic efficiency are the same in figure 52 and figure 53. Since the optimal pressure difference regarding maximum net work lies below 30 bar, the conclusion is that for a hot air temperature at 80 °C there is no need for an expansion valve to improve the performance of the power cycle.

These simulations have not been conducted for hot air temperatures of 120 °C and 160 °C, but there is a possibility that the expansion valve will improve the performance of the power cycle at these temperature levels. It should be underlined though that the incorporation of the expansion valve is only meant to establish the desired working conditions for the expander in the case of testing in the laboratory. In a real commercial

power plant, the expansion valve could be replaced by one or more expander units in series.

4. Conclusions

This report is a conclusion on work done as part of the ROMA (Resource Optimization and recovery in the materials industry) Energy Recover project. This project is involved in the development of a new technology for power production from low temperature heat sources such as off gas from aluminum production cells. The technology is based on the use of CO_2 as a working fluid in a trans-critical Rankine cycle, as this is a principle which theoretically improves the utilization of low temperature heat sources.

In the development of this new technology a prototype was planned built early in 2009. At the center of this prototype is the CO_2 power cycle with a new prototype expander unit as the core. In addition the prototype constitutes of two circuits which functions as the boundary conditions for the power cycle. The air loop delivers heat to the power cycle and is meant to simulate the real heat source, the off gas from the aluminum production cells. The other circuit, the ethylene glycol loop, provides the cooling for the power cycle. Working as a supplementary circuit is a CO_2 heat pump which takes heat from the ethylene glycol loop and provides heat to the air loop.

The work with the ROMA Energy Recovery project and the power production from waste heat prototype started with a detailed simulation and uncertainty analysis of the prototype in the autumn of 2008. This was then used to improve on the design and to do further calculations of the prototype. This work was continued with the Master thesis where the main focus was on instrumentation and experimental investigation of the prototype.

In the ROMA prototype rig, optimization of the power cycle has two aspects. One aspect is to take out as much energy from the heat source as possible, which increases the potential energy into the expander unit. This is very much related to the expander inlet pressure (the pressure in the gas heater) and the heat transfer from the warm air to the CO_2 in the power cycle. The other aspect is to extract as much as possible of this potential energy in the expander. This amount is “decided” by the expander properties and most of all the expander isentropic efficiency. The expander isentropic efficiency describes how much of the theoretical expansion work it is possible to extract with the expander.

Because of a delay in the completion of the prototype rig, most of the experimental investigation was carried out on the individual cycles, mainly the air loop, its components and the expander unit.

The investigation of the air loop included leakage tests, mass flow measurements, installation and investigation of thermocouples, investigation of temperature profile, air flow velocity profile and the individual components of the air loop. The investigation uncovered some irregularities which would and will affect the performance of the

prototype system. These irregularities were shown as a maldistribution of the temperature of the air flowing into the air-to- CO_2 heat exchanger where heat is provided to the power cycle (HX-2). Further investigation showed that there was a problem with distributing the air uniformly across the channels; more air flowed on the right side of the air channel into HX-2 than on the left side. This tendency could also be traced to the inlet of the heater, which provided the heating of the air and was situated right in front of HX-2.

The main source for the irregular air flow proved to be the two air-to- CO_2 heat exchangers (HX-2 and HX-4). These heat exchangers were both of the same kind of tube and fin heat exchangers. Most likely due to a production error, air flowed through much easier on the right side than on the left side of the heat exchangers.

A consequence of the temperature maldistribution and air flow into HX-2 is that the heat transfer from the air loop to the power cycle might not be as efficient as the preliminary design and simulations accounted for. A new simulation of the power cycle where the effects from the investigation of the air loop were incorporated was conducted, with a warm air temperature of 80 °C. It showed a reduction in the maximum net work by 27 %, from 225 W to 165 W, and it also affected the optimal expander inlet pressure which was reduced from 100 bar to 92 bar.

The investigation of the expander unit was performed in a simpler set up compared to the power cycle it is intended to be used in. The main properties investigated in these tests were how the isentropic efficiency was related to the inlet pressure of the expander and the pressure difference across the expander. Initial tests also proved limitations on the pressure difference obtainable across the expander.

The expander was tested for inlet pressures of 84 bar, 90 bar and 100 bar. The pressure drop across the expander was varied and the resulting isentropic efficiency was found for each test. A prototype expansion valve installed after the expander, was used to maintain the expander inlet pressure when the pressure difference across the expander was changed.

The resulting curves for the expander isentropic efficiency indicated that the pressure difference across the expander at which the maximum isentropic efficiency was found, increased when the expander inlet pressure was increased. Another tendency observed was that for increasing expander inlet pressures, the isentropic efficiency had a more significant decrease when moving away from the optimal pressure difference across the expander. As a result the need for stable expander inlet conditions increases as the expander inlet pressure increases. Overall the expander efficiency was never measured above 45 %. Some of the expansion work loss can be attributed to the small size of the expander, since the leakage loss relative to the mass flow for a turbine/expander increases as the size of the turbine/expander decreases.

Since the real expander efficiency proved to be quite lower than the value used in the prototype simulation, new simulations were carried out. In these simulations (for warm air temperature of 80 °C) the expander isentropic efficiency was represented as a function

of the pressure difference across the expander, where the function was based on the test data. Two simulations were carried out, one of the power cycle without the expansion valve installed and one of the power cycle with the expansion valve installed to see if this could improve the resulting net work. The simulation results showed that the new conditions reduced the maximum net work from 225 W to 59,3 W and this maximum net work was found at a pressure difference of 20 bar, i.e. 20 bar less than what was found in the original simulation. This is mainly a result of the reduced expander efficiency. But it is also a result of the opposite effects it has on the heat source utilization and the isentropic efficiency when the pressure difference across the expander is increased beyond the optimal value.

The new simulations also showed that, for a warm air temperature of 80 °C, the use of an expansion valve after the expander did not increase the maximum net work produced in the power cycle.

All in all the investigation of the prototype power production system uncovered some flaws and characteristics which will prove important in the optimization of the prototype system. Both the performance of the air loop and the characteristics of the expander are hard to improve without doing major changes to either. In the case of the air loop, the main problem seems to lie with the two air-to-CO_2 heat exchangers. The most effective way to improve the performance of the air loop is therefore to replace those two heat exchangers. But since this has an economic cost as well as being time consuming (the heat exchangers has to be disconnected from the air loop and replaced with the new ones, this means instrumentation of parts of the air loop has to be done all over again), the most likely result from the air loop testing is the awareness of the problem and to incorporate this in the optimization of the prototype rig.

Regarding the results from the expander testing, these will be important in the control strategy and optimization of the rig, as shown in the new simulation results.

References

[1] Hall CM. Process of reducing aluminum from its fluoride salts by electrolysis, U.S. patent 400,664 (Patent) 1889.

[2] Solheim A. Aluminiumelektrolyse: Teknologi og prinsipper. SINTEF Materialer og kjemi. 2005.

[3] Skistad H. Senior Research Scientist. Personal Communication. 7th May 2009.

[4] Minea V. Using geothermal energy and industrial waste heat for power generation. Paper presented at 2007 IEEE Canada Electrical Power Conference. Montreal, Canada.

[5] Sollesnes G, Helgerud HE. Potensialstudie for utnyttelse av spillvarme fra norsk industri. ENOVA. Report number: 1, 2009.

[6] Badr O, O'Callaghan PW, Probert SD. Rankine-cycle systems for harnessing power from low-grade energy sources. Applied Energy. 1990; 36; 263-292.

[7] Wikipedia [www.wikipedia.org]. Wikimedia Foundation. [21 November 2008 at 03:28; 13 December 2008 at 19:52]. http://en.wikipedia.org/wiki/Rankine_cycle.

[8] Hung TC, Shai TY, Wang SK. A review of organic Rankine cycles (ORCs) for the recovery of low-grade waste heat. Energy. 1997; 7; 661-667.

[9] Larjola J. Electricity from industrial waste heat using high-speed organic Rankine cycle (ORC). Int. J. Production Economics. 1995; 41; 227-235.

[10] Chinese D, Meneghetti A, Nardin G. Diffused introduction of Organic Rankine Cycle for biomass-based power generation in an industrial district: a systems analysis. Int. J. Energy Research. 2004; 28; 1003-1021.

[11] Badr O, O'Callaghan PW, Probert SD. Performances of Rankine-cycle engines as functions of their expanders' efficiencies. Applied Energy. 1984; 18; 15-27.

[12] Hettiarachchi MHD, Golubovic M, Worek WM, Ikegami Y. Optimum design criteria for an Organic Rankine cycle using low-temperature geothermal heat sources. Energy. 2007; 32;1698-1706.

[13] Liu BT, Chien KH, Wang CC. Effect of working fluids on organic Rankine cycle for waste heat recovery. Energy. 2004; 29; 1207-1217.

[14] Al-Rabghi OM, Beirutty M, Akyurt M, Najjar Y, Alp T. Recovery and utilization og waste heat. Heat Recovery Systems & CHP. 1993; 5; 463-470.

[15] Barbier E. Geothermal energy technology and current status: an overview. Renewable and Sustainable Energy Reviews. 2002; 6; 3-65.

[16] Bronicki LY. (2008, July). Advanced power cycles for enhancing geothermal sustainability. Paper presented at IEEE Power and Energy Society 2008 General Meeting: Conversion and Delivery of Electrical Energy in the 21st Century, PES. Pittsburg, PA, United States

[17] Watt Committee. Profiting from low-grade heat – Thermodynamic cycles for low temperature heat sources. London: The Institution of Electrical Engineers; 1994.

[18] Leibowitz H, Mirolli M. First Kalina combined-cycle plant tested successfully. Power Engineering. 1997; May; 44-47.

[19] Zamfirescu C, Dincer I. Thermodynamic analysis of a novel ammonia-water trilateral Rankine cycle. Thermochimica Acta. 2008; 477; 7-15.

[20] Mirolli M, Hjartarson H. Mlcak HA, Ralph M. Testing and operating experience of the 2 MW Kalina geothermal power plant in Húsavík, Iceland. OMMI. 2002; August;

[21] Valdimarsson P. The Kalina power plant in Husavik – why Kalina and what has been learned. Presentation at Energy workshop. Strasbourg, September 2006.

[22] Ronald DiPippo. Second Law assessment of binary plants generating power from low-temperature geothermal fluids. Geothermics. 2004; 33; 565-586.

[23] Moran MJ, Shapiro HN. Fundamentals of Engineering Thermodynamics. 5th Edition. Hoboken, NJ: John Wiley & Sons Inc.; 2004.

[24] Fuller B. Turbo-machinery considerations using super-critical carbon dioxide working fluids for a closed Brayton cycle. Paper presented on Symposium on supercritical CO_2 power cycle for next generation systems, MIT.

[25] Ladam Y. Power production from low to medium temperature heat sources – Literature review. SINTEF Energy Research; TR F6653.

[26] Hans T Haukås AS – NTNU – SINTEF Energiforskning AS. Kjøle- og fryseanlegg med CO_2 som kuldemedium. Trondheim: Norsk Kjøleteknisk Forening – Compendium

[27] Midtsjø A. Design and start-up of work recovery from low temperature heat sources test facility, applying CO_2 as working fluid [Project work]. Trondheim: NTNU; 2008.

[28] Coleman HW, Steele GW. Experimentation and Uncertainty Analysis for Engineers. Second Edition. New York; John Wiley & Sons Inc.;1999.

[29] Moffat RJ. Describing the uncertainties in experimental results. Experimental Thermal and Fluid Science. 1988; 1: 3-17.

[30] Wikipedia [www.wikipedia.org]. Wikimedia Foundation. [11 May 2009 at 22:20; 13 May 2009 at 16:19]. http://en.wikipedia.org/wiki/Pressure_measurement.

[31] White FM. Fluid mechanics. 5th Edition. New York, NY; The McGraw-Hill Companies, Inc.; 2003.

[32] Standard Norge. Norsk Standard: Measurement of fluid flow by means of pressure differential devices inserted in circular cross-section conduits running full; Part 1: General principles and requirements. (ISO 5167-1:2003)

[33] Standard Norge. Norsk Standard: Measurement of fluid flow by means of pressure differential devices inserted in circular cross-section conduits running full. Part 2: Orifice plates. (ISO 5167-2:2003)

[34] Baker RC. Flow measurement handbook: Industrial designs, operating principles, performance and applications. First Edition .Cambridge, UK; Cambridge University Press; 2000.

List of Figures

FIGURE 1: THE PATENT ON ALUMINUM ELECTROLYSIS DEVELOPED BY CHARLES MARTIN HALL IN 1886..... 1
FIGURE 2: THE CROSS-SECTION OF AN ALUMINUM ELECTROLYSIS CELL..... 2
FIGURE 3: ENERGY FLOW IN A TYPICAL NORWEGIAN ALUMINUM WORKS..... 4
FIGURE 4: WASTE HEAT IN THE NORWEGIAN ALUMINUM INDUSTRY SORTED BY TEMPERATURE INTERVALS .. 5
FIGURE 5: THE RANKINE CYCLE SYSTEM. 6
FIGURE 6: ENTROPY DIAGRAM FOR A STEAM RANKINE CYCLE..... 7
FIGURE 7: A COMPARISON OF THE EVAPORATION OF WATER AND AN ORGANIC FLUID 8
FIGURE 8: THE ORGANIC RANKINE CYCLE USED AS A BOTTOMING CYCLE IN THE WATER VAPOR RANKINE CYCLE. 9
FIGURE 9: SCHEMATIC DIAGRAM OF THE KALINA CYCLE'S CONDENSING ARRANGEMENT 11
FIGURE 10: SCHEMATIC REPRESENTATION OF THE IDEAL BRAYTON CYCLE IN A PRESSURE-VOLUME DIAGRAM AND A TEMPERATURE-ENTROPY DIAGRAM 12
FIGURE 11: PRESSURE-DENSITY DIAGRAM SHOWING THE PRESSURE DEPENDENCY OF DENSITY CHANGE DUE TO INCREMENTAL TEMPERATURE VARIATION. 13
FIGURE 12: PRESSURE-VOLUME DIAGRAM AND TEMPERATURE-ENTROPY DIAGRAM OF THE STIRLING CYCLE 14
FIGURE 13: THE CARNOT CYCLE ILLUSTRATED IN A TEMPERATURE-ENTROPY DIAGRAM AND A SCHEMATICALLY REPRESENTATION 14
FIGURE 14: THE IDEAL TRILATERAL CYCLE; AS A COMPOSITION OF INFINITESIMAL CARNOT CYCLES AND ON INTEGRAL FORM..... 15
FIGURE 15: GRAPHICAL REPRESENTATION OF THE IDEAL CARNOT AND TRILATERAL CYCLE EFFICIENCIES... 16
FIGURE 16: THE TRANS-CRITICAL RANKINE CYCLE SHOWN IN THE LOGARITHMIC PRESSURE–ENTHALPY DIAGRAM FOR CO_2..... 17
FIGURE 17: TEMPERATURE-ENTROPY DIAGRAM FOR A TRANS-CRITICAL HEATING OF WORKING FLUID AND A CONVENTIONAL PROCESS WITH HEAT TRANSFER TO A WORKING FLUID INSIDE TWO-PHASE AREA 19
FIGURE 18: DRAWING OF TEST FACILITY. 20
FIGURE 19: GRAPHICAL SET UP OF TEST FACILITY IN THE PROCESS SIMULATING TOOL PRO/II. 25
FIGURE 20: THE RELATIVE UNCERTAINTY OF THE HEAT DUTIES OF HX-3, HX-7 AND HX-8, FOR THE ETHYLENE GLYCOL SIDE, AS A RESULT OF VARIATION OF THE TEMPERATURE UNCERTAINTY. 29
FIGURE 21: THE RELATIVE UNCERTAINTY OF THE NET WORK AND THERMAL EFFICIENCY AS A RESULT OF VARIATION OF THE TEMPERATURE UNCERTAINTY ON TEMPERATURES ON BOTH SIDES OF THE EXPANDER AND THE PUMP IN THE CO_2 POWER CYCLE. 30
FIGURE 22: THE RELATIVE UNCERTAINTY OF NET WORK AND THERMAL EFFICIENCY AS A FUCTION OF THE TORQUE AND ROTATIONAL SPEED ACCURACY..... 30
FIGURE 23: SIMPLE MANOMETER USED TO MEASURE A PRESSURE DIFFERENCE..... 32
FIGURE 24: SKETCHES OF THE SET UP OF THERMOCOUPLES IN FRONT OF AND AFTER HX-2. 34
FIGURE 25: PICTURE OF THERMOCOUPLE INSTALLATION AT HEAT EXCHANGER INLET..... 35
FIGURE 26: PICTURE SHOWING THE ROMA PROTOTYPE RIG 36
FIGURE 27: GEOMETRY AND FLOW PATTERNS IN THE ORIFICE PLATE SET UP..... 37
FIGURE 28: TEMPERATURE DISTRIBUTION IN FRONT OF AND AFTER HEAT EXCHANGER. THE TEMPERATURE RESPONSE WHEN AIR FAN SPEED CHANGES FROM 50 HZ TO 25 HZ, THE HEATER TEMPERATURE SET POINT IS CONSTANT AT 80 °C. 40
FIGURE 29: TEMPERATURE DISTRIBUTION IN FRONT OF AND AFTER HEAT EXCHANGER. THE TEMPERATURE RESPONSE WHEN AIR FAN SPEED CHANGES FROM 25 HZ TO 50 HZ, THE HEATER TEMPERATURE SET POINT IS CONSTANT AT 80 °C. 41
FIGURE 30: TEMPERATURE DISTRIBUTION IN FRONT OF AND AFTER HEAT EXCHANGER. THE TEMPERATURE RESPONSE WHEN THE HEATER TEMPERATURE SET POINT IS CHANGED FROM 80 °C TO 100 °C. THE AIR FAN FREQUENCY IS CONSTANT AT 50 HZ. 42
FIGURE 31: TEMPERATURE DISTRIBUTION IN FRONT OF AND AFTER HEAT EXCHANGER. THE TEMPERATURE RESPONSE WHEN THE HEATER TEMPERATURE SET POINT IS CHANGED FROM 50 °C TO 80 °C. THE AIR FAN FREQUENCY IS CONSTANT AT 50 HZ. 43
FIGURE 32: MEASURING POINTS FOR THE AIR VELOCITY AT THE OUTLET OF BOTH THE ELECTRIC HEATER AND THE INDIVIDUAL HEAT EXCHANGERS. 44

FIGURE 33: CONSTRUCTED VELOCITY PROFILES BASED ON MEASURED VALUES AT HEATER OUTLET 45
FIGURE 34: PICTURE OF HONEYCOMB. 46
FIGURE 35: CONSTRUCTED VELOCITY PROFILES BASED ON MEASURED VALUES AT HONEYCOMB PLACED AFTER THE HEATER OUTLET 47
FIGURE 36: PHOTOS OF THE HEATING ELEMENTS OF THE ELECTRIC HEATER WITH A THERMAL CAMERA 48
FIGURE 37: CONSTRUCTED VELOCITY PROFILES BASED ON MEASURED VALUES AT HONEYCOMB PLACED AFTER HX-4 OUTLET. 49
FIGURE 38: PICTURE TAKEN OF THE AIR FAN OUTLET. 50
FIGURE 39: CONSTRUCTED VELOCITY PROFILE BASED ON MEASURED VALUES AT HONEYCOMB PLACED AFTER AIR FAN OUTLET. 51
FIGURE 40: CONSTRUCTED VELOCITY PROFILES BASED ON MEASURED VALUES AT HONEYCOMB PLACED AFTER HX-4 OUTLET. 52
FIGURE 41: CONSTRUCTED VELOCITY PROFILES BASED ON MEASURED VALUES AT HONEYCOMB PLACED AFTER HX-2 OUTLET 53
FIGURE 42: AIR FLOW CHARACTERISTICS FOR THE INDIVIDUAL AIR LOOP COMPONENTS 54
FIGURE 43: PICTURE SHOWING THE FRONT OF A HEAT EXCHANGER OF THE SAME TYPE AS HX-2 AND HX-4 55
FIGURE 44: OPTIMIZATION OF NET WORK FOR POWER CYCLE WITH NEW AIR LOOP BOUNDARY CONDITIONS 56
FIGURE 45: SYSTEM DRAWING OF THE EXPANDER TEST RIG SET UP. 57
FIGURE 46: TESTING OF THE EXPANDER AT CONSTANT INLET PRESSURE OF 84 BAR 60
FIGURE 47: TESTING OF THE EXPANDER AT CONSTANT INLET PRESSURE OF 90 BAR 61
FIGURE 48: TESTING OF THE EXPANDER AT CONSTANT INLET PRESSURE OF 100 BAR 62
FIGURE 49: THE TEST SERIES FOR CONSTANT EXPANDER INLET PRESSURE WITH TRENDLINES DISPLAYED. ... 63
FIGURE 50: THE RELATION BETWEEN EXPANDER LEAKAGE LOSS AND EXPANDER SIZE. 64
FIGURE 51: TRENDLINE EQUATION FOR USE IN A NEW SIMULATION OF THE POWER CYCLE. 66
FIGURE 52: SIMULATION RESULTS FOR THE POWER CYCLE WITH THE EXPANDER EFFICIENCY AS A FUNCTION OF THE PRESSURE DIFFERENCE ACROSS THE EXPANDER. 67
FIGURE 53: SIMULATION RESULTS FOR THE POWER CYCLE WITH THE EXPANDER EFFICIENCY AS A FUNCTION OF THE PRESSURE DIFFERENCE ACROSS THE EXPANDER, AND AN EXPANSION VALVE INSTALLED IN THE CYCLE RIGHT AFTER THE EXPANDER. 68

Appendix A: Additional test expander test results

Constant mass flow rate

The first few test series were run with a constant mass flow rate. The expansion valve was kept fully open while the pressure drop over the expander was varied by varying the torque on the expander shaft. For the first test series the compressor ran on a speed of 15 Hz.

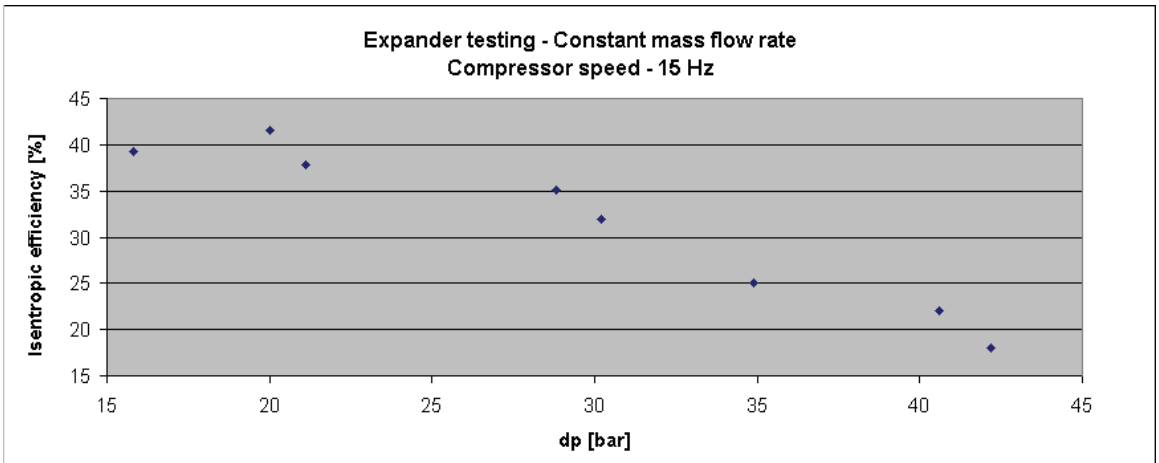

Compressor speed	**Hz**	15	15	15	15	15	15	15	15
Torque, expander	**Nm**	0,337	0,492	0,533	0,796	0,899	1,068	1,261	1,332
Rpm, expander	**min^{-1}**	7704	6991	6017	4799	4001	2973	2501	1975
Power	**W**	272	360	336	400	377	332	330	275
Massflow $_{CO2}$	**kg/min**	3,46	3,51	3,48	3,46	3,49	3,51	3,52	3,50
Temperature, expander in	**C**	61,6	70,0	65,1	72,6	75,7	80,0	86,2	86,8
Pressure, expander in	**bar**	68,5	74,1	73,3	81,6	84,5	89,5	96,0	97,3
Temperature, expander out	**C**	44,1	48,7	43,0	44,2	47,0	48,9	52,1	52,3
Pressure, expander out	**bar**	52,7	54,1	52,2	52,8	54,3	54,6	55,4	55,1
dp	**bar**	15,8	20,0	21,1	28,8	30,2	34,9	40,6	42,2
Expander efficiency	**%**	39,3	41,6	37,8	35,1	32,0	25,1	22,1	18,0

Figure 54 Chart and table from expander testing where mass flow rate of CO_2 was kept constant at approximately 3,5 kg/min and the compressor is run at 15 Hz. The chart displays the expander isentropic efficiency as a function of the pressure drop across the expander.

The chart in figure 44 shows a decline in the isentropic efficiency as the pressure drop over the expander increases. The table below shows that while running the compressor on a constant speed, the pressure at the inlet of the expander increases as the torque on the expander is increased. It can also be noted that the temperature increase at the expander inlet follows the pressure increase.

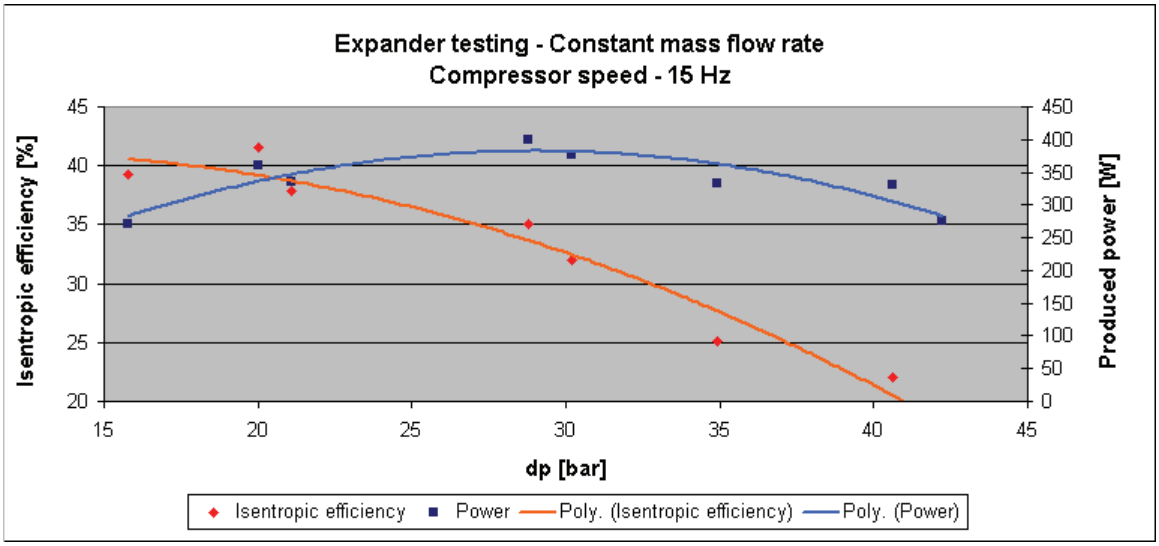

Figure 55 Comparison of isentropic efficiency and power curves for a constant mass flow rate and a compressor speed at 15 Hz.

When comparing the isentropic efficiency of the expander and the power produced by the generator driven by the expander (figure 45), the figure shows that maximum power is obtained at another pressure difference than maximum isentropic efficiency.

Another test series was conducted where the compressor speed was set to run at 22 Hz. The mass flow rate of CO_2 was still kept constant while the torque on the expander was gradually increased. The results for this series are shown in figure 46.

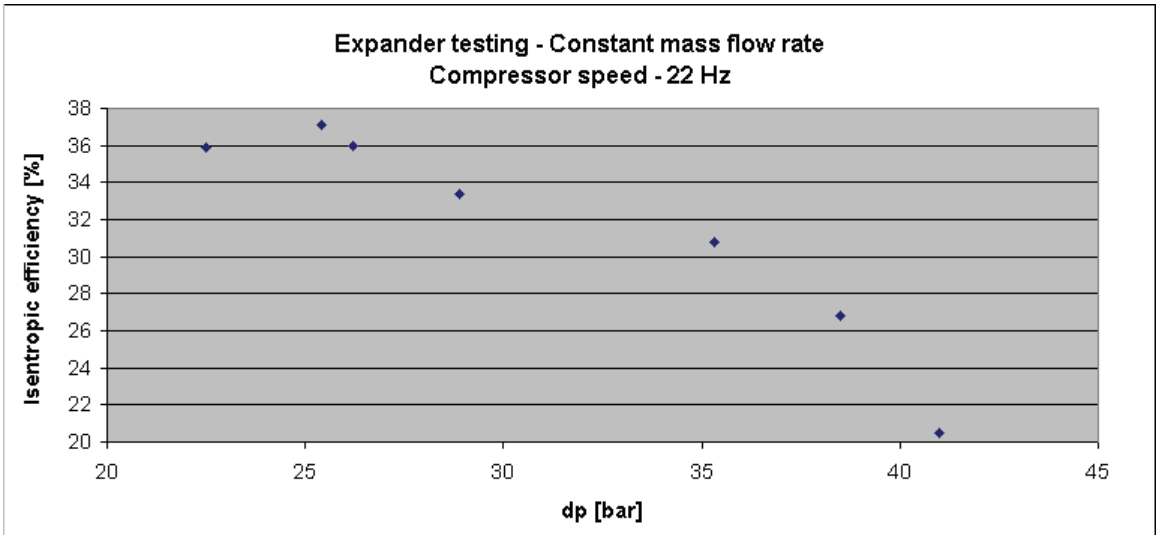

Compressor speed	**Hz**	22	22	22	22	22	22	22
Torque, expander	**Nm**	0,528	0,641	0,680	0,799	1,016	1,174	1,268
Rpm, expander	**min^{-1}**	7949	7435	6974	5951	4974	3998	2957
Power	**W**	439	499	497	498	529	492	393
Massflow $_{CO2}$	**kg/min**	3,51	3,50	3,51	3,51	3,51	3,53	3,53
Temperature, expander in	**C**	81,1	85,1	87,0	90,1	95,8	97,8	101,2
Pressure, expander in	**bar**	67,7	70,9	72,2	75,2	82,2	85,6	88,6
Temperature, expander out	**C**	55,9	57,7	59,3	60,8	62,6	63,2	66,8
Pressure, expander out	**bar**	45,2	45,5	46,0	46,3	46,9	47,1	47,6
dp	**bar**	22,5	25,4	26,2	28,9	35,3	38,5	41,0
Expander efficiency	**%**	35,9	37,1	36,0	33,4	30,8	26,8	20,5

Figure 56 Chart and table from expander testing where mass flow rate of CO_2 was kept constant at approximately 3,5 kg/min and the compressor is run at 22 Hz. The chart displays the expander isentropic efficiency as a function of the pressure drop across the expander.

From this series it is worth noting that the pressure level in general is higher while the expander efficiency seems to be a bit lower. In fact, the efficiencies shown in figure 46 never reaches above 40 % while for the series in figure 44 the highest efficiency obtained is 41,6 %.

In the comparison between the isentropic efficiency and power produced in figure 47, the same can be seen as for the case with compressor speed at 15 Hz. The maximum produced power is found at a higher pressure difference than that for the maximum isentropic efficiency.

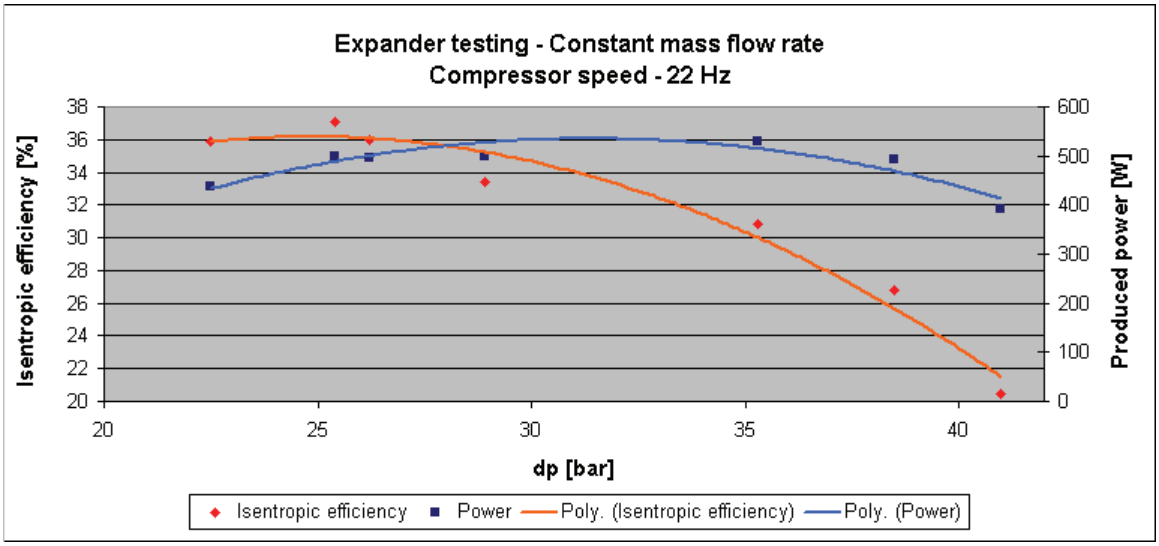

Figure 57 Comparison of isentropic efficiency and power curves for a constant mass flow rate and a compressor speed at 22 Hz.

To give an impression of how the isentropic efficiency measurements from the tests are distributed, figure 52 displays the isentropic efficiency versus the pressure difference across the expander from all five test series.

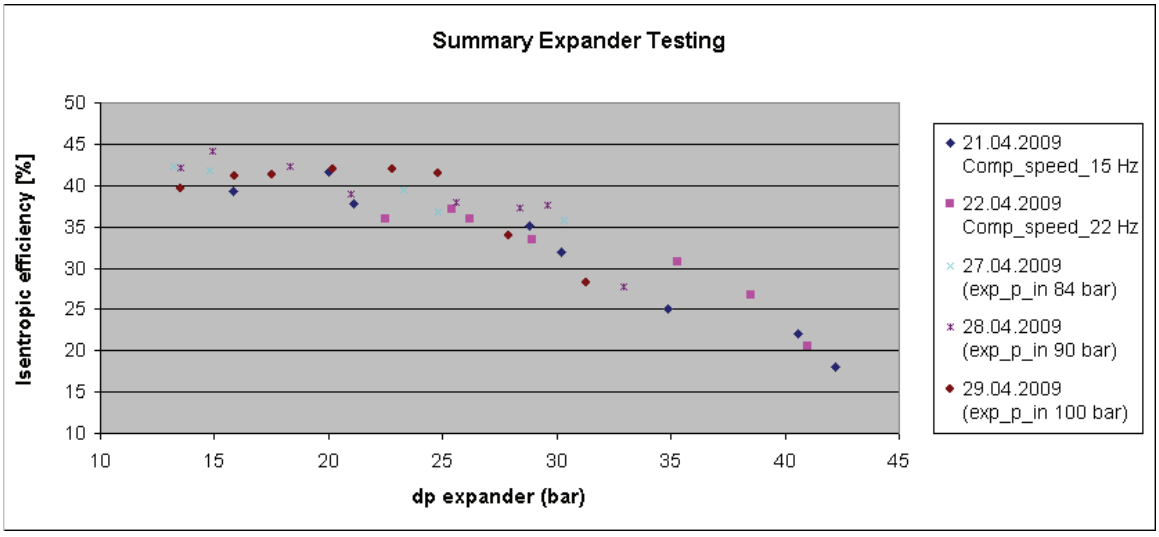

Figure 58 This chart shows the dispersion of the isentropic efficiency of all five test series performed on the expander.

Appendix B: Results from uncertainty analysis

Charts of heat exchanger duties in the test facility simulation for a warm air temperatures of 80 °C, 120 °C and 160 °C . Also shown are the uncertainty bars (max and min values) for hot and cold side of each heat exchanger.

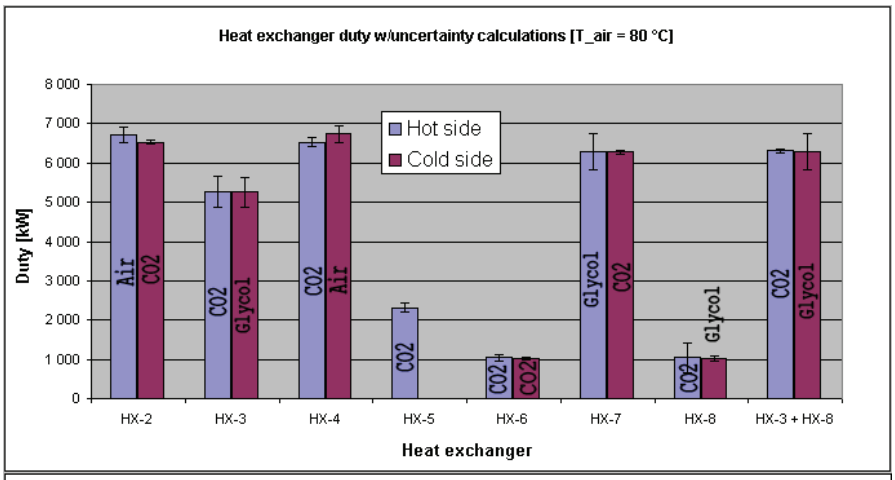

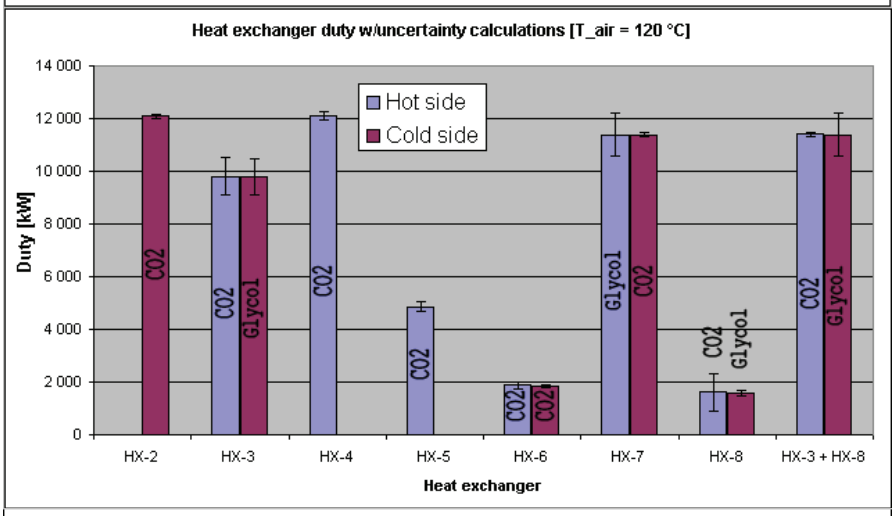

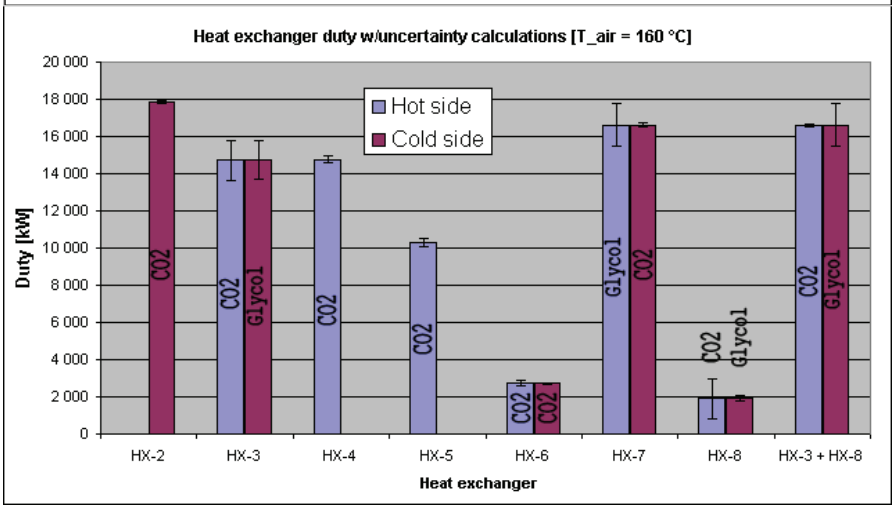

Due to unresolved issues of calculation of air properties for temperatures above 100 °C, heat exchanger duties for air is not represented in the charts for warm air temperatures of 120 °C and 160 °C. This has also had an effect on the calculation of thermal efficiency for those warm air temperatures.

The calculated values and uncertainties of net work and COP is presented in the table below:

	T = 80 °C			T = 120 °C			T = 160 °C		
	W_net [W]	η_th	COP	W_net [W]	η_th	COP	W_net [W]	η_th	COP
Calculated value	224,75	0,034	3,469	686,74	N.A.	3,064	1229,83	N.A.	2,991
Uncertainty	73,76	0,080	0,044	100,84	N.A.	0,032	114,61	N.A.	0,030
Relative uncertainty [%]	32,82	231,89	1,25	14,68	N.A.	1,03	9,32	N.A.	0,99